

***Development And Application Of An Optical
Gas-Sensor Based On Cavity Enhanced
Absorption Spectroscopy Using Diode And
Quantum Cascade Lasers***

A thesis submitted for the degree of

Doctor of Philosophy (Science)

in

Physics (Experimental)

by

Abhijit Maity

**Department of Physics
University of Calcutta**

July, 2017

Dedicated to My Parents and my Supervisor...

Acknowledgements

The research presented in this thesis would not have been possible without the support and guidance of numerous people, whom I thank sincerely. Foremost, I owe a large debt of gratitude to my supervisor, Dr. Manik Pradhan, for his sound advice, ideas and direction throughout my PhD. It is also hard to quantify the intellectual and physical resources that Dr. Pradhan made available to me in this journey. I must address my special thanks to Mithun Pal for his hard work and ideas to complete my thesis and Sanchi Maithani for her unconditional support and scrupulous proof-reading of the thesis. I am also thankful to Chiranjit Ghosh who stood by me in my hard time during my father's illness. I would like to thank my all other lab mates: Gourab Dutta Banik, Suman Som, Santanu Mandal, Akash Das, Sasthi Charan Mandal and Ikbal Ahmed for providing me a wonderful and friendly environment in the lab. Thanks to Dr. Animesh Patra who mentored me in the early days and Nirnay Samanta with whom I spent lots of enjoyable moments.

Last but not the least, I also wish to express my deepest regards to my family, specially my father, for his love and support throughout my life.

Finally, I would like to acknowledge DST, INSPIRE Fellowship for providing me doctoral fellowship and S. N. Bose National Centre for Basic Sciences for giving me an opportunity to work.

Abhijit Maity

Table of Contents

Abstract	vii
List of publications related to thesis work	ix
List of publications apart from thesis work	x
List of Patents	xi
Chapter 1: An introduction to infrared molecular spectroscopy and different techniques for trace gas sensing	1
1.1 Introduction	1
1.2 Infrared Absorption Spectroscopy	3
1.2.1 Vibrational Spectroscopy.....	3
1.2.2 Rotational Spectroscopy	5
1.2.3 Ro-vibrational Spectroscopy	6
1.3 Spectral Line Intensity.....	6
1.4 Spectral Line Width.....	7
1.5 Importance of Atmospheric Trace Gas Analysis	9
1.5.1 Significance of Methane and Acetylene Monitoring.....	10
1.5.2 Infrared Spectrum of Methane and Acetylene.....	11
1.6 Role of Trace Gases in Breath Analysis	15
1.7 Spectroscopic Techniques for Detection of Trace Gases.....	16
1.7.1 Differential Optical Absorption Spectroscopy	17
1.7.2 Tunable Diode Laser Absorption Spectroscopy	18
1.7.3 Photoacoustic Spectroscopy	18
1.7.4 Laser Induced Fluorescence	19
1.7.5 Cavity Enhanced Absorption Spectroscopy	20
1.7.6 Gas Chromatographic Separation and Detection	21

1.7.7 Proton Transfer Reaction Mass Spectrometry	23
1.8 References	24
Chapter 2: Development of Cavity Ring-Down Spectroscopy coupled with a continuous wave external-cavity quantum cascade laser for trace detection of methane isotopes	30
2.1 Introduction	30
2.2.1 Principle of CRDS operation	32
2.2.2 Sensitivity of CRDS	35
2.2.3 Mode Structure of an Optical Cavity	36
2.2.4 Stable Cavity Construction.....	39
2.2.5 Continuous wave Cavity Ring-Down Spectroscopy.....	43
2.3 Overview of Diode and Quantum Cascade Lasers	44
2.4 Experimental Setup	47
2.5 Results and Discussions.....	48
2.6 Conclusions.....	55
2.7 References	56
Chapter 3: Calibration-free ($2f/1f$) Wavelength Modulation Spectroscopy using an external-cavity quantum cascade laser for trace detection of acetylene	60
3.1 Introduction	60
3.2 Calibration-free WMS- $2f/1f$ Model.....	62
3.3 Experimental Setup	64
3.4 Results and Discussions.....	65
3.4.1 Absorption Spectroscopy of C_2H_2	65
3.4.2 Laser Characterization	67
3.4.3 Optimization of Modulation depth.....	68
3.4.4 Calibration-free normalized WMS- $2f/1f$ signal	70
3.4.5 Measurement Linearity and System Stability	71
3.5 Conclusions.....	72

3.6 References	73
Chapter 4: Design of Residual Gas Analyzer based Mass-Spectrometry for the Measurements of $^{13}\text{CO}_2/^{12}\text{CO}_2$ Isotope ratios in Human Exhaled Breath.....	76
4.1 Introduction	76
4.2 Overview of <i>H. pylori</i> infection and ^{13}C -UBT	78
4.3 Notation and Measurement Unit of Isotopic Analysis	79
4.4 Materials and Methods	80
4.4.1 Subjects	80
4.4.2 Breath sample collection.....	80
4.4.3 Statistical Analysis.....	81
4.5 Design and Function of Residual Gas Analyzer-Mass Spectrometry (RGA-MS).....	81
4.6 Diode Laser based Cavity Enhanced Absorption Technique	84
4.7 Calibration and Validation of the RGA-MS system	86
4.8 Results and Discussions.....	89
4.9 Conclusions.....	95
4.10 References	96
Chapter 5: Measurement of ^{18}O isotope of CO_2 in exhaled breath using Diode laser based Cavity Enhanced Absorption Technique for non-invasive detection of <i>Helicobacter Pylori</i> infection.....	100
5.1 Introduction	100
5.2 Materials and Methods	101
5.2.1 Human Subjects	101
5.2.2 Exhaled breath sample collection.....	102
5.2.3 Off-axis integrated cavity output spectroscopy (OA-ICOS)	102
5.2.4 Statistical Analysis.....	102
5.3 Results and Discussions.....	103
5.4 Conclusions.....	108

5.5 References	109
Chapter 6: Sensing Molecular Hydrogen in breath using a Residual Gas Analyzer for non-invasive diagnosis of Peptic Ulcer and Non-ulcerous Dyspepsia.....	111
6.1 Introduction	111
6.2 Materials and Methods	113
6.2.1 Subjects	113
6.2.2 Breath sample collection.....	114
6.2.3 H ₂ concentration and ¹³ C/ ¹² C isotope ratio measurements	115
6.2.4 Statistical analysis	116
6.3. Results.....	117
6.4 Discussion	121
6.5 Conclusions.....	125
6.6 References	126
Chapter 7: Measurements of natural isotopic abundances of ¹⁸O and ¹³C-urea in gastric juice using Cavity Enhanced Spectroscopy Technique for non-invasive monitoring of ulcer.....	129
7.1 Introduction	129
7.2 Materials and Methods	131
7.2.1 Subjects	131
7.2.2 Collection of gastric juice.....	132
7.2.3 Preparations of Chemical solutions	132
7.2.4 Fourier Transform Infrared (FTIR) Study	133
7.2.5 Isotopic determination of gastric juice urea	133
7.2.6 Off-axis Integrated Cavity Output Spectroscopy (OA-ICOS)	134
7.2.7 Breath sample collection.....	134
7.2.8 Statistical analysis	134
7.3 Results and Discussions.....	135
7.4 Conclusion	143

7.5 References	144
Chapter 8: Summary and Future Perspectives	146
8.1 Summary of the Thesis.....	146
8.2 Future Perspectives.....	147
8.2.1 Measurement of $^{13}\text{C}/^{12}\text{C}$ isotope ratio by the developed QCL based spectrometer	147
8.2.2 Combination of WMS and ICOS	148
8.2.3 Miniaturization of RGA-MS system	148

Abstract

In the environmental sciences, the study of various trace gases and volatile organic compounds (VOCs) has become the subject of immense research interest to understand the different atmospheric chemical processes and to evaluate the global climate change. Therefore, the real-time measurements of green-house gases (e.g. CO₂, CH₄, C₂H₂ etc.) with high sensitivity and accuracy are very much essential to enable the development of better benchmarking climate models. But such studies have been limited due to sub parts per million (ppm) or parts per billion (ppb) levels of concentrations of these molecules in the atmosphere. Similarly, in the field of biomedical research and non-invasive diagnostics, the investigation of biogenic trace gases as volatile disease markers has gained increasing interest. The quantitative analysis of exhaled breath, which contains several hundred endogenous volatiles, can provide important information about the health status of living subject. Most of these volatile molecules are present in volume fractions of the order of ppb or lower. Therefore, high-resolution and high-sensitive tools are much essential for detailed investigation of both atmospheric and biomedical research.

In this thesis, we mainly focused on the development and implementation of new generation optical as well as mass-spectrometric gas-sensors for the applications of environmental trace gas sensing and non-invasive diagnosis of human diseases by means of exhaled breath analysis. First, we developed a high-resolution continuous wave (*cw*) cavity enhanced absorption spectroscopy (*cw*-CEAS) technique employing an external cavity quantum cascade laser (EC-QCL) in the mid-infrared (mid-IR) molecular fingerprint region covering 7.5 to 8 μm . In the *cw*-CEAS, a high-finesse optical cavity comprised of two high reflectivity mirrors ($R \sim 99.98\%$) was exploited as an absorption measurement cell to achieve an effective optical pathlength of several

kilometres and thereby enhancing the sensitivity in the orders of 10^{-8} cm⁻¹. We subsequently explored the potential of the mid-IR *cw*-CEAS technique for trace detection of methane (CH₄) isotopes in atmosphere and human exhaled breath. Next, we developed a novel wavelength modulation spectroscopy (WMS) technique modulating the injection current of EC-QCL and subsequently demodulating at harmonics of the modulating frequency to avoid the excess $1/f$ noise of the laser. We thereafter employed the $1f$ -normalized $2f$ WMS method for ultra-sensitive detection of acetylene (C₂H₂) in ambient air.

In non-invasive medical diagnostics, we mainly targeted the detection of an ulcer-causing *Helicobacter pylori* pathogen and simultaneously explored different potential markers associated with the pathogenesis of the bacteria utilizing the optical cavity-enhanced laser spectroscopy technique combined with mass-spectrometry (MS). We designed a simple residual gas analyser based mass-spectrometry (RGA-MS) method for non-invasive diagnosis of *Helicobacter pylori* infection exploiting human breath analysis. The RGA-MS method was shown to have potential of a point-of-care (POC) diagnostic tool for large-scale screening purposes of the infection in real-time with the measurements of high-precision ¹³CO₂/¹²CO₂ isotopic enrichments in exhaled breath samples. We further showed that breath molecular hydrogen (H₂) level can be utilized to track the different disease states of *Helicobacter pylori* infection *i.e.* peptic ulcer disease (PUD) and non-ulcer dyspepsia (NUD). Finally, we utilized the diode laser based cavity-enhanced laser spectroscopy technique to assess the isotopic compositions of urea present in the human gastric juice and subsequently utilized those isotopic compositions for non-invasive detection of *Helicobacter pylori* infection. In conclusion, we developed different novel laser-based optical spectroscopic and mass-spectrometric techniques and explored their potential for atmospheric trace gas sensing and human breath analysis.

List of publications related to Thesis work

- [1] “Cavity enhanced absorption spectroscopy exploiting external-cavity continuous wave quantum cascade laser operating at 7.8 μm for monitoring methane isotopes” **Abhijit Maity**, Mithun Pal, Gourab Dutta Banik, Sanchi Maithani and Manik Pradhan. (*Under revision, 2017*).
- [2] “Calibration-free (2f/1f) Wavelength-Modulation Spectroscopy for C_2H_2 detection using an external-cavity continuous wave quantum cascade laser” **Abhijit Maity**, Mithun Pal, Sanchi Maithani, Gourab Dutta Banik and Manik Pradhan. (*Under revision, 2017*).
- [3] “Residual gas analyzer-mass spectrometry for human breath analysis: a new tool for non-invasive diagnosis of *Helicobacter pylori* infection” **Abhijit Maity**, Gourab Dutta Banik, Chiranjit Ghosh, Suman Som, Sujit Chaudhuri, Sunil B Daschakraborty, Shibendu Ghosh, Barnali Ghosh, Arup K Raychaudhuri, Manik Pradhan. *Journal of Breath Research*, 8(1),016005, **2014**.
- [4] “Oxygen-18 stable isotope of exhaled breath CO_2 as a non-invasive marker of *Helicobacter pylori* infection” **Abhijit Maity**, Suman Som, Chiranjit Ghosh, Gourab Dutta Banik, Sunil B Daschakraborty, Shibendu Ghosh, Sujit Chaudhuri, Manik Pradhan. *Journal of Analytical Atomic Spectrometry*, 29 (12), 2251-2255, **2014**.
- [5] “Molecular hydrogen in human breath: a new strategy for selectively diagnosing peptic ulcer disease, non-ulcerous dyspepsia and *Helicobacter pylori* infection” **Abhijit Maity**, Mithun Pal, Sanchi Maithani, Barnali Ghosh, Sujit Chaudhuri and Manik Pradhan. *Journal of Breath Research*, 10, 036007, **2016**.
- [6] “Natural ^{18}O and ^{13}C -urea in gastric juice: a new route for non-invasive detection of ulcer” **Abhijit Maity**, Mithun Pal, Suman Som, Sanchi Maithani, Sujit Chaudhuri, Manik Pradhan. *Analytical and bioanalytical chemistry*, 409, 193–200, **2017**.

List of publications apart from Thesis work

- [1] “An EC-QCL based N_2O sensor at $5.2 \mu m$ using cavity ring-down spectroscopy for environmental applications” Gourab Dutta Banik, Suman Som, **Abhijit Maity**, Mithun Pal, Sanchi Maithani, Santanu Mandal and Manik Pradhan. *Analytical Methods*, 9, 2315, 2017.
- [2] “Continuous wave external-cavity quantum cascade laser-based high-resolution cavity ring-down spectrometer for ultrasensitive trace gas detection” Anulekha De, Gourab Dutta Banik, **Abhijit Maity**, Mithun Pal, and Manik Pradhan. *Optics Letters*, 41, 1949-1952, 2016.
- [3] “Assessing Atmospheric CO_2 Entrapped in Clay Nanotubes using Residual Gas Analyzer” Sankar Das, **Abhijit Maity**, Manik Pradhan, Subhra Jana. *Analytical Chemistry*, 88 (4), 2205, 2016.
- [4] “Halloysite Nanotubes Capturing Isotope Selective Atmospheric CO_2 ” Subhra Jana, Sankar Das, Chiranjit Ghosh, **Abhijit Maity** and Manik Pradhan. *Scientific Reports*, 5, 2015.
- [5] “Mechanisms linking metabolism of *Helicobacter pylori* to ^{18}O and ^{13}C -isotopes of human breath CO_2 ” Suman Som, Anulekha De, Gourab Dutta Banik, **Abhijit Maity**, Chiranjit Ghosh, Mithun Pal, Sunil B Daschakraborty, Sujit Chaudhuri, Subhra Jana, Manik Pradhan. *Scientific Reports*, 5, 2015.
- [6] “Excretion kinetics of ^{13}C -urea breath test: influences of endogenous CO_2 production and dose recovery on the diagnostic accuracy of *Helicobacter pylori* infection” Suman Som, **Abhijit Maity**, Gourab Dutta Banik, Chiranjit Ghosh, Sujit Chaudhuri, Sunil Baran Daschakraborty, Shibendu Ghosh, Manik Pradhan. *Analytical and bioanalytical chemistry*, 406(22), 5405-5412, 2014.

List of Patents filed and Published

1. Patent Filed: 201631002214; Title: "A system and kit for non-invasive detection of peptic ulcer disease, non-ulcerous dyspepsia and helicobacter pylori infection", *Indian Pat. Appl.* (2016).

2. Patent Filed: 201731017087; Title: "Advancement in Methodology and System to Control Isotopic Fractionations in Carbon Containing Gases", *Indian Pat. Appl.* (2017).

Chapter 1

An introduction to infrared molecular spectroscopy and different techniques for trace gas sensing

1.1 Introduction

Molecular spectroscopy is concerned with the interaction (i.e. absorption, emission, scattering) of electromagnetic radiation with molecules. A molecule in space, just like an atom, possesses quantized energy levels. In a molecule, the energy levels mainly arise from i) the rotational motion of the molecule about the centre of gravity (rotational energy), ii) the periodic vibration of molecular bonds from the equilibrium position (vibrational energy) and iii) the electronic motion associated with the molecular bonds (electronic energy). On the other side, the electromagnetic radiation covers a wide range of frequencies extending from radio wave to gamma (γ) wave. Therefore, when a molecule interacts with an electromagnetic radiation, the frequency of the radiation largely determines the type of transitions that a molecule may undergo, such as rotational, vibrational or electronic excitation. Table 1.1 depicts different types of transitions at the different wavelength range of the electromagnetic spectrum.

Table 1.1 Electromagnetic radiation and molecular transitions [1].

Transition:	Rotational	Vibrational	Electronic
Spectral Region	Microwave	Infrared	Visible and UV
Limits: ν/cm^{-1}	$\sim 0.3\text{-}300$	$\sim 300\text{-}13000$	$\sim 13000\text{-}50000$
Limits: $\lambda/\mu\text{m}$	$\sim 30000\text{-}30$	$\sim 30\text{-}0.8$	$\sim 0.8\text{-}0.2$

When a molecule interacts with an electromagnetic radiation, the molecular transition takes place between two energy levels (E_1 and E_2) and this phenomenon is governed by the Bohr's condition where the energy difference ($\Delta E = E_2 - E_1$) between the two levels must be related to the frequency (ν) of the electromagnetic radiation by $\Delta E = h\nu$. There are three distinct types of interactions of a molecule with electromagnetic radiation, identified by Albert Einstein and Max Planck, which may occur in the molecular transition. The three distinct interactions are namely i) stimulated absorption where a molecule is excited to the higher energy state following the absorption of a photon energy, ii) stimulated emission where a photon of a particular frequency stimulates the release of an additional photon at the same frequency subsequent to the transition of a molecule from an excited state to a lower energy state, and iii) spontaneous emission where a molecule in an excited state emits a photon and returns to a lower energy state.

This thesis is focused on the development and implementations of spectroscopic as well as mass-spectrometric techniques for trace gas sensing in atmosphere and human exhaled breath. The spectroscopic techniques, presented in this thesis, comprise of both near-infrared diode laser and mid-infrared quantum cascade laser. Therefore, the aim of the first chapter is to introduce infrared spectroscopy and discuss different spectroscopic and mass-spectrometric methods to monitor

trace gases and subsequently to learn the significance of the different trace gases present in the atmosphere and human exhaled breath.

1.2 Infrared Absorption Spectroscopy

The infrared (IR) region of electromagnetic spectrum deals with the vibrational molecular transitions, each of which is referred to as a band. Each vibrational band consists of a large number of closely spaced ($\leq 10 \text{ cm}^{-1}$) rotational transition lines associated with each vibrational excitation. Vibrational, rotational and combined ro-vibrational spectroscopy are discussed in the subsequent sub-sections.

1.2.1 Vibrational Spectroscopy

The basic principle of vibrational spectroscopy is that vibrational motion of molecular bonds from the equilibrium position must give rise to a change of electric dipole moment of a molecule. A polyatomic molecule containing N number of atoms has $3N-6$ number of normal modes of vibration, whereas it is $3N-5$ for a linear molecule. However, all the normal modes of vibration may not be IR active; the normal modes which eventually change the net electric dipole moment of the molecule are the IR active.

For a small periodic displacement (x) of a molecular bond length (r) from the equilibrium position (r_e), the potential energy (V) associated with the displacement can be modelled as a parabolic function of displacement x and expressed as

$$V = kx^2; \text{ where } x = (r - r_e) \quad (1.1)$$

where k is the force constant. The energy associated with the vibration is quantized and the permitted vibrational energy levels, E_v , are given by

$$E_v = (v + \frac{1}{2})\hbar\omega; \text{ where } \omega = \sqrt{\frac{k}{\mu}} \quad (1.2)$$

where v is the vibrational quantum number and can take only integer values. The quantity μ is the reduced mass and is given by

$$\mu = \frac{m_1 m_2}{m_1 + m_2} \quad (1.3)$$

where m_1 and m_2 are the masses of atoms.

The vibrational levels can be expressed in terms of wavenumber as

$$G(v) = (v + \frac{1}{2}) \bar{\nu} ; \bar{\nu} = \frac{1}{2\pi c} \sqrt{\frac{k}{\mu}} \quad (1.4)$$

The selection rule for the permitted vibrational transitions is $\Delta v = \pm 1$. However, this selection rule is derived from the harmonic oscillator wave function and the rule is approximately valid under anharmonic condition. If the selection rule was strictly followed, the vibrational spectrum of a diatomic molecule would consist of a single fundamental band ($1 \leftarrow 0$).

The motion of vibrating bonds is not purely harmonic and hence the restoring force is no longer proportional to the displacement of bond. The anharmonic effects can be better modelled under the Morse potential function which represents the potential energy surface along the co-ordinate of the molecular bonds. The vibrational states derived from the Morse potential, in terms of wavenumber, are given by

$$G(v) = (v + \frac{1}{2}) \bar{\nu} - (v + \frac{1}{2})^2 x_e \bar{\nu} ; x_e = \frac{\bar{\nu}}{4D_e} \quad (1.5)$$

where D_e is the depth of the potential minimum and x_e is the anharmonicity constant. The selection rule for an anharmonic oscillator is given by $\Delta v = \pm 1, \pm 2, \pm 3, \dots$

This anharmonicity leads to the convergence of vibrational energy levels and gives rise to the weaker overtone transitions ($2 \leftarrow 0$, $3 \leftarrow 0$ etc.) which are forbidden by the selection rule of $\Delta v = \pm 1$. Moreover, it is considered up to now that the vibrational levels are independent and do not affect each other. Therefore, if this restriction to the simple harmonic oscillator is relaxed, the selection rule then also allows the combination bands.

1.2.2 Rotational Spectroscopy

The key criterion of pure rotational spectroscopy is that molecules must have permanent electric dipole moments, and hence the direction of electric dipole moment changes periodically when the molecule rotates around the centre of gravity of the molecule. The rotational spectroscopy provides the information about the bond length and bond angle in a molecule. Although pure rotational spectroscopy is the microwave region phenomenon, but each vibrational level contains its own series of more closely spaced rotational lines. If we assume that the molecules are rigid and are not distorted during rotation, the rotational energy levels are then given by

$$F_J = BJ(J + 1); \text{ where } B = \frac{\hbar^2}{4\pi cI} \quad (1.6)$$

where B is the rotational constant, J (=0,1,2...) is the angular momentum quantum number and I is the moment of inertia about the axis of rotation. The selection rule for a rotational transition is given by $\Delta J = \pm 1$ and the energy separation between the adjacent rotational levels is thus 2BJ.

However, in real situation the centrifugal distortion takes place during the rotation of a molecule and stretches the bonds of the molecule, thereby increasing the moment of inertia. As a result, the spacing between two adjacent rotational energy levels is reduced compared to

the spacing predicted from rigid rotator analysis. The rotational energy levels with centrifugal distortion can be expressed as

$$F_J = BJ(J + 1) - D_J J^2 (J + 1)^2; \text{ where } D_J = \frac{4B^3}{\nu^2} \quad (1.7)$$

where D_J is the centrifugal distortion constant.

1.2.3 Ro-vibrational Spectroscopy

Ro-vibrational spectroscopy represents the fine structure of vibrational band which arises from rotational transitions accompanying a vibrational excitation. The selection rule for rotational transition i.e. $\Delta J = \pm 1$ is still valid for ro-vibrational spectroscopy. Moreover, the rotational transition corresponding to $\Delta J = 0$ is also allowed provided that the molecule must have the angular momentum about its own axis. A vibrational band consists of three rotational branches namely (i) P branch ($\Delta J = -1$), (ii) Q branch ($\Delta J = 0$) and (iii) R branch ($\Delta J = +1$).

The energy states of ro-vibrational levels, neglecting anharmonicity and centrifugal distortion, can be expressed as

$$S(\nu, J) = (\nu + \frac{1}{2})\bar{\nu} + BJ(J + 1) \quad (1.8)$$

1.3 Spectral Line Intensity

The basic principle of absorption spectroscopy is the Beer-Lambert law, which is given by

$$I = I_0 \exp(-\sigma_\lambda [X]d) \quad (1.9)$$

where I_0 and I are incident and transmitted light intensities, σ_λ is the line integrated absorption cross-section, $[X]$ is the sample concentration and d is the sample length. Therefore, strength of any absorption, for a

particular absorption cross-section, primarily depends on two factors (i) concentration of the sample and (ii) sample length. The strength of absorption is proportional to both sample concentration and sample length.

The spectral line intensity also depends on two factors: (i) the number of molecules initially present in the state from which transition occurs and (ii) the transition probability. The relative population of any two states is governed by the Boltzmann distribution expressed as

$$\frac{N_{upper}}{N_{lower}} = \frac{g_u}{g_l} \exp\left(\frac{-\Delta E}{kT}\right) \quad (1.10)$$

where N is the total number of molecules in a particular state, $\Delta E = E_{upper} - E_{lower}$ is the energy difference between two states, T is the temperature, k is the Boltzmann constant, and g_u and g_l are the degeneracies of the upper and lower state, respectively.

1.4 Spectral Line Width

Spectral lines are always associated with a finite width. The spectral width provides information about the energy levels and the environment of the targeted molecule. There are several factors which may contribute to the broadening of the spectral line, and the conditions under which the experiment is performed, determine to what extent some of these factors contribute to the spectral broadening.

One of the main sources of broadening is Doppler broadening which arises from the Doppler shift in which radiation is shifted in frequency when the source is moving towards or away from the observer. The observed spectral profile reflects the Maxwell-Boltzmann distribution of molecular velocity parallel to the line of sight. This Doppler shift results in a Gaussian line shape function with full-width half maximum (FWHM):

$$\delta\nu = \frac{2\nu}{c} \sqrt{\frac{2kT}{m} \ln 2} \quad (1.11)$$

where m is the mass of the molecule, T is the temperature, ν is the transition frequency, k is the Boltzmann constant and c is the speed of light. Doppler broadening increases with sample temperature because the molecules have a wider range of speeds at higher temperatures. Narrow spectral lines may thus be obtained at low temperature.

Lifetime broadening is another mechanism which contributes to the finite width of spectral lines. Lifetime broadening arises from the quantum mechanical effect. The Heisenberg uncertainty principle states that if the lifetime of a system in a particular state is τ , then the energy levels of the state will be uncertain to an extent of δE where

$$\delta E \approx \frac{\hbar}{\tau} \quad (1.12)$$

As no excited state has an infinite lifetime, all spectral transition lines exhibit a certain width and even at low temperature, this residual broadening still remains.

Two other factors that contribute to the finite lifetime of a state are (i) pressure deactivation and (ii) spontaneous emission. At high pressure (greater than 50-100 Torr) collisional deactivation can occur, which leads to pressure broadening. Pressure broadening gives rise to line shapes with Lorentzian profiles. Collision also causes transient interactions between the colliding molecules and perturbs their energy levels, resulting in further broadening and frequency shifts of spectral lines.

In the spontaneous emission, the rate of spontaneous emission depends on the frequency of the transition. Therefore, the 'natural width' of the spectral line also depends on the region of the electromagnetic spectrum

which is used for the measurement. The ‘natural’ lifetime broadening also results in Lorentzian line shape profiles.

However, it is important to remember that when both Doppler and Lorentzian broadening contribute to the broadening of an individual line profile, Voigt profile, which is the convolution of Gaussian line shape with a Lorentzian line shape, should be used to fit the spectral line.

1.5 Importance of Atmospheric Trace Gas Analysis

For atmospheric research, real-time monitoring of the concentrations of trace atmospheric constituents is essential in understanding the underlying processes that occur in the atmosphere. There are a number of sources of trace gases, including biogenic and anthropogenic release,

Table 1.2: Mixing ratios and chemical lifetimes of various trace gases [2-9].

Trace gases	Mixing ratio		Lifetimes
	ppmv (10^{-6})	ppbv (10^{-9})	
Methane (CH ₄)	1.7		3.0 years
Acetylene (C ₂ H ₂)		0.8-150	7-200 days
Ethane (C ₂ H ₄)		1-30	20 hours to 5.2 months
Carbon monoxide (CO)		50-200	-
Nitrogen dioxide (NO ₂)		0.01-200	-
Tropospheric ozone (O ₃)		10-500	-

as well as production through chemical reactions. Table 1.2 shows typical mixing ratios of selected trace gases present in the troposphere expressed either in parts per million by volume (ppmv/ 10^{-6}) or parts per billion by volume (ppbv/ 10^{-9}).

Despite their low concentrations, these trace molecules have a large impact on tropospheric chemistry. Table 1.2 also illustrates the typical atmospheric lifetimes of selected trace gases with respect to the attack by OH/ NO_3 / O_3 . The comparatively long atmospheric lifetime has been allowing these compounds to reach remote areas as well as the stratosphere and hence these compounds can be targeted as tracers for polluted air masses. Therefore, to get a local as well as global understanding of the distribution and effects of the trace molecules, it is very important to make accurate and comparable measurements of individual trace molecules. Moreover, the measurement of the abundance of the stable isotopologues of individual trace molecules is a possible key for understanding the possible sources and sinks of the trace molecules in the atmosphere. The isotopologue ratios can be used to estimate the relative source strengths of the diverse anthropogenic and natural emissions of trace molecules and their variation with time.

In this thesis, trace sensing of acetylene (C_2H_2) and methane (CH_4) isotopes in ambient air are presented exploiting the different spectroscopic techniques.

1.5.1 Significance of Methane and Acetylene Monitoring

Methane (CH_4) is the most predominant greenhouse gas after carbon dioxide (CO_2) and water (H_2O) present in the Earth's atmosphere [10-15]. However, the global warming potential (GWP) of CH_4 is almost 25 times greater than CO_2 over 100 year time horizon. The main sources of CH_4 are various anthropogenic activities. It is a major component of natural gas, which is used to generate electricity in various countries [16]. The present atmospheric concentration of CH_4 has been increased by 166% since the pre-industrial times [17]. Methane is also important in

astrophysical exploration because it is found in the atmosphere of various planets [18].

Acetylene (C_2H_2) is one of the trace non-methane volatile organic compounds (VOCs) present in the Earth's atmosphere. It is an important tracer of anthropogenic sources with relatively long atmospheric lifetime of several days to months [19-21]. C_2H_2 is also one of the potential green-house gases and significantly contributes to the global warming. It is generally formed in the intermediate stage of combustion of hydrocarbon fuels as a precursor of soot which has serious adverse effects on human health and environment [22,23]. Moreover, C_2H_2 is widely used as a fuel and essential organic raw material in various industries, which is indeed an inflammable and explosive gas with an explosive limit of 2.3–72.3% in air at the ambient temperature and pressure [24].

Therefore, real-time and sensitive monitoring of CH_4 and C_2H_2 in the ambient air is essential for environmental studies, human health and industrial safety purposes.

1.5.2 Infrared Spectrum of Methane and Acetylene

Methane (CH_4) is a tetrahedral molecule and the simplest hydrocarbon. It has $3 \times 5 - 6 = 9$ infrared modes of vibration with four stretching and five bending modes as presented in Table 1.3 [25]. The four C-H stretching modes correspond to a symmetric stretching band (ν_1) at $\sim 2916.48 \text{ cm}^{-1}$ and a triply degenerate antisymmetric stretching band (ν_3) at $\sim 3019.49 \text{ cm}^{-1}$. The five bending modes correspond to a triply degenerate bending band (ν_4) at $\sim 1310.76 \text{ cm}^{-1}$ and a doubly degenerate bending band (ν_2) at $\sim 1533.33 \text{ cm}^{-1}$. However, only ν_3 and ν_4 vibrational modes of CH_4 are

Table 1.3 Summary of the fundamental vibrational modes of methane [25].

Assignment	Vibration mode	Degeneracy	Band origin (cm ⁻¹)	IR active
ν_1	Symmetric C-H stretch	1	~2916.48	No
ν_2	Bend	2	~1533.33	No
ν_3	Asymmetric C-H stretch	3	~3019.49	Yes
ν_4	Bend	3	~1310.76	Yes

normally IR active. Therefore, the infrared spectra of CH₄ show only two strong absorption bands consisting of many overlapping bands, which are demonstrated in the simulated HITRAN spectra (Figure 1.1) [26].

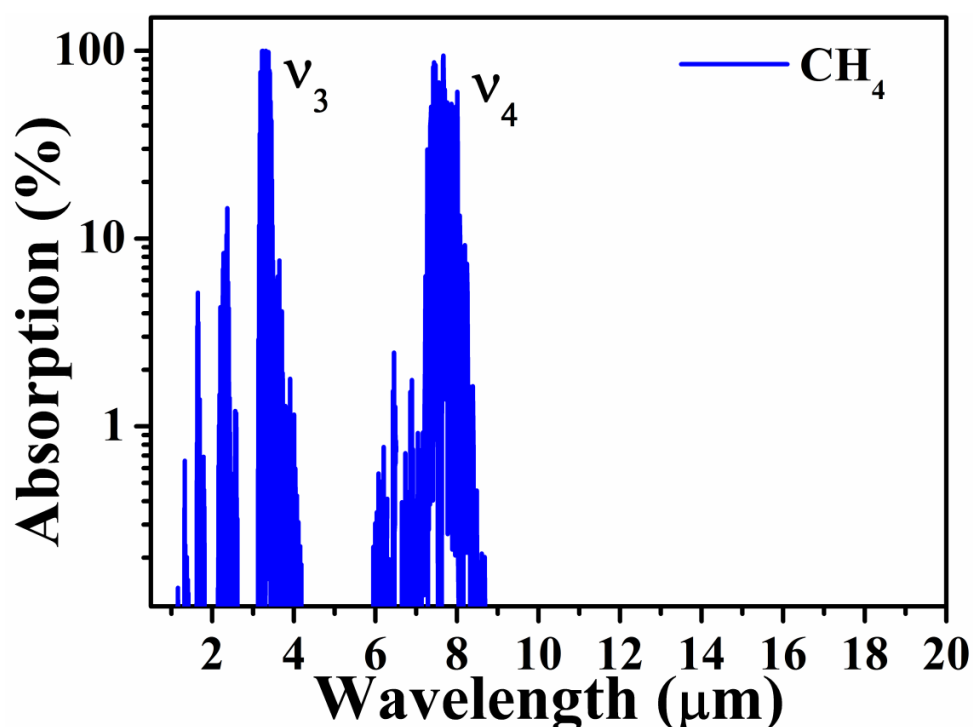


Figure 1.1 IR spectra of methane with different fundamental and combinational bands simulated from the HITRAN database at atmospheric pressure and 296K temperature.

Acetylene (C_2H_2) is a linear and centre-symmetric molecule with total 4 numbers of atoms. Therefore, the total number of fundamental normal modes (ν) of vibration of C_2H_2 becomes $3 \times 4 - 5 = 7$ as presented in Table 1.4 [27]. There are three singly degenerate stretching modes (ν_1, ν_2, ν_3) and two doubly degenerate bending modes (ν_4, ν_5). Only two fundamental vibrational modes i.e. (ν_3 and ν_5) are IR active because they produce a change in the zero electric dipole moment of C_2H_2 and hence give rise to IR absorption. Apart from the two fundamental vibrational bands ν_3 and ν_5 with band origins at $\sim 3300 \text{ cm}^{-1}$ and 730 cm^{-1} , respectively C_2H_2 has two strong combination bands ($\nu_1 + \nu_3$) and ($\nu_4 + \nu_5$) at 6500 cm^{-1} and 1300 cm^{-1} , respectively. The combination band ($\nu_1 + \nu_3$) arises due to stretching of C-H bonds whereas the origin of ($\nu_4 + \nu_5$) combination band is the bending of C-H bonds. A simulated spectrum,

Table 1.4 Summary of the fundamental vibrational modes of acetylene [27].

Assignment	Vibration mode	Degeneracy	Band origin (cm^{-1})	IR active
ν_1	Symmetric C-H stretch	1	~ 3372.5	No
ν_2	Symmetric C-C stretch	1	~ 1973.5	No
ν_3	Asymmetric C-H stretch	1	~ 3294.8	Yes
ν_4	Symmetric bend	2	~ 611.7	No
ν_5	Asymmetric bend	2	~ 729.1	Yes

from the HITRAN database, of infrared absorption bands of C_2H_2 is depicted in Figure 1.2 [26].

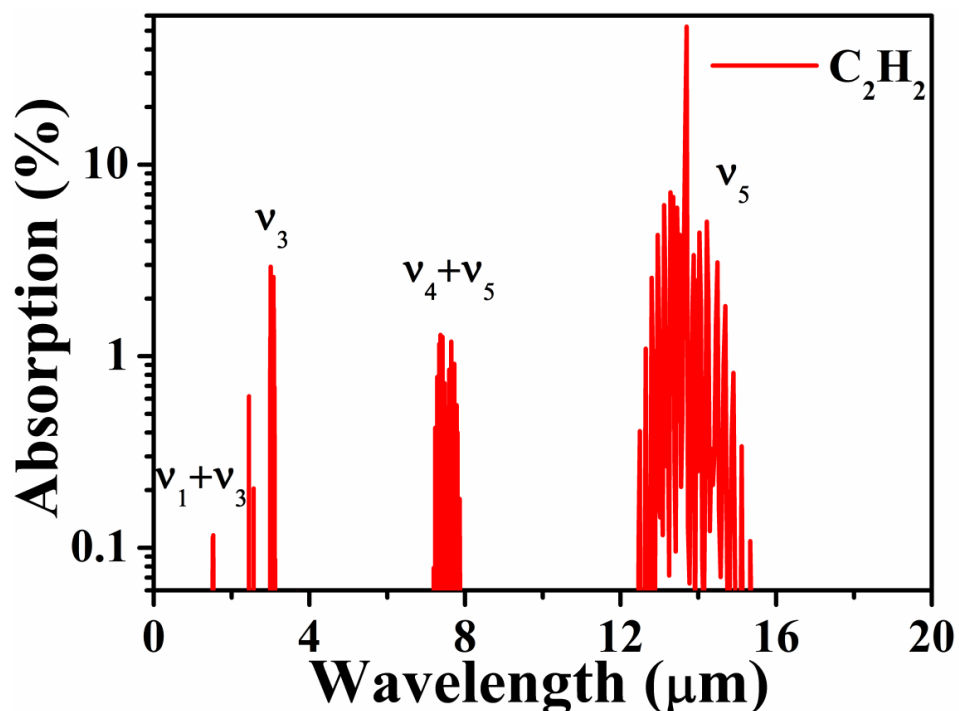


Figure 1.2 IR spectra of acetylene with different fundamental and combinational bands simulated from the HITRAN database at atmospheric pressure and 296K temperature.

In this thesis, ν_4 fundamental band of CH_4 and $(\nu_4+\nu_5)$ combination band of C_2H_2 at around 1300 cm^{-1} have been exploited for trace detection in ambient air. The spectral region of 1300 cm^{-1} is particularly significant because this region is the molecular “fingerprint” region with fundamental and combinational bands of several other important trace gases like N_2O , H_2S , H_2O_2 and SO_2 [26]. Therefore, this spectral region will provide a unique opportunity to study numerous atmospheric pollutants in a single spectral window. Moreover, the spectral region of 1300 cm^{-1} is in close vicinity of atmospheric transmission window of $770\text{ -}1280\text{ cm}^{-1}$ and hence free from any major interference of atmospheric abundant molecules like CO_2 , H_2O , O_2 and N_2 . Therefore, this spectral region has very high importance in real-field sensor designing for atmospheric trace gas sensing. Nonetheless, the mid-infrared (mid-IR) spectral region is far less studied than near-infrared (near-IR) region and hence theoretically simulated spectroscopic parameters associated with the molecular transitions in this region are required to be experimentally validated.

1.6 Role of Trace Gases in Breath Analysis

In recent years the analysis of numerous trace gases in human breath with ultra-low concentrations has emerged as a promising new-generation, non-invasive technique for the diagnosis of various human

Table 1.5: Biomarkers for different diseases and their concentrations in exhaled human breath [28].

Biomarker	Concentration in exhaled breath	Diseases
Isotopes of CO ₂	4-5%	<ul style="list-style-type: none"> • Various Metabolic diseases like diabetes. • Different gastro-intestinal disorders like <i>Helicobacter pylori</i> infection, peptic ulcer etc.
Methane (CH ₄)	2 ppm–10 ppm	Intestinal problems, colonic fermentation.
Hydrogen (H ₂)	0-10 ppm	Gastro-intestinal diseases, carbohydrate malabsorption
Ammonia (NH ₃)	0.5 ppm–2 ppm	Kidney failure, cirrhosis.
Hydrogen Sulphide (H ₂ S)	0.8–1.3 ppm	Airway inflammation.
Nitric Oxide (NO)	10 ppb–50 ppb	Asthma, acute lung injury, lung infection, lung cancer.
Acetone ((CH ₃) ₂ CO)	<1 ppm	Diabetes, lung cancer, dietary fat losses, congestive heart failure.

diseases. Exhaled human breath consists of more than 3000 gas molecules associated with physiological and metabolic processes continuously occurring inside the human body. Various trace molecules, in exhaled breath, have already attracted a great deal of medical research due to their potential link to various human diseases [28-30]. Table 1.5 depicts typical concentrations of few selected trace molecules present in the exhaled breath and their roles in various human diseases [28].

Breath tests can be also utilized for analysis of environmental exposure and phenotypic information of enzyme activity. Several breath tests have already been approved by the US Food and Drug Administration (FDA) for the clinical applications such as [31]

- (i) Breath nitric oxide test for monitoring asthma therapy
- (ii) Breath carbon monoxide test for neonatal jaundice
- (iii) Breath ethanol test for blood alcohol
- (iv) Breath carbon dioxide test for capnography
- (v) Breath hydrogen and methane tests for gastrointestinal diagnosis
- (vi) Breath test (Heartsbreath™) for detection of heart transplant rejection
- (vii) ^{13}C -urea breath test (^{13}C -UBT) for detection of gastric infection by *Helicobacter pylori*.

In this present thesis, different drawbacks of ^{13}C -urea breath test (^{13}C -UBT) are addressed and subsequently potential solutions to overcome the problems are provided utilizing different mass-spectrometric and optical spectroscopic techniques.

1.7 Spectroscopic Techniques for Detection of Trace Gases

Monitoring of trace gas species present in a variety of environments is the subject of extensive research, and this not only includes monitoring

of atmospheric constituents at sites across the globe, but also extends to human breath analysis for medical diagnostics of various human diseases. Therefore, the necessity to identify and quantify individual trace molecules and their stable isotopologues levels has led to the development of different spectroscopic and non-spectroscopic detection methods for monitoring trace molecules.

There are a variety of spectroscopic as well as mass-spectrometric methods to monitor the concentrations of the trace molecules. 'Differential optical absorption spectroscopy (DOAS)', 'Tunable diode laser absorption spectroscopy (TDLAS)', 'Photo acoustic spectroscopy (PAS)', 'Laser induced fluorescence (LIF)' and 'Cavity enhanced absorption spectroscopy (CEAS)' are widely utilized spectroscopic methods, whereas 'Gas chromatography mass-spectrometry (GC-MS)' and 'Proton transfer reaction mass spectrometry (PTRMS)' are among the commonly used mass spectrometric methods for the measurements of different trace molecules. A brief overview of these techniques is presented in this section.

1.7.1 Differential Optical Absorption Spectroscopy

Differential optical absorption spectroscopy (DOAS) was first reported by Platt *et al.* [32]. In DOAS, light source and receiver are generally placed at several kilometres apart to measure the concentrations of a particular species through absorption spectroscopy. The long pathlength provides the excellent sensitivity. However, DOAS suffers from poor spatial resolution as it measures an average sample concentration over the entire pathlength. The spatial resolution of DOAS can be improved in multi-pass optical absorption spectroscopy (MOAS), where a White cell provides a long pathlength within a small region.

In DOAS, the light intensity I_0 in absence of sample cannot be measured and hence a differential absorption cross-section is used to measure the sample concentration. The differential absorption cross-section is generally determined by comparing the light intensity received by

detector at on and off resonance with molecular absorption feature. Therefore, DOAS requires a reference spectra obtained in the laboratory, which can be fitted to the atmospheric spectra to calculate the mixing ratio of the trace species.

However, DOAS has been used to detect different atmospheric species such as iodine monoxide (IO) in the marine boundary layer (MBL) [33] and the hydroxyl radical with ppb level concentrations [34].

1.7.2 Tunable Diode Laser Absorption Spectroscopy

Tunable diode laser absorption spectroscopy (TDLAS), pioneered in 1960 [35], is a commonly employed spectroscopic technique for trace gas sensing applications owing to its high detection sensitivity and accuracy, long-term stability and fast response. TDLAS is a direct absorption technique and usually carried out in a long path absorption cell such as a Herriot cell [36], with a tunable light source.

TDLAS is often combined with modulation spectroscopy to further improve the sensitivity reducing the excessive laser $1/f$ noise [37]. The advantage of modulation spectroscopy in TDLAS is that the amplitude of difference signal is directly proportional to the species concentration and the signal is detected at harmonics of modulating frequency where the laser noise is significantly reduced [38].

Recent advancements in mid-IR laser sources, in particular quantum cascade lasers (QCLs), have enabled the development of compact sensors that make use of modulation techniques, and which demonstrate excellent sensitivity [39,40].

1.7.3 Photoacoustic Spectroscopy

Photoacoustic Spectroscopy (PAS) is different from the conventional spectroscopy as it works on the principle of photoacoustic effect [41,42]. In PAS, vibrationally excited molecules, after IR absorption, collide with bath gas molecules (e.g. N_2 and O_2) and therefore the vibrational energy

is transferred to translation energy, creating an acoustic wave in the cell. The acoustic signal is then converted to electric signal with the help of microphone and the amplitude of the signal is proportional to the concentration of the absorbing molecule inside the cell.

The magnitude of a photoacoustic (PA) signal is directly proportional to the optical power of the laser, and hence high power CO₂ lasers are often used to achieve low detection limits. Schilt *et al.* [43] designed a PA instrument with a CO₂ laser for ultra-sensitive detection of ammonia. Recently, mid-IR quantum cascade lasers have been employed in PAS and detection limit of ppb has been reported [44].

1.7.4 Laser Induced Fluorescence

Laser induced fluorescence (LIF) is a very sensitive spectroscopic method for quantitative measurement of sample concentration. In LIF, targeted molecule or radical is excited to a vibrational level of an excited electronic state after laser radiation. The spontaneous emission from the excited molecule is used to measure the sample concentration subject to the sensitive calibration of the instrument. The intensity of the spontaneous emission is proportional to the sample concentration. LIF has greater sensitivity than direct absorption spectroscopy because the background signal of LIF is very weak. The sensitivity of LIF can be further enhanced with the use of a single photon detector. However, LIF is only suitable for the molecules that have bound and optically assessable excited electronic state. Moreover, LIF suffers from collision quenching of fluorescence at atmospheric pressure.

To overcome this problem, samples are often expanded into low pressure vacuum chambers for the detection. This technique is known as fluorescence assay by gas expansion (FAGE) [45]. This method reduces the concentration of target species in the sample but the dilution is compensated for by the excellent sensitivity of the technique. Using this technique, Bloss *et al.* demonstrated a sensitivity of 3.1×10^5 molecule cm⁻³ and 2.6×10^6 molecule cm⁻³ for OH and HO₂, respectively [46].

An alternative approach to LIF is chemiluminescence. This method operates on a similar principle to fluorescence of laser radiation. In principle, chemiluminescence should have an even lower background signal than LIF because of scattered laser light. The sensitivity is, however, limited by the efficiency of the excitation reaction.

1.7.5 Cavity Enhanced Absorption Spectroscopy

Cavity enhanced spectroscopic techniques utilize an optical cavity comprised of two or more highly reflective mirrors. A laser source injected into the cavity through one of the mirrors is reflected back and forth between the mirrors several times, giving an optical pathlength of several kilometres. The first cavity enhanced technique which was used to measure an absorption spectrum of oxygen in an open air, was cavity ring down spectroscopy (CRDS), used by O'Keefe and Deacon in 1988 [47]. CRDS measures the exponential decay of light intensity leaking from one of the cavity mirrors, and the ring-down time (τ) is used to calculate the concentration of the absorbing species present in the cavity without any secondary calibration [48]. An alternative cavity enhanced technique is cavity enhanced absorption spectroscopy (CEAS) which uses a high finesse cavity into which a laser beam is injected in an off-axis alignment, and the cavity behaves like a multi-pass cell supporting a continuum of frequencies [49]. The frequency of the laser is swept over a small spectral range at fast repetition rates. Therefore, several spectra can be accumulated in a short time which eventually improves the signal to noise (S:N) ratio and hence the detection limit.

The high sensitivity of cavity enhanced techniques makes them suitable for *in situ* measurements of atmospheric constituents. Other advantages include good temporal resolution, compact instrumentation, and quantitative concentration analysis from the acquired spectra. The continuous wave (*cw*) CRDS technique was widely applied to measure ppbv (10^{-9}) level concentrations of atmospheric trace gases [50,51].

Broadband CRDS (BB-CRDS) [52], a variant of CEAS, utilizes a broadband light source to excite an optical cavity, and instead of sweeping the laser frequency across an absorption line, the entire spectrum can be recorded on a broadband detector such as charge coupled detector (CCD).

In optical-feedback CRDS (OF-CRDS) technique [53], light from a *cw* laser is coupled into a fixed length cavity by chirping the laser until the frequency coincides with a cavity mode. Once overlap between the frequency of the laser and cavity mode is achieved, feedback to the laser fixes its frequency and the intensity of light inside the cavity increases. When the laser is extinguished at the end of the current pulse, an experimental decay of light intensity from the cavity may be recorded. OF-CRDS has high temporal resolution due to the repetition rate at which the laser frequency may be chirped.

1.7.6 Gas Chromatographic Separation and Detection

The complete process of gas chromatographic (GC) separation and detection can be divided into four main sections: sample acquisition, preparation and injection, separation and detection. Analysis of atmospheric samples may be performed either *in situ* or post acquisition, and preferable sampling mode generally depends on the stability of the targeted species. However, the post-acquisition method is only suitable for species that are unreactive. For the sample acquisition, a gas sample is first passed through a trap containing a specific adsorbent material for the molecules of interest. The trapped molecules is then released by thermal desorption and subsequently measured in laboratory.

For the atmospheric species with relatively high concentrations, such as CH₄, sample can directly be injected on to a GC column. However, for the trace gas species with much lower concentrations, sample pre-concentration is required to artificially enhance the concentration prior to the GC separation.

It is essential to remove water from the sample before it is passed through the absorbent trap because condensation of water onto the absorbent significantly reduces absorbent capacity and subsequently affect the GC columns and detection system. Moreover, ice crystals, formed at sub-ambient temperature, may cause blockage. A Nafion dryer is commonly used to remove water from the sample. Other drying agents, such as potassium carbonate and magnesium perchlorate, can be used but the requirement for periodic regeneration makes them less popular.

There are different kinds of detectors that are used to measure the molecules eluting from a GC column. The three most popular detector systems are: (i) flame ionisation detectors (FIDs), (ii) mass spectrometry (MS) and (iii) electron capture devices (ECD). A detailed description of these devices may be found in the literature [54,55]. FID offers high sensitivity and linearity across a wide concentration range and is commonly used for the detection of hydrocarbons [56]. MS, one of the most versatile detection methods, may be used to detect hydrocarbons [57], oxygenated VOCs [58] and a wide range of other species. ECDs are highly sensitive to electrophilic compounds such as halocarbons [59]. However, ECDs show no response to hydrocarbons. Oxygenated ECD may be used to enhance the sensitivity for the species which have a poor ECD response [60].

All the detectors require calibration and once the calibration is complete, these instruments provide a quantitative and reliable analysis of atmospheric samples.

1.7.7 Proton Transfer Reaction Mass Spectrometry

Proton transfer mass spectrometry, a variant of chemical ionisation mass-spectrometry (CIMS), utilizes H_3O^+ ions to protonate VOCs. H_3O^+ ions, generated by ionisation of water vapour using a glow discharge, are passed through a drift tube which is flushed with a gaseous sample such as air. H_3O^+ exclusively protonates VOCs which tend to have higher proton affinity than water. In contrast, the reactions do not occur with the inert species such as N_2 , O_2 , Ar and CO_2 as their proton affinities are lower. Proton transfer is typically a non-dissociative process in which only one product ion is formed for each VOC. However, if the species do dissociate, the predictable pathways facilitate the identification of the formed products [61].

PTR-MS has the potential of rapid detection of VOCs at very low concentrations (10-100 pptv). The quantitative concentration analysis can be performed using Equation 1.13 provided the reaction time, t and rate constant of the protonation reaction, k are known [62]. For the accurate quantification of VOCs, the flow drift-tube is essential to perform protonation under well-defined conditions.

$$[R] = \frac{1}{kt} \frac{[RH^+]}{[H_3O^+]} \quad (1.13)$$

The sensitivity of PTR-MS increases with the increase of the ratio of the product ion signal to the density of the neutral compound and hence sufficient time for reaction in the drift tube is essential. However, the problem of same mass for identification of ions still exists, and the sensitivity is often affected due to the clustering of water molecules around the product ion [63]. Nevertheless, PTR-MS has widely been applied in atmospheric monitoring [64], and is a powerful tool to detect a large number of VOCs.

1.8 References

- [1] Atkins P W, *Physical Chemistry*, 5th edition, Oxford University Press, 1994.
- [2] Wayne R P, *Chemistry of Atmospheres*, 3rd edition, Oxford University Press, 200.
- [3] Goody R, *Principles of Atmospheric Chemistry and Physics*, Oxford University Press, 1995.
- [4] Brasseur G P, Orlando J J and Tyndall G S, *Atmospheric Chemistry and Global Change*, Oxford University Press, 1999.
- [5] Hester R E and Harrison R M, *Volatile Organic Compounds in the Atmosphere*, RSC: Issues in Environmental Science and Technology, Royal Society of Chemistry, Cambridge, 1995.
- [6] Jacobson M Z, *Atmospheric Pollution*, Cambridge University Press, 2002.
- [7] Atkinson R 2000 Atmospheric chemistry of VOCs and NO_x *Atmos. Environ.* **34**, 2063-101.
- [8] Lindley R E, *Development of Diode laser-based optical sensors for quantitative trace gas analysis*, PhD Thesis, University of Bristol, UK, 2007.
- [9] Pradhan M, *Development of a diode-laser based optical sensor for continuous monitoring of trace gases in the atmosphere*, PhD Thesis, University of Bristol, UK, 2008.
- [10] Khalil M 1999 Non-CO₂ greenhouse gases in the atmosphere *Annu. Rev. Energy. Environ.* **24**, 645-61.
- [11] Schulze E D, Luyssaert S, Ciais P, Freibauer A, Janssens I A *et al.* 2009 Importance of methane and nitrous oxide for Europe's terrestrial greenhouse-gas balance *Nature Geoscience* 842-850.
- [12] Dacey J W H and Klug M J 1979 Methane Efflux from Lake Sediments Through Water Lilies *Science* **203(4386)**, 1253-5.

- [13] Ménard C, Ramirez A A, Nikiema J and Heitz M 2012 Biofiltration of methane and trace gases from landfills: a review *Environ. Rev.* **20**, 40–53.
- [14] Judd A G 2003 The global importance and context of methane escape from the seabed *Geo-Mar Lett.* **23**, 147-54.
- [15] Frenzel P and Rudolph J 1998 Methane emission from a wetland plant: the role of CH₄ oxidation in *Eriophorum Plant and Soil* **202**, 27-32.
- [16] Yeh S 2007 An empirical analysis on the adoption of alternative fuel vehicles: the case of natural gas vehicles *Energy Policy* **35**, 5865–75.
- [17] Blasing T J, *Recent greenhouse gas concentrations* (Carbon Dioxide Information Analysis Center (CDIAC), Oak Ridge National Laboratory, USA), 2009.
- [18] Nassar R and Bernath P 2003 Hot methane spectra for astrophysical applications *J Quant Spectrosc Radiat Transf* **82**, 279–92.
- [19] Nelson P F, Quigley S M and Smith M Y 1983 Sources of atmospheric hydrocarbons in Sydney: A quantitative determination using a source reconciliation technique *Atmos. Environ.* **17**, 439-49.
- [20] Seinfeld J H and Pandis S N, *Atmospheric Chemistry and Physics*, Wiley Interscience: New York, 1998.
- [21] Kanakidou M, Bonsang B, Le Roulley J C, Lambert G, Martin D and Sennequier G 1988 Marine source of atmospheric acetylene *Nature* **333**, 51– 2.
- [22] Frenklach M 2002 Reaction mechanism of soot formation in flames. *Phys Chem Chem Phys* **4**, 2028–37.
- [23] Luch A 2005 *Polycyclic aromatic hydrocarbon-induced carcinogenesis-an introduction*. The carcinogenic effects of polycyclic aromatic hydrocarbons 1–18.
- [24] He Q, Zheng C, Liu H, Li B, Wanga Y, Tittel F K 2016 A near-infrared acetylene detection system based on a 1.534 μm tunable diode

laser and a miniature gas chamber *Infrared Physics & Technology* **75**, 93–9.

[25] Hargreaves R J, Beale C A, Michaux L, Irfan M and Bernath P F 2012 Hot Methane Line Lists For Exoplanet And Brown Dwarf Atmosphere *The Astrophysical Journal* **757(46)**, (10pp).

[26] Rothman L, Gordon I, Babikov Y, Barbe A, Chris Benner D, Bernath P, Birk M, Bizzocchi L, Boudon V, Browni L R, Campargue A, Chance K, Cohen E A, Coudert L H, Devi V M, Drouin B J, Fayt A, Flaud J M, Gamachem R R, Harrison J J, Hartmann J M, Hill C, Hodges J T, Jacquemart D, Jolly A, Lamouroux J, LeRoy R J, Li G, Long D A, Lyulin O M, Mackie C J, Massie S T, Mikhailenko S, Müller H S P, Naumenko O V, Nikitin A V, Orphal J, Perevalov V, Perrin A, Polovtseva E R, Richard C, Smith M A H, Starikova E, Sung K, Tashkun S, Tennyson J, Toon G C, Tyuterev V I G and Wagner G 2013 The HITRAN 2012 molecular spectroscopic database *J Quant Spectrosc Radiat Transf* **130**, 4–50.

[27] Steinfeld J I, *Molecules and Radiation: An Introduction to Modern Molecular Spectroscopy* (Dover Reprint Edition, 2005).

[28] Thalakkotur L M, Prabhahari P, Sukhananazerin A and Biji P 2015 Technologies for Clinical Diagnosis Using Expired Human Breath Analysis *Diagnostics* **5**, 27-60.

[29] Wang C and Sahay P 2009 Breath Analysis Using Laser Spectroscopic Techniques: Breath Biomarkers, Spectral Fingerprints, and Detection Limits *Sensors* **9(10)**, 8230-8262.

[30] Modak A S 2007 Stable isotope breath tests in clinical medicine: a review *J. Breath Res.* **1**, 014003 (13pp).

[31] Amann A, Miekisch W, Schubert J, Buszewski B, Ligor T, Jezierski T, Pleil J and Risby T 2014 Analysis of Exhaled Breath for Disease Detection *Annu. Rev. Anal. Chem.* **7**, 455–82.

[32] Platt U, Perner D and Patz H W 1979 Simultaneous measurement of atmospheric CH₂O, O₃, and NO₂ by differential optical absorption *J. Geophys. Res.* **84**, 6329-35.

- [33] Allan B J, McFiggans G, Plane J M C and Coe H 2000 Observations of iodine monoxide in the remote marine boundary layer *J. Geophys. Res.* **105**, 14363-9.
- [34] Heard D E and Pilling M J 2003 Measurement of OH and HO₂ in the Troposphere *Chem. Rev.* **103**, 5163-98.
- [35] Hinkley E D 1970 High-resolution infrared spectroscopy with a tunable diode laser *Appl. Phys. Lett.* **16**, 351.
- [36] Herriott D R and Schulte H J 1964 Folded Optical Delay Lines *Appl. Opt.* **4**, 883-9.
- [37] Martin PA 2002 Near-infrared diode laser spectroscopy in chemical process and environmental air monitoring *Chem. Soc. Rev.* **31**, 201-10.
- [38] Werle P 1998 A review of recent advances in semiconductor laser based gas monitors *Spectrochimica. Acta A* **54**, 197-236.
- [39] Namjou K, Cai S, Whittaker E A, Faist J, Gmachl C, Capasso F, Siveo D L and Cho A Y 1998 Sensitive absorption spectroscopy with a room-temperature distributed-feedback quantum-cascade laser *Opt. Lett.* **23**, 219-21.
- [40] Kosterev A A and Tittle F K 2002 *IEEE J. Quant. Elect.* **38**, 82.
- [41] Harren F J M, Cotti G, Oomens J and Hekkert S te L in *Encyclopaedia of Analytical Chemistry*, ed. Meyers R A; John Wiley & Sons, Ltd, 2000; chapter: Photoacoustic Spectroscopy in Trace Gas Monitoring, pp. 2203-2226.
- [42] Miklos A and Hess P 2001 Application of acoustic resonators in photoacoustic trace gas analysis and metrology *Rev. Sci. Instrum.* **72**, 1937-1955.
- [43] Schilt S, Thevenaz L, Nikles M, Emmenegger L and Huglin C 2004 Ammonia monitoring at trace level using photoacoustic spectroscopy in industrial and environmental applications *Spectrochimica Acta A* **60**, 3259-68.

- [44] Paldus B A, Spence T G, Zare R N, Oomens J, Harren F J M, Parker D H, Gmachi C, Capasso F, Sivco D L, Baillargeon J N, Hutchinson A L and Cho A Y 1999 Photoacoustic spectroscopy using quantum-cascade lasers *Opt. Lett.* **24**, 178-80.
- [45] Heard D E, Pilling M J and Whitaker B J 1997 *J. Chem. Soc. Faraday Trans.* **93**, 2907.
- [46] Bloss W, Gravestock T J, Heard D E, Ingham T, Johnson G P and Lee J D 2003 Application of a compact all solid-state laser system to the in situ detection of atmospheric OH, HO₂, NO and IO by laser-induced fluorescence *J. Environ Monit.* **5**, 21-8.
- [47] O'Keefe A and Deacon D A G 1988 Cavity ring-down optical spectrometer for absorption measurements using pulsed laser sources *Rev. Sci. Instrum.* **59**, 2544-51.
- [48] Mazurenka M, Orr-Ewing A J, Peverall R and Ritchie G A D 2005 Cavity ring-down and cavity enhanced spectroscopy using diode lasers *Annu. Rep. Prog. Chem. Sect. C* **101**, 100-42.
- [49] O'Keefe A 1998 Integrated cavity output analysis of ultra-weak absorption *Chem. Phys. Lett.* **293**, 331-6.
- [50] Fawcett B L, Parkes A M, Shallcross D E and Orr-Ewing A J 2002 Trace detection of methane using continuous wave cavity ring-down spectroscopy at 1.65 μm *Phys. Chem. Chem. Phys.* **4**, 5960-5.
- [51] Wada R and Orr-Ewing A J 2005 Continuous wave cavity ring-down spectroscopy measurement of NO₂ mixing ratios in ambient air *Analyst* **130**, 1595-1600.
- [52] Ball S M and Jones R L 2003 Broad-band cavity ring-down spectroscopy *Chem. Rev.* **103**, 5239-62.
- [53] Morville J, Romanini D, Kachanov A A and Chenevier M 2004 Two schemes for trace detection using cavity ringdown spectroscopy *Appl. Phys.* **78**, 465-76.

- [54] Braithwaite A and Smith F J, *Chromatographic Methods*, Blackie Academic and Professional, 1995.
- [55] Gorb R L and Barry E F, *Modern Practice of Gas Chromatography*, Willey, 2004.
- [56] Hopkins J R, Lewis A C and Read K A 2003 A two-column method for long-term monitoring of non-methane hydrocarbons (NMHCs) and oxygenated volatile organic compounds (o-VOCs) *J. Environ. Monit.* **5**, 8-13.
- [57] Baroja O, Goicolea M A, Sampedro M C, Rodriguez E, Balugera Z G de, Alonso A and Barrio R J 2004 Multisorbent tubes sampling used in thermal desorption cold trap injection with gas chromatography-mass spectrometry for C₂-C₆ hydrocarbon measurements in an urban atmosphere *Intern. J. Environ. Anal. Chem.* **84**, 341-53.
- [58] Leibrock E and Slemr J 1997 *Atmos. Environ.* **31**, 3329-39.
- [59] Rivett A C, Martin D, Nickless G, Simmonds P G, O'Doherty S J, Gray D J and Shallcross D E 2003 *Atmos. Environ.* **37**, 2221-35.
- [60] Urhahn T and Ballschmiter K 2000 Analysis of halogenated C₁/C₂-trace compounds in marine atmosphere *Fresenius J. Anal. Chem.* **366**, 365-7.
- [61] Hansel A 2004 Proton Transfer Mass Spectrometer *Europhysics News* **35**(6), 197-9.
- [62] Lindinger W, Jordon A and Hansel A 1998 *Chem. Soc. Rev.* **27**, 247-354.
- [63] Warneke C, Veen van der, Luxembourg S, Gouw A de and Kok A 2001 *Int. J. Mass Spectrom.* **207**,167-82.
- [64] Lindinger W, Hansel A and Jordon A 1998 *Int. J. Mass Spectrom. Ion Process.* **173**, 191-241.

Chapter 2

Development of Cavity Ring-Down Spectroscopy coupled with a continuous wave external-cavity quantum cascade laser for trace detection of methane isotopes

2.1 Introduction

Cavity enhanced absorption techniques have been introduced in the Chapter 1. The high-finesse optical cavity enhanced absorption techniques [1,2], such as integrated cavity output spectroscopy (ICOS) [3] and cavity ring-down spectroscopy (CRDS) [4] have widely been employed to achieve ultra-high sensitivity of 10^{-9} - 10^{-11} cm⁻¹, thus facilitating the measurement capability of trace molecular species as low as parts-per-trillion (ppt) levels. CRDS is an ultra-sensitive optical absorption technique where decay-rate of optical signal, trapped in a high-finesse optical cavity is utilized for ultra-low and high-precision measurements of molecular concentration. In CRDS method, time-domain measurements are advantageous, being insensitive to shot-to-

shot laser intensity fluctuations and free from any secondary calibrations in contrast to ICOS technique, where time-integrated light intensity across the molecular transition provides the absorption features.

CRDS combines the advantageous features of traditional absorption spectroscopy, such as species selectivity, quantitative and non-intrusive measurement and possibility of remote sensing with a fast-time response and ultra-high sensitivity. Therefore, CRDS technique, first introduced by O'Keefe and Deacon in 1988 [5], has been modified greatly in the recent years and has found numerous applications in molecular spectroscopy [6], kinetic studies [7], breath diagnostics [8], environmental monitoring [9,10], and process monitoring in hostile environment such as plasmas [11,12] and flames [13]. CRDS has been used extensively in the study of gaseous sample, but has also been applied to liquids [14,15], thin films [16], surfaces [17] and solids [18].

Moreover, the recent progress in quantum cascade laser (QCL) technology provides the access to almost entire mid-IR region (i.e. 4-25 μm) [19,20]. The mid-infrared (mid-IR) spectral region is considered to be the "molecular fingerprint" region with strong characteristic fundamental and combinational vibrational transitions of trace molecules, which are several orders stronger than the overtone bands in the NIR and hence offers enhanced sensitivity. Additionally, the unique features of QCL, like room-temperature operation, large mode-hop-free (MHF) tuning range, high-power and highly collimated light source with narrow line-width, make it an attractive choice compared to the NIR lasers or the cryogenic mid-IR sources for high-resolution spectroscopy and gas sensing applications like environmental research and breath analysis. Therefore, the development of CRDS using continuous wave (*cw*) QCLs offers the possibility of developing compact, lightweight, highly sensitive and field deployable sensor for atmospheric constituents and a modern medical diagnostic tool.

However, the reports of *cw* CRDS technique combined with the latest *cw* external cavity (EC)-QCL are still very limited in the mid-IR spectral region beyond 5 μm due to unavailability and prohibitively expensive

optical components such as optical isolator and acousto-optic modulator (AOM) [21]. In this context, the present chapter demonstrates the development of a *cw* CRDS technique coupled with a *cw* EC-QCL operating between 7.5 and 8 μm for selective and quantitative detection of trace gases in real-time and to study high-resolution molecular spectroscopy. The significance of the selected spectral region (i.e. 7.5-8 μm) has already been highlighted in section 1.5.2 of Chapter 1.

In this chapter, we first present the basic principle of CRDS and important parameters to form a stable optical cavity. In the subsequent sections, we demonstrate our developed experimental setup of *cw* CRDS coupled with a *cw* EC-QCL and validate the CRD spectrometer by ultra-sensitive direct detection of methane isotopes ($^{12}\text{CH}_4$ and $^{13}\text{CH}_4$) which served as a benchmark molecule in the selected spectral region with strong fundamental vibrational transitions (as presented in section 1.5.2).

2.2.1 Principle of CRDS operation

In CRDS spectrometer, two or more highly reflective ($R \geq 99.97\%$) mirrors form a high finesse and stable optical cavity (shown in Figure 2.1). The laser light injected into the cavity along the central axis is trapped inside the cavity and moves back and forth in between the two

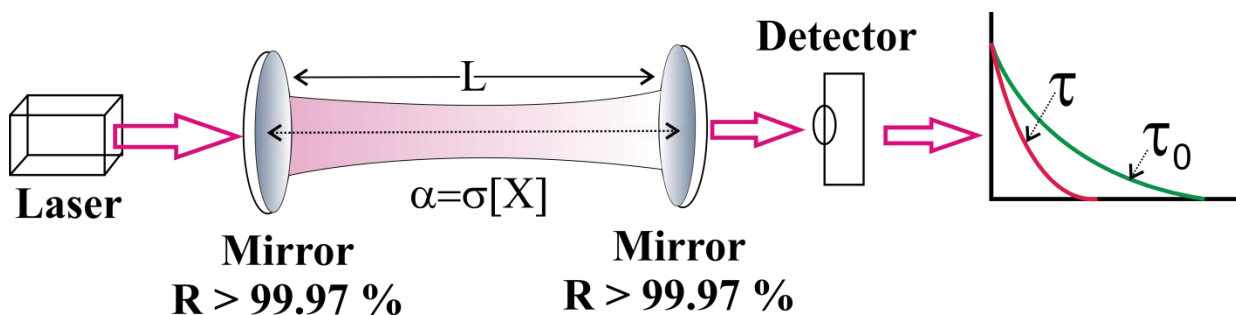


Figure 2.1 Schematic of a general cavity ring-down set up.

mirrors. Due to imperfection of high reflective coatings, a small portion of the trapped laser light is transmitted through each of the mirrors at every reflection. The light that is leaking out from the cavity is detected

as a function of time by a fast response detector placed behind one of the mirrors. In absence of any sample, detected light intensity decays exponentially, as expressed by the following Equation [22]:

$$\begin{aligned}
 I &= I_0 \cdot \exp\left[-\left(\frac{\text{Number of reflections}}{\text{round trip}}\right) \cdot \left(\frac{\text{Loss}}{\text{Reflection}}\right) \cdot (\text{Number of round trips})\right] \\
 &= I_0 \cdot \exp\left[-(2) \cdot (1-R) \cdot \left(\frac{tc}{2l}\right)\right] \\
 &= I_0 \cdot \exp\left[-\frac{(1-R) \cdot c}{l} \cdot t\right] \\
 &= I_0 \cdot \exp\left[-\frac{t}{\tau_0}\right]; \text{ where } \tau_0 = \frac{l}{(1-R) \cdot c} \quad (2.1)
 \end{aligned}$$

τ_0 is the time required for the light intensity exiting from the cavity to decay to $(1/e)$ value of its initial intensity in absence of any sample and is called empty cavity ring-down time (RDT), l is the length of the cavity, R is the mirror reflectivity and c is the speed of light. The decay rate (k) is termed as inverse of the ring-down time i.e.

$$k_0 = \frac{1}{\tau_0} \quad (2.2)$$

Therefore, the effective optical pathlength ($l_{\text{effective}}$) inside the cavity becomes:

$$l_{\text{effective}} = \tau_0 \cdot c \quad (2.3)$$

As an example, for mirror with $R = 0.99988$, a typical value for the current mirror coatings, $l = 0.5$ m, $\tau_0 = 14.2$ μs

$$l_{\text{effective}} \approx 4.2 \text{ kilometre}$$

Now, in presence of gas sample inside the cavity, as the laser light is tuned into resonance with absorption feature of the sample, the exponential decay of light intensity becomes faster, described by the following Equation [22]:

$$\begin{aligned}
I &= I_0 \cdot \exp\left[-(1-R) \cdot \left(\frac{tc}{l}\right) + \left(\frac{\text{Absorption loss}}{\text{round trip}}\right) \cdot (\text{Number of round trips})\right] \\
&= I_0 \cdot \exp\left[-(1-R) \cdot \left(\frac{tc}{l}\right) + (2 \cdot \alpha \cdot d) \cdot \left(\frac{tc}{2l}\right)\right] \\
&= I_0 \cdot \exp\left[-\frac{tc}{l} \{(1-R) + \alpha \cdot d\}\right] \\
&= I_0 \cdot \exp\left[-\frac{t}{\tau}\right]; \text{ where } \tau = \frac{1}{c} \left[\frac{l}{(1-R) + \alpha \cdot d}\right] \quad (2.4)
\end{aligned}$$

Here d is the sample length which is equal to l in our experiment, α is the absorption coefficient, defined by

$$\alpha = \sigma_{\lambda} \cdot [X] \quad (2.5)$$

where σ_{λ} is the wavelength dependent absorption cross-section and $[X]$ is the concentration of the sample.

From Equations 2.1 and 2.4, we can say that RDT depends only on mirror reflectivity, cavity length and absorption by the medium inside the cavity. Consequently, RDT is independent of laser intensity and hence it is not influenced by the laser intensity fluctuations.

If τ and τ_0 are acquired as a function of laser frequency during the experiment, the absorption spectrum of a sample within the cavity can be derived without the need for further calibration using the following Equation:

$$\alpha = \sigma_{\lambda} \cdot [X] = \frac{\Delta k}{c}; \text{ where } \Delta k = \frac{1}{\tau} - \frac{1}{\tau_0} \quad (2.6)$$

Here, Δk is the change in ring-down decay rate coefficient (in sec^{-1}) of the cavity in presence of the absorbing sample. The absorption spectra of a gas sample is achieved by plotting the ring-down decay rate (k) against the wavenumber (cm^{-1}) of the laser for a specific molecular transition and subsequently the area under the spectra is exploited to calculate the sample concentration from the knowledge of the absorption cross-section for the transition. Otherwise, if the absorption cross-section of a

molecular species is known at particular wavelength, the concentration of the molecules can easily be calculated from measured changes in the RDT or rate coefficient in the presence and absence of the sample.

2.2.2 Sensitivity of CRDS

CRDS is an ultra-sensitive absorption method and it is useful to define the sensitivity limit of the spectrometer. The sensitivity limit of a CRDS sensor is generally expressed in the form of minimum detectable absorption coefficient (α_{\min}) by

$$\alpha_{\min} = \frac{1}{c \tau_0} \frac{\Delta \tau_{\min}}{\tau_0} \quad (2.7)$$

where $\Delta \tau_{\min}$ is the minimum detectable change in the cavity ring-down time and $(\Delta \tau_{\min}/\tau_0)$ corresponds to the relative error of the ring-down time measurements. For a CRDS spectrometer, when scanning across an absorption line, typically the limiting sensitivity is of the order of $\sim 10^{-8}$ - 10^{-9} cm^{-1} . Again, α_{\min} can directly be converted to a minimum detectable concentration by dividing it by the wavelength dependent peak absorption cross-section; this minimum concentration is referred to as the detection limit of the spectrometer in CRDS

$$[X_{\min}] = \frac{\alpha_{\min}}{\sigma_{\lambda}} \quad (2.8)$$

The detection limit of the spectrometer can often be denoted in terms of a *mixing ratio* expressed in ppbv (10^{-9}) or pptv (10^{-12}) at 1 atmosphere pressure in a bulk gas such as air. In that case, we have to consider the line specific pressure broadening coefficient in the calculation because of the pressure broadening effect which reduces absorption cross-sections at a given wavelength. Alternatively, the sensitivity of the CRDS spectrometer is often defined as noise-equivalent absorption coefficient (NEA) expressed as

$$NEA = \sqrt{\frac{2}{f_{rep}}} \alpha_{min} \quad (2.9)$$

where f_{rep} is the data acquisition rate [23]. The NEA coefficient is typically expressed in unit of $\text{cm}^{-1}\text{Hz}^{-1/2}$. The NEA incorporates the effect of data acquisition rate and is improved by high data acquisition rates. The typical value of NEA for a CRDS spectrometer varies from 10^{-8} to $10^{-11} \text{ cm}^{-1}\text{Hz}^{-1/2}$.

2.2.3 Mode Structure of an Optical Cavity

A high finesse cavity acts as a Fabry-Perot resonator supporting only specific longitudinal modes. For a longitudinal mode to propagate in an optical cavity, it must satisfy the condition that the total phase change for a complete round trip is an integer multiple of 2π . The frequency spacing between two consecutive longitudinal modes, $\Delta\nu$, is given in Equation 2.10 and depends on the time taken for the light to complete a round trip within the cavity, t .

$$\Delta\nu = \frac{1}{t} = \frac{c}{2l} \quad (2.10)$$

This frequency spacing is also referred to as the free spectral range (FSR) of the cavity. For a high finesse cavity with length $l=50 \text{ cm}$, the FSR is equal to 300 MHz or 0.01 cm^{-1} .

The widths of the cavity modes depend on the reflectivity of the mirrors and the sharpness of the modes eventually determines the mode maxima and thus decay time. The width of the cavity modes can be evaluated from the finesse of the cavity, F , which is given in Equation 2.11.

$$F = \frac{\pi\sqrt{R}}{(1-R)} \quad (2.11)$$

From this, the FWHM of the cavity modes, $\Delta\nu_{1/2}$, can be calculated using Equation 2.12.

$$\Delta\nu_{1/2} = \frac{\Delta\nu}{F} \quad (2.12)$$

Thus, for a cavity with mirrors of reflectivity $R=0.99988$ which are separated by $l=50$ cm, the finesse of the cavity, $F\sim 26\times 10^3$ and the FWHM of the cavity modes, $\Delta\nu_{1/2}=11.46$ kHz.

In a pulsed CRDS operation, the mode matching between the frequencies of the cavity modes and the laser frequency is not required as the laser bandwidth, which is typically ≥ 500 MHz, is often greater than the FSR of a cavity, illustrated in Figure 2.2. In contrast, the bandwidth of a *cw* diode laser is much less, typically ~ 4 MHz, and hence the overlap

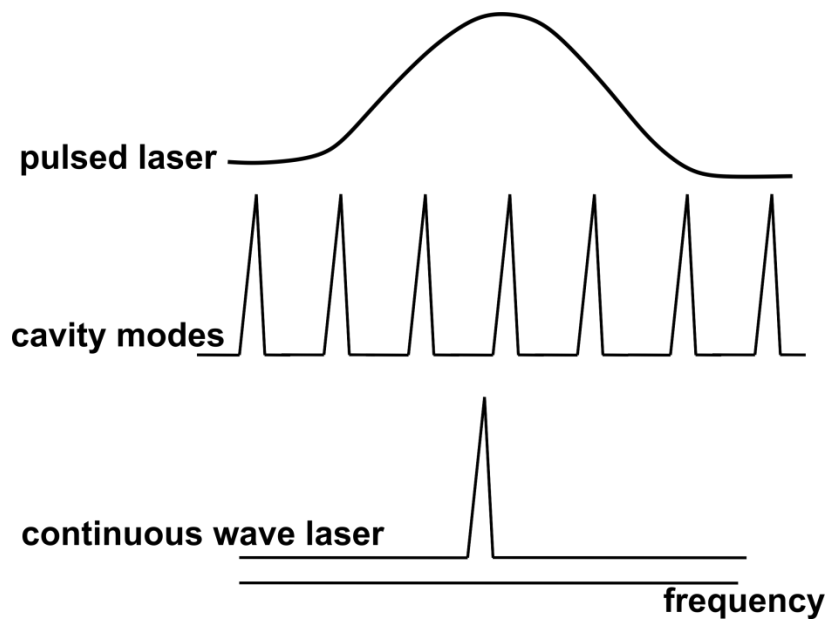


Figure 2.2 Schematic of a typical free spectral range (FSR) of a high finesse optical cavity in comparison to the typical bandwidths of pulsed and continuous wave lasers.

between the cavity modes and the frequency of the laser is less likely to occur. Mode matching technique may be employed to ensure light intensity build up within the optical cavity.

The most common method of mode matching utilized in *cw* CRDS is to modulate the position of one of the cavity mirrors, and thus the cavity length. If the mirror position is modulated by more than the FSR of the cavity, laser radiation will couple into the cavity at all frequencies. The mirror position can be modulated by attaching it to a piezo-electric transducer (PZT) which translates the mirror uniformly. Figure 2.3 shows a triangular voltage function input to a PZT and the resultant build-up of light intensity that occurs when the fixed laser frequency coincides with a mode of the cavity.

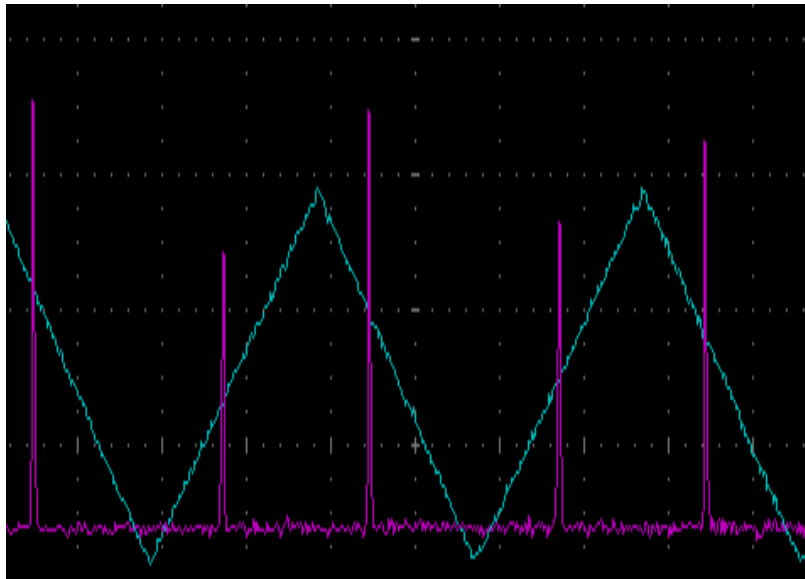


Figure 2.3 A screen-shot of an oscilloscope showing TEM_{00} modes during experiment. The spikes represent the on resonance laser intensity build-up inside the cavity when the cavity length is modulated by a triangular voltage function as shown in the screen.

The optimum alignment for a high finesse cavity is with the mirrors positioned perfectly parallel to one another and the laser beam travelling perpendicular to the mirror faces and passing through the centre of each mirror along the cavity axis. The transverse electromagnetic mode (TEM) occupying this path is called TEM_{00} . Excitation of higher order modes is also possible. If the cavity is not well aligned, other transverse modes may propagate through the cavity. The TEM_{00} mode has a Gaussian radial distribution of intensity.

2.2.4 Stable Cavity Construction

A stable optical resonator that is capable of maintaining a long effective pathlength, is the critical criterion for achieving CRDS. Some important properties of the laser beam must be defined before designing of such an optical resonator.

A laser beam may be expressed as a Gaussian beam propagating along a z-axis as shown in Figure 2.4 [24-26]. The main parameter characterizing a beam is the beam waist, ω_0 , that lies at a reference plane $z=0$. The diameter of the waist, $2\omega_0$, is called the spot size. At this point, the radius of curvature of the wavefront, R , is infinite in the propagation direction.

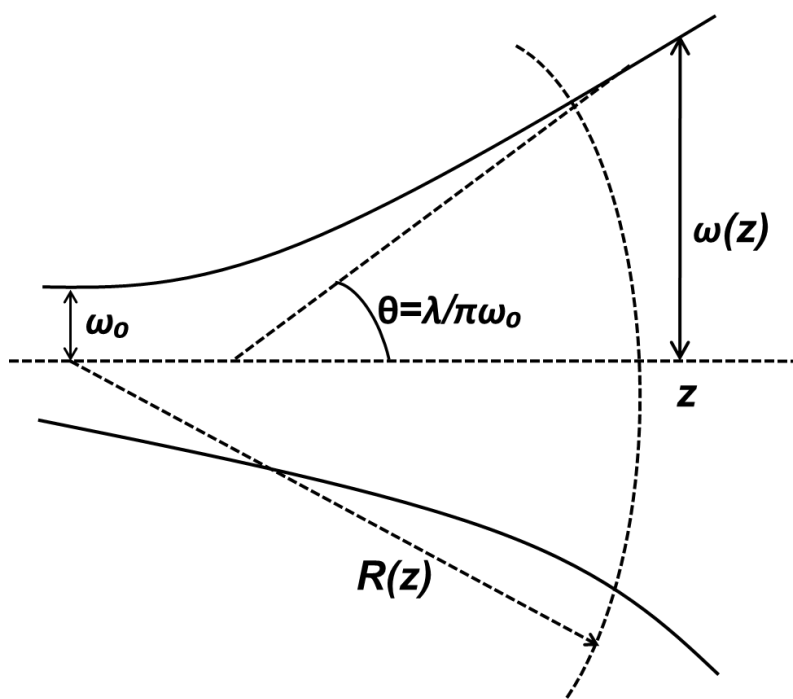


Figure 2.4 A schematic of a Gaussian beam propagating along the z axis.

The distance from the beam waist at which the beam diameter is increased approximately by $\sqrt{2}$ and the beam area gets doubled is called the Rayleigh range (z_R). Equation 2.13 describes the Rayleigh range and signifies that a beam with a larger waist and a shorter wavelength would have a higher z_R , and hence would be more collimated. The Gaussian beam is nearly parallel near the beam waist, with a same cross-section as that at the beam waist. At further distances, when $z \gg z_R$, the

beam radius increases approximately linearly along the z axis with an angular divergence θ .

$$z_R = \frac{\pi\omega_0^2}{\lambda} \quad (2.13)$$

Other beam parameters such as the beam spot size, $\omega(z)$ at a distance z , and the radius of curvature of the beam at the wavefront, R , can be expressed in terms of the beam waist and Rayleigh range, as given in Equations 2.14 and 2.15.

$$\omega(z) = \omega_0 \sqrt{1 + \left(\frac{z}{z_R}\right)^2} \quad (2.14)$$

$$R = z + \frac{z_R^2}{z} \quad (2.15)$$

In an optical cavity resonator consisting of two mirrors, M_1 and M_2 , separated by a distance L , the radii of curvature of the mirrors, R_1 and R_2 , must match with the wavefront curvature of a Gaussian beam for the

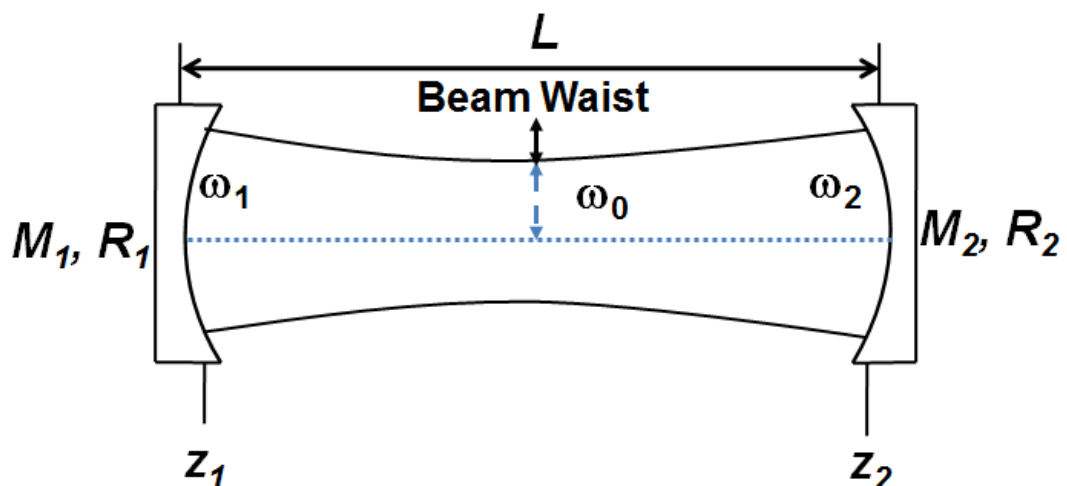


Figure 2.5 A schematic of a two-mirror resonator supporting the propagation of a Gaussian wave.

beam to propagate through the cavity. In this orientation, the Gaussian beam will have a specific beam waist and the mirrors will be situated at distance z_1 and z_2 from the beam waist, as shown in Figure 2.5.

The stability of an optical cavity can be more conveniently described by two resonator g parameters, g_1 and g_2 , defined in Equation 2.16.

$$g_1 = 1 - \frac{L}{R_1} \quad \text{and} \quad g_2 = 1 - \frac{L}{R_2} \quad (2.16)$$

The Rayleigh range, location of the two mirrors and beam waist of a Gaussian beam can be expressed in terms of the resonator g parameters, as given in Equations 2.17, 2.18 and 2.19, respectively.

$$z_R^2 = \frac{g_1 g_2 (1 - g_1 g_2)}{(g_1 + g_2 - 2g_1 g_2)^2} L^2 \quad (2.17)$$

$$z_1 = \frac{g_2 (1 - g_1)}{(g_1 + g_2 - 2g_1 g_2)} L \quad \text{and} \quad z_2 = \frac{g_1 (1 - g_2)}{(g_1 + g_2 - 2g_1 g_2)} L \quad (2.18)$$

$$\omega_0^2 = \frac{L\lambda}{\pi} \sqrt{\frac{g_1 g_2 (1 - g_1 g_2)}{(g_1 + g_2 - 2g_1 g_2)^2}} \quad (2.19)$$

The spot sizes of the beam at either end of the resonator, ω_1 and ω_2 can also be written in terms of g_1 and g_2 and are given in Equation 2.20.

$$\omega_1^2 = \frac{L\lambda}{\pi} \sqrt{\frac{g_2}{g_1 (1 - g_1 g_2)}} \quad \text{and} \quad \omega_2^2 = \frac{L\lambda}{\pi} \sqrt{\frac{g_1}{g_2 (1 - g_1 g_2)}} \quad (2.20)$$

These Equations clearly depict that the real and finite solutions for Gaussian beam parameters can only exist if g_1 and g_2 are confined to a stable range, $0 \leq g_1 g_2 \leq 1$. Figure 2.6 shows the stability diagram for a two-mirror optical resonator.

The shaded region on the stability diagram depicts all two-mirror cavities that would form an optically stable resonator. The points outside the shaded region correspond to unstable two-mirror cavities.

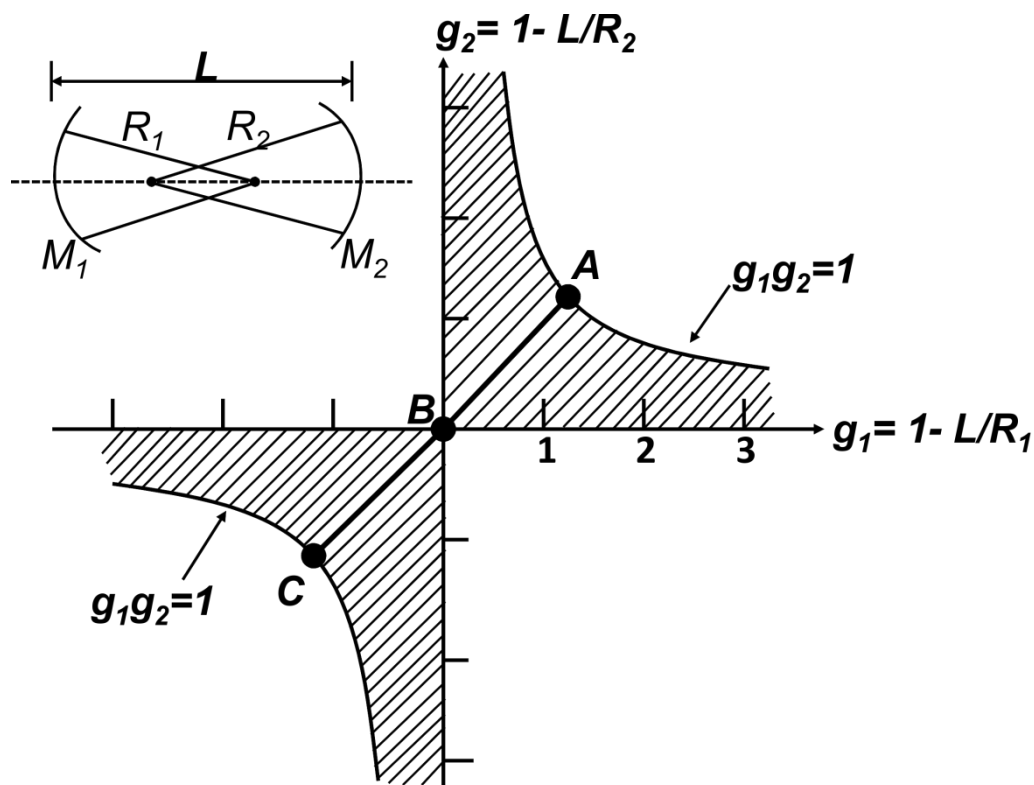


Figure 2.6 A stability diagram for a two-mirror optical resonator.

If the resonator consists of two mirrors with equal radii of curvature, $R_1=R_2=R$, then the system will lie along the $+45^\circ$ diagonal within the shaded region, shown in Figure 2.6. There are three points of interest on the stability diagram for a two-mirror cavity, labelled as A, B and C in Figure 2.6.

Point A in Figure 2.6 denotes a cavity with near-planar mirrors with $R_1=R_2\approx\infty$ and $g_1=g_2\approx 1$. In this configuration, the Gaussian beam will have a very long and large waist, with large spot on each of the mirrors.

The central point B represents a symmetric confocal cavity with $R_1=R_2=L$ and $g_1=g_2=0$. Here, the beam is focused at the centre of the cavity by the two mirrors whereas the mirrors lie exactly at the two Rayleigh ranges. This cavity configuration is relatively insensitive to mirror misalignment and has a small beam diameter along the length of the cavity.

Position C on the stability diagram depicts a near-concentric or spherical cavity where the cavity length, L , is less than the sum of the two radii of curvature R_1+R_2 by a small amount δL . For a near-concentric resonator, $R_1 \approx R_2 \approx R = (L/2)$ and $g_1 \approx g_2 = 1 - \delta L/R$. The beam waist is small in this case and the spot size on each mirror is large.

2.2.5 Continuous wave Cavity Ring-Down Spectroscopy

After the successful coupling between the laser frequency and the frequencies of the cavity modes, the laser radiation inside the cavity is required to be extinguished for achieving a single exponential decay of the light intensity. If the laser continues to radiate, the laser frequency will continue to couple into the cavity whilst it is in resonance, and may interfere with the exponential decay. In pulsed CRDS operation, decay signal is achieved at the off-period between two consecutive pulses and hence external switching is not required. In *cw* CRDS, laser radiation is extinguished by using a fast optical switch, such as an acousto optic modulator (AOM), combined with a trigger circuit. A user specified, predefined threshold intensity is set on the trigger generator, and when the light intensity inside the cavity reaches the value, the trigger is sent to the AOM. The AOM cuts off the first order diffracted beam input to the cavity, thus allowing the light intensity to decay in an unperturbed, first-order exponential. Figure 2.7 illustrates an experimental ring-down decay trace.

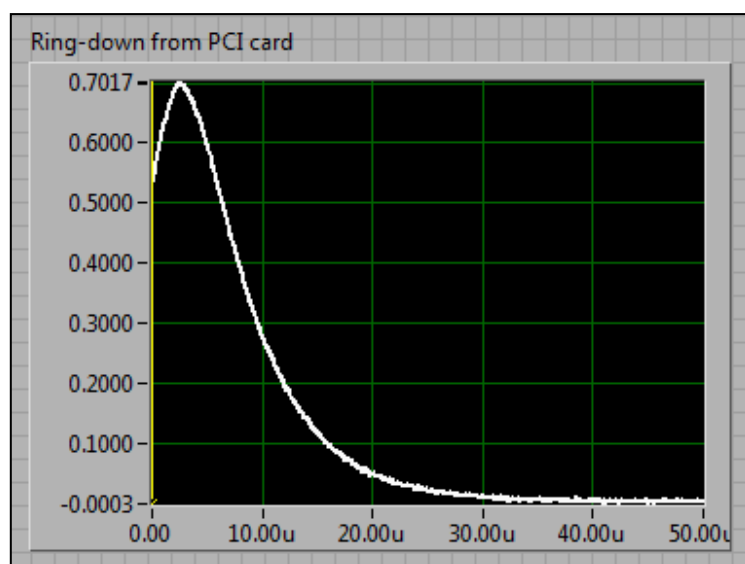


Figure 2.7 An experimental ring-down trace acquired by a PCI card.

There are few advantages of using a *cw* laser source. The spatial resolution in CRDS is limited by the bandwidth of the laser and bandwidth of a *cw* laser is much less than the pulsed laser. There is also an increased intensity build up for a *cw* laser as the laser frequency is in resonance with a cavity mode for longer time periods due to narrow bandwidth and thereby increasing the S:N ratio of the subsequent ring-down decays.

2.3 Overview of Diode and Quantum Cascade Lasers

Diode lasers are the most common optical sources for the radiation ranging from visible to near IR spectral region. The fundamental working principle of a diode laser is the interband transition of an electron from conduction band to valence band of a semiconductor material releasing a photon in the process of electron-hole recombination in the valence band. The bandgap energy of the semiconductor material determines the wavelength of the emitted photon. Therefore, the radiation wavelength of a diode laser can easily be controlled with the use of widely different semiconductor materials having different bandgap energies. However, lasing of a diode laser is mostly restricted into the near IR and ultimately the reliance on the bandgap becomes the limiting factor for the lasing in mid IR spectral

region. The reason is that the bandgap is required to be reduced for lasing in the longer wavelength range and as the bandgap shrinks, the operation of a semiconductor laser becomes very critical due to the effects of thermal runaway and thermal recycling [20]. Moreover, chemical bonds of a material become weaker with the decrease of bandgap, which eventually introduces defects during growth and device fabrication.

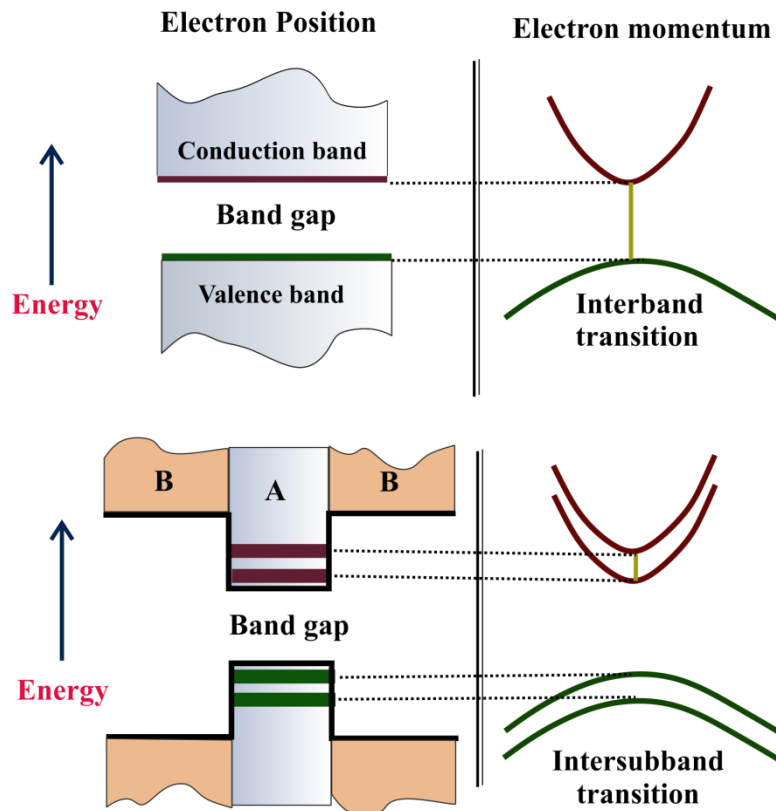


Figure 2.8 An illustration of the differences between (interband) diode laser and (intersubband) quantum cascade laser. The yellow line shows the electronic transition associated with a photon release for the respective cases.

Quantum cascade laser (QCL) is a new-generation optical source which revolutionizes the fundamental principle of light emission (Figure 2.8). A QCL is a unipolar device where a photon is generated by the intersubband transition of an electron within the conduction band [27]. The intersubbands are the quantum wells created artificially by stacking alternative layers of semiconductor materials of nanometric thickness. Hence, the emission wavelength of a QCL is independent of bandgap and depends on the properties of the layers. After an electron undergoes

an intersubband transition, it reaches to the next period by quantum mechanical tunnelling where the same process is repeated and another photon is generated. Therefore, multiple photons are generated by a single electron as it traverses QCL structure and this leads to a higher power than the semiconductor laser diodes. The unique feature of a QCL is that the emission wavelength primarily depends on the thickness of the heterostructure layers. Hence, a QCL can operate on a wide spectral region ranging from mid to far IR and terahertz regime.

In 1994, QCL was first demonstrated experimentally by the group at Bell Labs (Murray Hill, NJ, USA). After the first demonstration, QCL design went through rapid and revolutionary changes with the help of quantum engineering. The recent advancements in sophisticated laser technology, i.e. continuous wave external cavity quantum cascade laser (*cw* EC-QCL), opens up a new frontier providing the access to almost entire mid-IR region ranging from 3-25 μm and thus enabling us to explore the high-resolution fundamental vibrational transitions of molecules with unprecedented selectivity of the spectral region. Moreover, high power, extremely narrow laser line-width, mode-hop-free and broad spectral tunability along with the room-temperature operation and compactness make the *cw* EC-QCL a unique and attractive candidate for chemical and bio-medical sensing, and high-resolution molecular spectroscopic studies.

In this chapter, a *cw* EC-QCL with mode-hop-free tuning range of 1257-1341 cm^{-1} is utilized for atmospheric trace gas sensing in combination with the ultra-sensitive *cw* cavity ring-down spectroscopy (*cw* CRDS). A diode laser based cavity enhanced absorption spectroscopy is exploited in the Chapters 4-7 for the measurements of CO_2 isotopes (i.e. $^{12}\text{CO}_2$, $^{13}\text{CO}_2$ and $^{12}\text{C}^{18}\text{O}^{16}\text{O}$) at $\sim 2.051 \mu\text{m}$.

2.4 Experimental Setup

The experimental set-up is depicted in Figure 2.9. A room temperature water-cooled *cw* EC-QCL (MHF-41078; Daylight Solutions, USA) with mode-hop-free (MHF) tunability between 7.5 μm and 8 μm (1341 cm^{-1} - 1257 cm^{-1}) was utilized as a high-resolution ($<0.0003\text{ cm}^{-1}$) and high power ($<100\text{ mW}$) optical source for *cw* CRDS sensor. The highly collimated laser light was first allowed to pass through an optical isolator (FIO-5-7.8; Innovation Photonics) and subsequently through an acousto-optic modulator (AOM; AGM406B11M; IntraAction Corp; USA) which acts as an optical Bragg-diffractor to produce zeroth-order and first-order laser beams. The zeroth-order beam was directed to a wavemeter (621B-MIR; Bristol Instruments) for real-time and continuous monitoring of laser wavelength with an accuracy of $\pm 0.001\text{ cm}^{-1}$, whereas

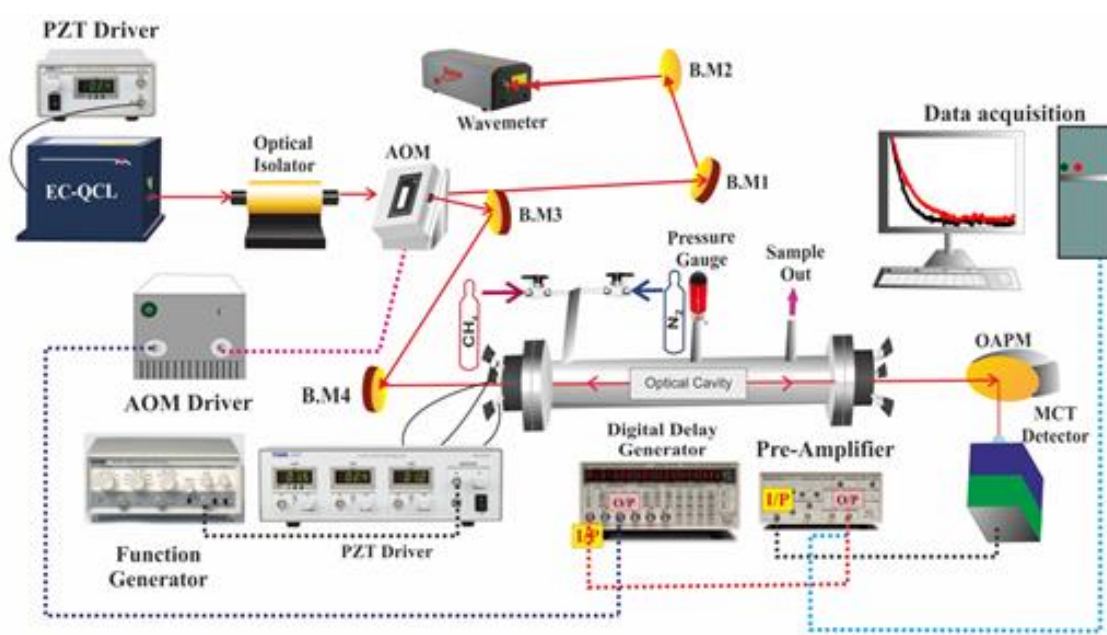


Figure 2.9 A schematic representation of the experimental set-up.

the first-order beam was precisely aligned along the central-axis of the optical cavity. The high-finesse cavity was formed by placing two high-reflective (HR) mirrors (CRD Optics Inc.; USA) with manufacturer specified reflectivity of $R > 99.98\%$ at $7.35\text{ }\mu\text{m}$ and 1 metre radius of curvature (ROC) at the two ends of a 50 cm long quartz-coated ring-

down cell (RDC). The optical signal was finally focused on to a four-stage thermo-electrically cooled photovoltaic mercury-cadmium-telluride (MCT) detector (PVI-4TE-8-1X1; Vigo System S.A.) using a gold-coated 90° off-axis parabolic mirror (50338 AU; Newport Corporation). The detector was further connected to an external low-noise voltage pre-amplifier (SR560; Stanford Research Systems) for amplification of electrical signal.

We next utilized cavity-length modulation technique to achieve the periodic resonance between laser mode and cavity mode. We applied ~60 Volt in parallel to the three piezoelectric transducers (PZT, Thorlabs PE4) attached to the front mirror-mount, using a triangular ramp function ($V_{pp}= 2.91V$, 50 Hz, 15x gain), to modulate the length of the cavity over one free-spectral-range (FSR) or half of the wavelength ($\lambda/2$). An intra-cavity light intensity (TEM₀₀ mode) was built-up periodically inside the optical cavity when the frequency of cavity mode matched with the laser mode frequency. The intra-cavity light intensity whenever reached to a pre-defined value, a pulse-delay generator (DG645; Stanford Research Systems) connected to the AOM driver was utilized to switch-off the first-order diffracted beam and an exponential decay of the intra-cavity light was observed. The exponential decay trace was captured by a high-speed (100 MS/s) data-acquisition card (5122 PCI National Instrument, 14-bit, 100 MHz bandwidth) and subsequently analysed by a custom-written LabVIEW program.

2.5 Results and Discussions

In the present EC-QCL based *cw* CRDS system, we achieved an empty cavity ring-down time of $\tau_0= 14.13 \mu s$ and standard deviation (1σ) of 0.56% with an averaging of 5 successive ring-down events. Based on these parameters the limiting sensitivity of the *cw* CRDS system was estimated to be $\alpha_{min}=1.32\times 10^{-8} \text{ cm}^{-1}$. As it was discussed later, this α_{min} translated into the detection limits for isotopic $^{12}\text{CH}_4$ and $^{13}\text{CH}_4$

molecules via the fundamental bending vibration of ν_4 band of 1.29×10^9 molecule cm^{-3} and 9.35×10^8 molecule cm^{-3} , respectively. With allowance of the broadening of spectral lines by an ambient pressure of 1 atm, these quoted detection limits would correspond to 52 pptv and 38 pptv, respectively for $^{12}\text{CH}_4$ and $^{13}\text{CH}_4$ isotopes of CH_4 . However, to assess the laser line-width, we modulated the cavity-length over one FSR to excite two successive TEM_{00} modes in a single piezo scanning (Figure 2.10a) and subsequently studied the individual TEM_{00} mode (Figure 2.10b). Thus, we obtained the time-scaled values of FSR (Δt_{FSR}) and individual TEM_{00} ($\Delta t_{\text{TEM}_{00}}$) mode. Then using the relation, $\Delta \gamma_{\text{QCL}} / \text{FSR} = \Delta t_{\text{TEM}_{00}} / \Delta t_{\text{FSR}}$ and the known value of FSR ($= c/2l$) of 300 MHz, we found the line-width of QCL ($\Delta \gamma_{\text{QCL}}$) of 13.66 MHz (i.e. 0.0004 cm^{-1}) which was in good agreement with the manufacturer specified linewidth (< 0.0003 MHz) of the current EC-QCL source. In contrast, the cavity line-width was measured to be $\Delta \gamma_{\text{Cavity}} = (\text{FSR} / \text{Finesse}) = 11.46 \text{ kHz}$. Therefore, the high-finesse ($F \sim 26000$) optical cavity coupled with an extremely narrow linewidth of *cw* EC-QCL provided an excellent platform for high-resolution and high-sensitivity spectral study of molecular absorptions.

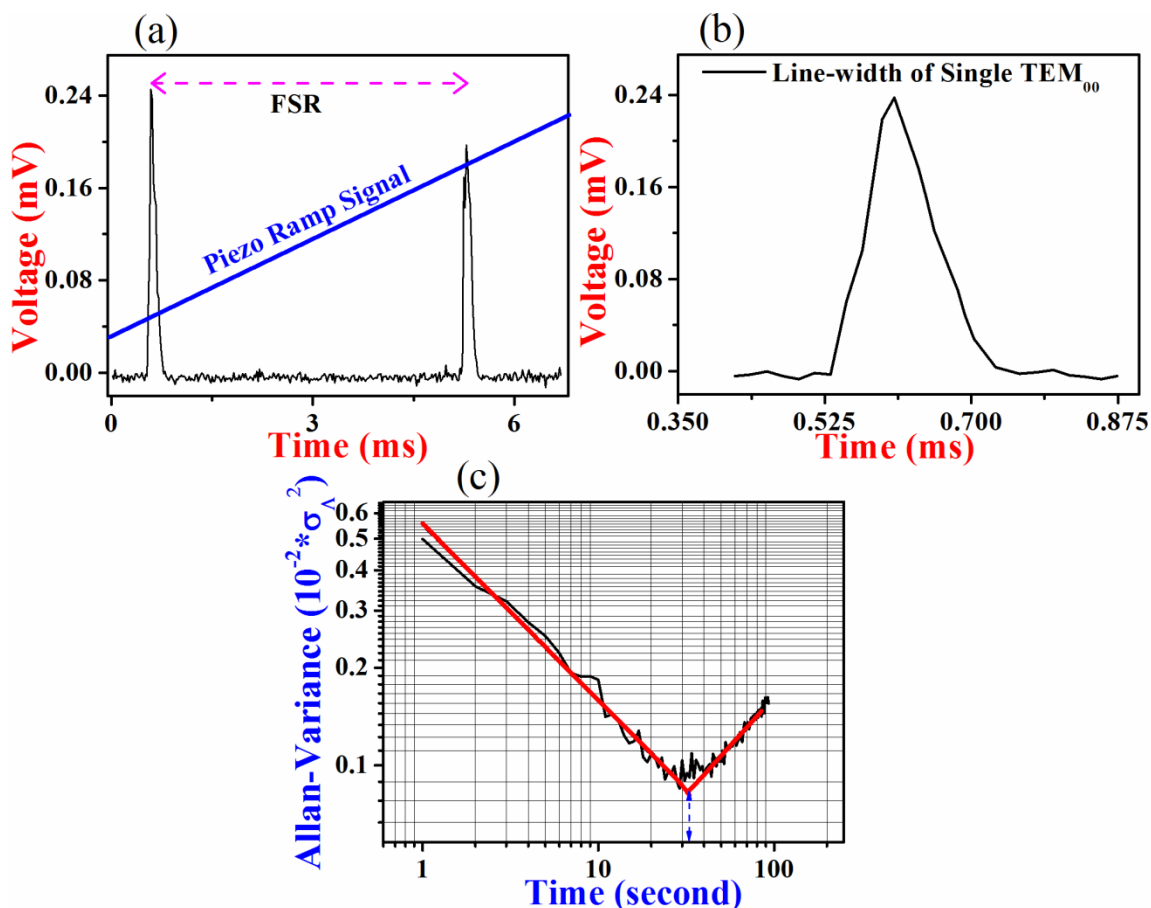


Figure 2.10(a) Laser-cavity resonances during cavity mirror oscillation over one free-spectral-range (FSR), (b) A zoom-in of single resonance, and (c) An Allan-variance plot of empty cavity ring-down time (τ_0).

We subsequently investigated the stability of the *cw* CRDS spectrometer by means of Allan variance analysis [28] to determine the optimum integration time to maximize the signal to noise ratio and thereby improving the limiting sensitivity of the current method. Figure 2.10c depicts a plot of the Allan-variance (σ_{λ}^2) of empty cavity ring-down times (τ_0) against the integration time (t) at a particular wavelength $\sim 7.5 \mu\text{m}$ with a data acquisition rate of 100 Hz. The log-log plot of the Allan-variance initially decreased linearly with the increase of integration time as the increase of data averaging reduces the noise level. We found an optimum integration time of 33 seconds which corresponds to 3300 ring-down decay signals for 100 Hz data acquisition rate and a noise-equivalent absorption coefficient (NEA) of $1.86 \times 10^{-9} \text{ cm}^{-1}\text{Hz}^{-1/2}$ was

achieved. However, after 33 sec there is no advantage of additional signal averaging since several instabilities arise in the system.

We next evaluated the performance of the *cw* CRDS sensor for sensitive, accurate quantitative measurements of ^{12}C and ^{13}C isotopes of CH_4 within 7.5-8 μm region by probing the interference-free molecular transitions of $^{12}\text{CH}_4$ and $^{13}\text{CH}_4$ isotopes arising from the fundamental bending (ν_4 band) vibrations of the bonds located at $\sim 1327.244\text{ cm}^{-1}$ and $\sim 1332.946\text{ cm}^{-1}$, respectively. Figure 2.11a and 2.11b shows the examples of the high-resolution *cw* CRDS spectra of CH_4 isotopes when certified

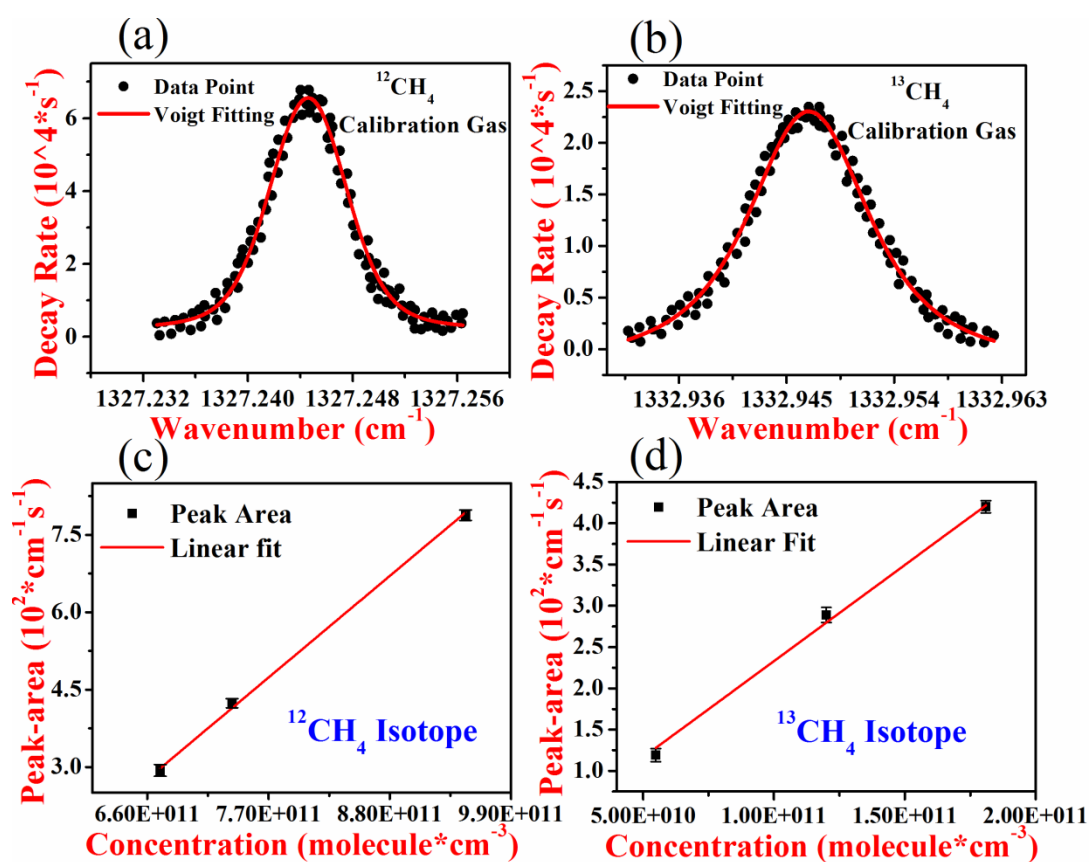


Figure 2.11(a), (b) CRDS spectra of calibration gases showing decay rate vs wavenumber plot of ^{12}C and ^{13}C isotopes of CH_4 centred at $\sim 1327.244\text{ cm}^{-1}$ and $\sim 1332.946\text{ cm}^{-1}$, respectively and fitted with Voigt function, (c), and (d) a linear regression plot between the area of CRDS spectra and molecular concentration of ^{12}C and ^{13}C isotopes of CH_4 , respectively.

calibration gas mixtures of $9.62 \pm 0.05\text{ ppm}$ of $^{12}\text{CH}_4$ and $438 \pm 2\text{ ppb}$ of $^{13}\text{CH}_4$ in N_2 (Air Liquid, Uk and CIL, USA) were injected into the optical

cavity with a pressure of 1 Torr and 15 Torr, respectively and spectral lines were fitted with the Voigt line-shape functions.

We then injected different concentrations of calibration standards of $^{12}\text{CH}_4$ and $^{13}\text{CH}_4$ isotopes into the optical cavity and acquired the wavenumber (cm^{-1}) dependent change of decay-rate (Δk in s^{-1}) across the selected molecular transitions. The integrated area under each absorption curve ($\text{cm}^{-1}\text{s}^{-1}$) was plotted against the different concentrations (i.e., no. of molecules cm^{-3}) and from the linear regression plot (Figure 2.11c and 2.11d), the line-integrated absorption cross-sections were determined to be $(\sigma_I)^{12}\text{CH}_4 = 5.82 \times 10^{-20} \text{ cm}^{-1} \text{ molecule}^{-1} \text{ cm}^2$ and $(\sigma_I)^{13}\text{CH}_4 = 7.8 \times 10^{-22} \text{ cm}^{-1} \text{ molecule}^{-1} \text{ cm}^2$ (normalized with isotopic abundances), respectively for the molecular transitions of ^{12}C and ^{13}C -isotopes of CH_4 at the selected molecular transitions, which were in excellent agreement with the values reported in HITRAN database [29].

We next studied the pressure broadening effect on the absorption spectra of ^{12}C and ^{13}C -isotopes of CH_4 at the designated wavenumbers, introducing zero-air in the optical cavity, and simultaneously assessed the parameters of sensitivity and selectivity of the CRDS sensor at the higher pressure because the pressure broadening has a direct effect on these parameters. Figure 2.12a and 2.12b illustrates the ring-down spectra for both the isotopes at different cavity-pressures retaining the same numbers of CH_4 molecules inside the cavity. A significant reduction of the peak height of isotopic CH_4 spectra was observed with increasing the pressure in the cavity. The spectra of such absorption lines were fitted with Voigt line-shape functions. Figure 2.12c and 2.12d shows the plots of the full-width half-maxima (FWHM in cm^{-1}) of the absorption lines of $^{12}\text{CH}_4$ and $^{13}\text{CH}_4$ isotopes against the different cavity-pressures (in Torr). The gradient of the linear regression of the plot provided the pressure-broadening coefficient of $0.067 \text{ cm}^{-1}\text{atm}^{-1}$ and $0.052 \text{ cm}^{-1}\text{atm}^{-1}$, respectively for ^{12}C and ^{13}C -isotopes of CH_4 which were in good agreement with the HITRAN values [29]. Moreover, we observed that sample pressure inside the ring-down cavity can be increased up to 100 Torr without any significant overlapping with the

adjacent foreign molecular transitions such as H₂O, CO₂ and N₂O and hence the sensitivity and specificity of the *cw* CRDS sensor for CH₄ detection remain unaltered at that pressure limit. We also calculated the minimum detection limit of the CRDS-based CH₄ sensor to be 396 pptv and 287 pptv, respectively for ¹²C and ¹³C-isotopes of CH₄ at 100 Torr cavity-pressure without any deleterious effects of pressure broadening.

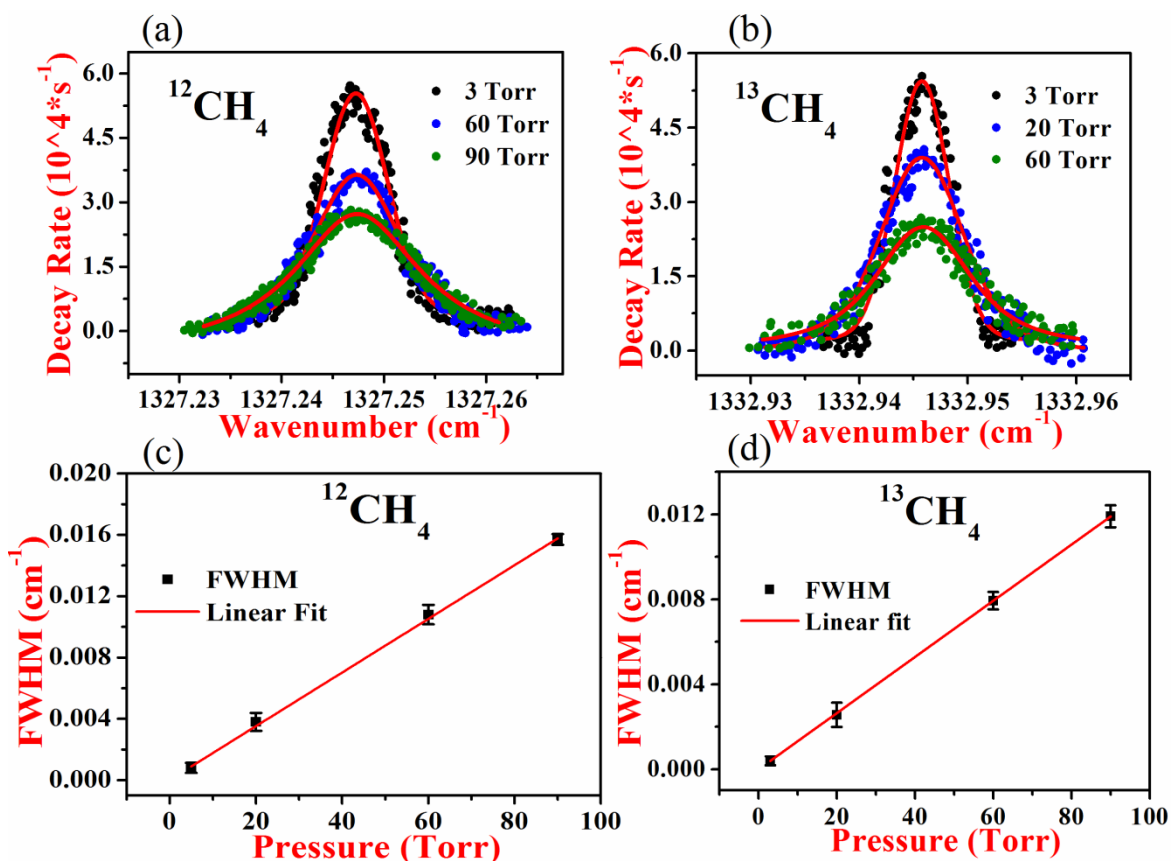


Figure 2.12(a), (b) Variation of absorption spectra of ¹²C and ¹³C isotopes of CH₄ respectively at different cavity pressures, (c), and (d) a linear regression plot between FWHM of absorption spectra and cavity pressures for ¹²C and ¹³C isotopes of CH₄ respectively.

We finally evaluated the potential of the EC-QCL based CH₄ sensor exploiting the *cw* CRDS technique for real-time monitoring of isotopic CH₄ concentrations in various environments for example, in ambient air and human exhaled breath samples. Figure 2.13a and 2.13b depicts the CRDS spectra of isotopic CH₄ in ambient air samples and the concentration levels of ¹²C and ¹³C-isotopic compositions of CH₄ were estimated to be 1200.4 ± 0.9 ppbv and 12.8±0.8 ppbv, respectively. We

subsequently utilized the sensor to quantify CH_4 isotopes in human exhaled breath. The CRDS spectra were depicted in Figure 2.13c and 2.13d and we observed that the typical concentration levels of ^{12}C and ^{13}C -isotopes of CH_4 in breath samples were 2340.7 ± 1 ppbv and 23.4 ± 0.7 ppbv, respectively. These observations suggest that the present EC-QCL based CH_4 sensor for quantitative detection of individual isotopes in the mid-IR spectral range has enormous potential to be applied in environmental sensing along with the non-invasive breath analysis for medical diagnostic purposes. It is noteworthy to mention that the

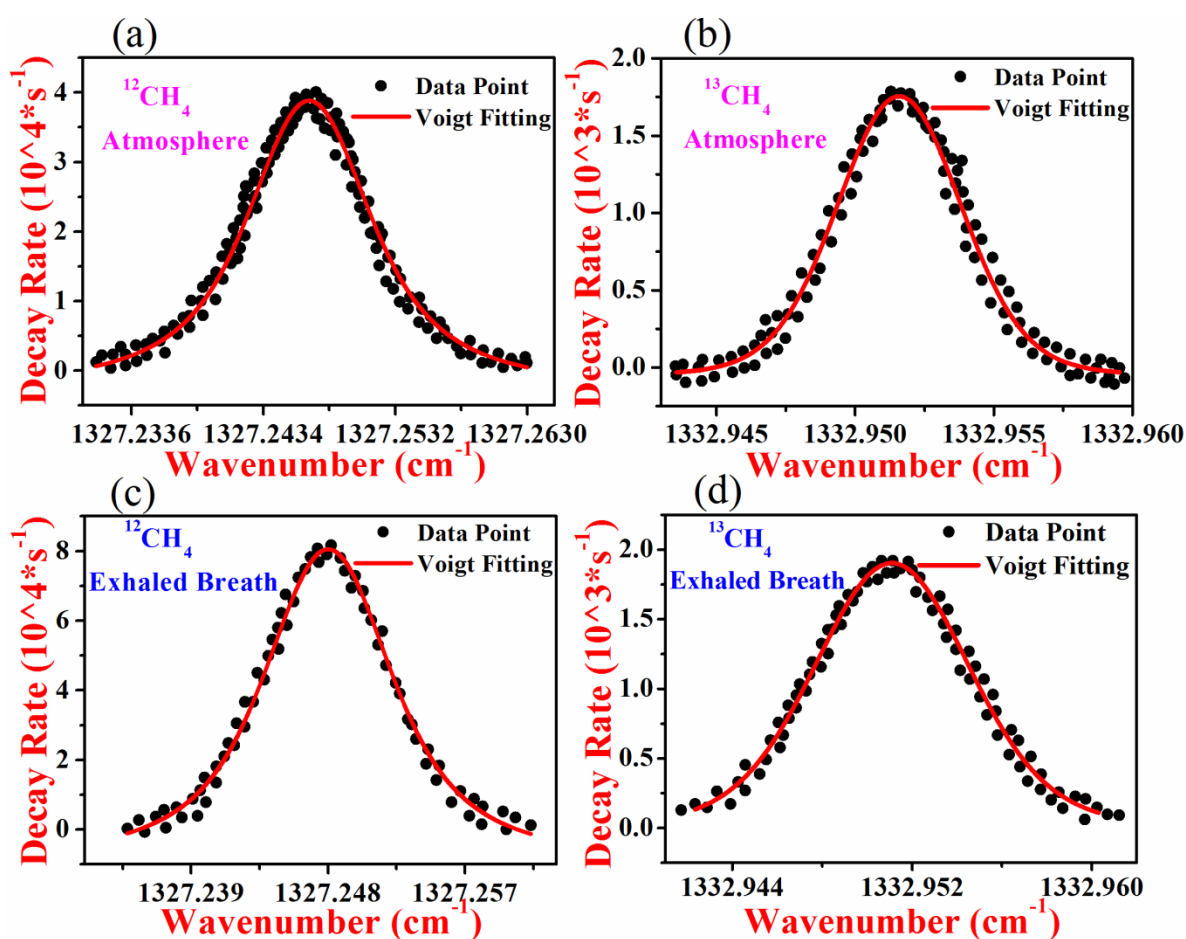


Figure 2.13 CRDS spectra of ^{12}C and ^{13}C isotopic concentrations of CH_4 in (a), (b) ambient air and (c), and (d) human exhaled breath.

detection limit of the present system for the measurement of the individual isotopes of CH_4 is comparable to the commercially available equipment (from Picarro and Los Gatos Research). However, the large uncertainty in the measurement of $^{13}\text{CH}_4$ isotope in our system in

comparison to the commercial equipment requires to be improved further for precise quantification of $^{13}\text{C}/^{12}\text{C}$ ratio.

2.6 Conclusions

We have developed and tested a high-resolution *cw* CRDS spectrometer coupled with a widely-tunable EC-QCL with MHF wavelength tuning capability working in the mid-IR spectral region of 7.5-8 μm for high-resolution molecular spectroscopy. We have validated the system for direct quantitative estimation of $^{12}\text{CH}_4$ and $^{13}\text{CH}_4$ isotopologues of methane (CH_4) without any sample pre-concentration unit. We have also demonstrated that the *cw* CRDS sensor has the sufficient capability to measure the different isotopes of CH_4 from various environments ranging from ambient air to human exhaled breath with ultra-high sensitivity in the levels of ppbv along with unprecedented molecular selectivity without overlapping any other trace molecular species. The high selectivity and sensitivity arise by probing the fundamental bending (ν_4 band) vibrations of the bonds of CH_4 that has well-defined central frequency. In addition, recording the high-resolution ring-down spectra at low pressures also eliminates the pressure broadening effects. Finally, the CRDS spectrometer can easily be adapted for monitoring several other isotopic species with mid-IR fundamental absorption bands such as H_2S , SO_2 , HNO_3 , C_2H_2 and H_2O_2 with anticipated detection limits in the pptv range. Therefore, the full potential of the EC-QCL-based *cw* CRDS method for in-depth high-resolution spectroscopic study to explore the whole range of 7.5-8 μm is yet to be explored, but the principles of the optical cavity based *cw* CRDS methodology are now well-established.

2.7 References

- [1] Mazurenka M, Orr-Ewing A J, Peverall R and Ritchie G A D 2005 Cavity ring-down and cavity enhanced spectroscopy using diode lasers *Annu. Rep. Prog. Chem. Sect. C* **101**, 100-42.
- [2] Scherer J J, Paul J B, O'Keefe A and Saykally R J 1997 Cavity Ring down Laser Absorption Spectroscopy: History, Development, and Application to Pulsed Molecular Beams *Chem. Rev.* **97**, 25-51.
- [3] O'Keefe A 1998 Integrated cavity output analysis of ultra-weak absorption *Chem. Phys. Lett.* **293**, 331-6.
- [4] Zalicki P and Zare R N 1995 Cavity ring-down spectroscopy for quantitative absorption measurements. *J. Chem. Phys.* **102**, 2708-17.
- [5] O'Keefe A and Deacon D A G 1988 Cavity ring-down optical spectrometer for absorption measurements using pulsed laser sources *Rev. Sci. Instrum.* **59**, 2544-51.
- [6] Greaves S J, Flynn E L, Fitcher E L, Wrede, Lydon D P, Low P J, Rutter S R and Beedy A 2006 Cavity Ring-Down Spectroscopy of the Torsional Motions of 1,4-Bis(phenylethynyl)benzene *J. Phys. Chem. A* **110**, 2114-21.
- [7] Hallock A J, Berman E S F and Zare R N 2003 Ultratrace Kinetic Measurements of the Reduction of Methylene Blue *J. Am. Chem. Soc.* **125**, 1158-9.
- [8] Dahnke H, Kleine D, Hering P and Murtz M 2001 Real-time monitoring of ethane in human breath using mid-infrared cavity leak-out spectroscopy *Appl. Phys. B* **72**, 971-5.
- [9] Atkinson D B 2003 Solving chemical problems of environmental importance using cavity ring-down spectroscopy *Analyst* **128**, 117-25.
- [10] Wada R and Orr-Ewing A J 2005 Continuous wave cavity ring-down spectroscopy measurement of NO₂ mixing ratios in ambient air *Analyst* **130**, 1595-1600.

- [11] Rennick C J, Engeln R, Smith J A, Orr-Ewing A J, Ashfold M N R and Mankelevich Y A 2005 Measurement and modeling of a diamond deposition reactor: Hydrogen atom and electron number densities in an Ar/H₂ arc jet discharge *J. Appl. Phys.* **97**, 113306.
- [12] van den Oever, van Helden J H, Lamers C C H, Engeln R, Schram D C, van de Sandan M C and Kessels 2005 Density and production of NH and NH₂ in an Ar-NH₃ expanding plasma jet *J. Appl. Phys.* **98**, 093301.
- [13] Schocker A, Kohse-Hoinghaus K and Brockhinke A 2005 Quantitative determination of combustion intermediates with cavity ring-down spectroscopy: systematic study in propene flames near the soot-formation limit *Appl. Optics* **44**, 6660-72.
- [14] Bechtel K L, Zare R N, Kachanov A A, Sanders S S and Paldus B A 2005 Moving beyond Traditional UV-Visible Absorption Detection: Cavity Ring-Down Spectroscopy for HPLC *Anal. Chem.* **77**, 1177-82.
- [15] Tong Z, Jakubinek M, Wright A, Gillies A and Loock H P 2003 Fiber-loop ring-down spectroscopy: A sensitive absorption technique for small liquid samples *Rev. Sci. Instrum.* **74**, 4818-26.
- [16] Engeln R, von Helden G, van Roji A J A and Meijer G 1999 Cavity ring down spectroscopy on solid C₆₀ *J. Chem. Phys.* **110**, 2732-3.
- [17] Pipino A C R, Hudgens J W and Huie R E 1997 Evanescent wave cavity ring-down spectroscopy with a total-internal-reflection minicavity *Rev. Sci. Instrum.* **68**, 2978-89.
- [18] Engeln R, Berden G, van den Berg E and Meijer G 1997 Polarization dependent cavity ring down spectroscopy *J. Chem. Phys.* **107**, 4458-67.
- [19] Wysocki G, Lewicki R, Curl R F, Tittel F K, Diehl L, Capasso F, Troccoli M, Hofler G, Bour D, Corzine S, Maulini R, Giovannini M and Faist J 2008 Widely tunable mode-hop free external cavity quantum cascade lasers for high resolution spectroscopy and chemical sensing *Appl. Phys. B* **92**, 305-11.

- [20] Curl R F, Capasso F, Gmachl C, Kosterev A A, McManus B, Lewicki R, Pusharsky M, Wysocki G and Tittel F K 2010 Quantum cascade lasers in chemical physics *Chemical Physics Letters* **487**, 1–18.
- [21] Hamilton D J and Orr-Ewing A J 2011 A quantum cascade laser-based optical feedback cavity-enhanced absorption spectrometer for the simultaneous measurement of CH₄ and N₂O in air *Appl. Phys. B* **102**, 879–90.
- [22] von Koch B *Atmospheric traces monitoring using cavity ring-down spectroscopy*, PhD Thesis, Technischen Universität zur, Germany, 2003.
- [23] van Zee R D, Hodges J T and Looney J P 1999 Pulsed, single-mode cavity ringdown spectroscopy *Appl. Optics*. **38**, 3951–60.
- [24] Siegman A E, *Lasers*, Oxford University Press, 1986.
- [25] Saleh B E A and Teich M C, *Fundamentals of Photonics*, John Willey & Sons, 1991.
- [26] Lindley R E, *Development of diode laser-based optical sensors for quantitative trace gas analysis*, PhD Thesis, University of Bristol, UK, 2007.
- [27] Li J S, Chen W and Fischer H 2013 Quantum Cascade Laser Spectrometry Techniques: A New Trend in Atmospheric Chemistry *Applied Spectroscopy Reviews*, **48**, 523–59.
- [28] Werle P, Mucke R and Slemr F 1993 The limits of signal averaging in atmospheric trace-gas monitoring by tunable diode-laser absorption spectroscopy (TDLAS) *Appl. Phys. B* **57**, 131–9.
- [29] Rothman L, Gordon I, Babikov Y, Barbe A, Chris Benner D, Bernath P, Birk M, Bizzocchi L, Boudon V, Browni L R, Campargue A, Chance K, Cohen E A, Coudert L H, Devi V M, Drouin B J, Fayt A, Flaud J M, Gamachem R R, Harrison J J, Hartmann J M, Hill C, Hodges J T, Jacquemart D, Jolly A, Lamouroux J, LeRoy R J, Li G, Long D A, Lyulin O M, Mackie C J, Massie S T, Mikhailenko S, Müller H S P, Naumenko O V, Nikitin A V, Orphal J, Perevalov V, Perrin A, Polovtseva E R, Richard C, Smith M A H, Starikova E, Sung K, Tashkun S, Tennyson J, Toon G C,

Tyuterev VI G and Wagner G 2013 The HITRAN 2012 molecular spectroscopic database *J Quant Spectrosc Radiat Transf* **130**, 4–50.

Chapter 3

Calibration-free ($2f/1f$) Wavelength Modulation Spectroscopy using an external- cavity quantum cascade laser for trace detection of acetylene

3.1 Introduction

Tunable diode laser absorption spectroscopy (TDLAS) is a very sensitive direct absorption technique to measure absorption-based gas parameters [1-5]. However, in conventional direct absorption spectroscopic technique a small change in light intensity is measured against a large background signal. Thus, the measurement sensitivity and precision of the TDLAS are often limited due to the inherent intensity fluctuations of diode laser which is called as low frequency noise or $1/f$ noise. Wavelength modulation spectroscopy (WMS) is incorporated to the TDLAS to reduce the excessive laser $1/f$ noise [6,7].

In WMS, laser wavelength is modulated at a high frequency (kHz to several MHz range), less than the optical frequency of the half-width of the probed absorption line. The rapidly modulating wavelength interacts with the non-uniform absorption feature and gives rise to the

harmonics components at the detector signal which are eventually recovered using a phase sensitive lock-in-amplifier. The amplitude of second harmonic ($2f$) signal is commonly utilized to infer sample concentration as the $2f$ signal strongly depends on both spectral parameters and sample properties and hence can easily be compared with spectral simulations. Moreover, $2f$ signal is sensitive to the curvature of the spectral line rather than absolute absorption intensity [8,9]. In contrast, first harmonic ($1f$) signal mostly contains the information of intensity fluctuation associated with the wavelength modulation [10-12]. The use of a lock-in-amplifier with a narrow band-pass filter significantly reduces the laser intensity noise and electronic noise. Therefore, WMS enhances the signal-to-noise ratio about two orders of magnitude over the direct absorption spectroscopy.

However, the conventional WMS suffers from a major drawback to be applied in the real world applications. The WMS- $2f$ signal amplitude is proportional not only to the concentration but also to the light power, the electronic gain, and the detection phase. Therefore, it is required to be calibrated with a known sample concentration at the experimental conditions to obtain the absolute concentration of an unknown sample. This makes the traditional WMS imperfect for the field-deployable sensors. Hence, several 'Calibration-free' methods have been proposed in the literatures [13-17]. Each method has its pros and cons and is found to be suitable at certain conditions. However, the method proposed by Li [18] is found to be the most appropriate to be applied in the real-world applications.

In this chapter, the 'Calibration-free' method suggested by Li is demonstrated for trace sensing of C_2H_2 using a cw EC-QCL operating between 7.5-8 μm . In this method, the WMS- $2f$ signal is first normalized for laser intensity by $1f$ signal. The WMS- $2f/1f$ signal is then fitted with a model which includes the characteristic parameters of the probed laser and spectral information of the probed absorption line. As the model incorporates the experimental parameters, it can be directly compared with the acquired WMS- $2f/1f$ signal to infer sample concentration.

3.2 Calibration-free WMS-2f/1f Model

The basic principle of self-calibration by 1f-normalized 2f (2f/1f) signal in wavelength modulation spectroscopy (WMS) has been described in details elsewhere [18-20]. Here, we have briefly described the theory of WMS-2f/1f method. The fundamental concept of absorption spectroscopy, in absence of optical saturation, is based on well-known Beer-Lambert's law expressed as

$$\begin{aligned} I(\nu) &= I_0(\nu) \exp[-\alpha(\nu)L] \\ &= I_0(\nu) \exp[-S_i(T)Px\phi_i(\nu)L] \end{aligned} \quad (3.1)$$

where, $I_0(\nu)$ is the incident laser intensity, $I(\nu)$ is the transmitted laser intensity, ν is the emission frequency, $\alpha(\nu)$ is the absorption coefficient, $S_i(T)$ is the absorption line strength of i^{th} transition at temperature T , P is the total pressure, x is the mole fraction of the target species, $\phi_i(\nu)$ is the transition line shape and L is the absorption optical path length.

WMS is generally performed by modulating the laser injection current with a frequency f_m , thereby simultaneously producing frequency modulation (FM) and linear and non-linear intensity modulation (IM) with modulation frequency dependent phase difference. Then the instantaneous frequency (ν) and incident intensity (I) of laser can be expressed as

$$\nu(t) = \nu_{ave} + \Delta\nu \cos 2\pi f_m t \quad (3.2)$$

$$I(t) = I_{ave}(\nu) [1 + \Delta I_1 \cos(2\pi f_m t + \psi_1) + \Delta I_2 \cos(4\pi f_m t + \psi_2)] \quad (3.3)$$

where $I(t)$ is the slowly varying laser intensity, ΔI_1 and ΔI_2 are the linear and non-linear IM amplitudes normalized by average laser intensity at ν , $\Delta\nu$ is the FM amplitude, ψ_1 and ψ_2 represent the phase differences of FM with the linear and non-linear IM, respectively.

As the laser frequency is modulated sinusoidally according to Equation 3.2, the transmitted laser intensity in Equation 3.1 also becomes a

periodic function of $2\pi f_m t$ and thus can be expanded in a Fourier series. Therefore, spectral absorbance can be expressed as

$$\alpha(\nu_{ave} + \Delta\nu \text{Cos} 2\pi f_m t) = \sum_{n=0}^{n=\infty} H_n(\nu_{ave} + \Delta\nu) \text{Cos}(2n\pi f_m t) \quad (3.4)$$

where $H_n(\nu_{ave} + \Delta\nu)$ is the n^{th} Fourier coefficient. For WMS-2f/1f method, a lock-in-amplifier (LIA) is employed to measure the second harmonics (2f) and first harmonics (1f) of the detector signal (I(t)). The X and Y components of 2f and 1f signals are recovered by multiplying detector signal (I(t)) by sinusoidal and cosinusoidal reference signals, respectively and are expressed as

$$X_{2f} = \frac{GI_{ave}(\nu)}{2} [H_2 + \frac{\Delta I_1}{2}(H_1 + H_3)\text{Cos} \psi_1 + \Delta I_2(H_0 + \frac{H_4}{2})\text{Cos} \psi_2] \quad (3.5)$$

$$Y_{2f} = -\frac{GI_{ave}(\nu)}{2} [\frac{\Delta I_1}{2}(H_1 - H_3)\text{Sin} \psi_1 + \Delta I_2(H_0 - \frac{H_4}{2})\text{Sin} \psi_2] \quad (3.6)$$

$$X_{1f} = \frac{GI_{ave}(\nu)}{2} [H_1 + \Delta I_1(H_0 + \frac{H_2}{2})\text{Cos} \psi_1 + \frac{\Delta I_2}{2}(H_1 + H_3)\text{Cos} \psi_2] \quad (3.7)$$

$$Y_{1f} = -\frac{GI_{ave}(\nu)}{2} [\Delta I_1(H_0 - \frac{H_2}{2})\text{Sin} \psi_1 + \frac{\Delta I_2}{2}(H_1 - H_3)\text{Sin} \psi_2] \quad (3.8)$$

where G is the optical-electrical gain of the detection system and also accounts for all transmission losses other than molecular absorption. Now, 1f normalized 2f signal being independent of instrumental factors provides calibration free response and thus can be utilized to assess the sample concentration with pre-characterization of laser parameters (ΔI_1 , ΔI_2 , $\Delta\nu$, ψ_1 and ψ_2). In this method, 1f normalized 2f used for concentration assessment is expressed as

$$R_{2f} / R_{1f} = \sqrt{X_{2f}^2 + Y_{2f}^2} / \sqrt{X_{1f}^2 + Y_{1f}^2} \quad (3.9)$$

where X_{2f} , Y_{2f} , X_{1f} and Y_{1f} are given by Equations 3.5-3.8. This technique is based on the consideration that R_{1f} is non-zero. To retrieve the sample concentration from the calibration-free WMS-2f/1f signal, either the central peak value or the line shape of R_{2f}/R_{1f} can be utilized [18,21].

3.3 Experimental Setup

The detailed experimental setup is schematically shown in Figure 3.1. A room temperature continuous wave external cavity quantum cascade laser (*cw* EC-QCL; Daylight Solutions MHF-41078) with mode-hop-free (MHF) tuning range of 1257-1341 cm^{-1} was employed as an optical source to probe the absorption features of C_2H_2 . The extremely narrow linewidth along with MHF frequency tuning capability ($<0.0003 \text{ cm}^{-1}$) and high power ($<100 \text{ mW}$) of the *cw* EC-QCL light source made the WMS-2f/1f strategy for high-resolution spectroscopic detection of C_2H_2 . The highly collimated laser light was initially passed through an optical

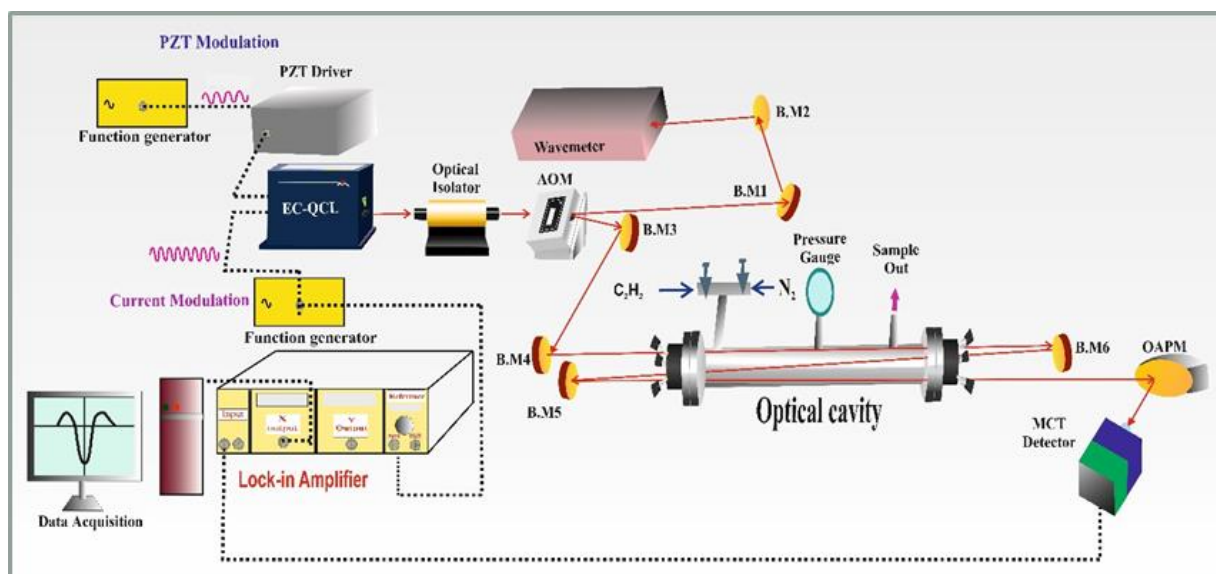


Figure 3.1 A schematic of experimental setup for wavelength modulation spectroscopy (WMS).

isolator (FIO-5-7.8; Innovation Photonics) to prevent the reflected light feeding back to the laser. An acousto-optic modulator (AOM; AGM406B11M; IntraAction Corp.) was thereafter utilized as a beam splitter to diffract the laser beam into zeroth order and first order

components. The first-order deflected beam from the AOM was then passed into the optical cavity and the zeroth-order beam was directed into a wavemeter (621B-MIR; Bristol Instruments) for real-time monitoring of wavenumber. The optical cavity comprised of two ZnSe mid-IR windows positioned about 50 cm apart from each other. Two flat, gold coated reflector mirrors (BM5 and BM6) outside the cavity were aligned to reflect the beam back and forth 3 times through the cell, thereby making a homemade multi-pass cell arrangement that increased the path length to ~ 1.5 m. The laser light exiting from the cavity was focused onto a mid-IR thermoelectrically cooled photovoltaic mercury-cadmium-telluride (MCT) detector (PVI-4TE-8-1X1; Vigo System S.A.) by a gold-coated off-axis parabolic mirror (OAPM). To achieve wavelength modulation, the EC-QCL was slowly and sinusoidally ($V_{\text{scan}} = 25\text{V}$ and $f_{\text{scan}} = 2.5\text{ Hz}$) scanned over the absorption line of C_2H_2 by a piezo-electric driver (MDT693B; ThorLabs) along with a 30 kHz (f_m) sine wave modulation of injection current of the EC-QCL. The detector signal was then fed into a lock-in amplifier (Stanford Research Systems SR830 DSP) to demodulate the signal at the harmonics of the modulating frequency. The lock-in amplifier time constant was set to 3 ms to achieve maximum signal-to-noise ratio. The demodulated signal from the lock-in amplifier was finally acquired using a high-speed (100MS/s) data-acquisition card (Model PCI-5221 National Instruments 14-bit, 100 MHz bandwidth) and analysed by a custom-written LabVIEW program.

3.4 Results and Discussions

3.4.1 Absorption Spectroscopy of C_2H_2

The *cw* EC-QCL was scanned over its entire mode-hop-free spectral region of 1257 cm^{-1} - 1341 cm^{-1} to assess the full P-branch of ($\nu_4 + \nu_5$) combination band of C_2H_2 . The experimental determination of the spectrum of direct absorption of 1034 ppm C_2H_2 at 150 Torr pressure and 296K temperature is depicted in Figure 3.2a. Subsequently, it was compared with the simulated spectrum from the HITRAN database [22]

(Figure 3.2b) based on the experimental parameters. Few transition lines of C_2H_2 with low absorption cross-section were indistinguishable in the

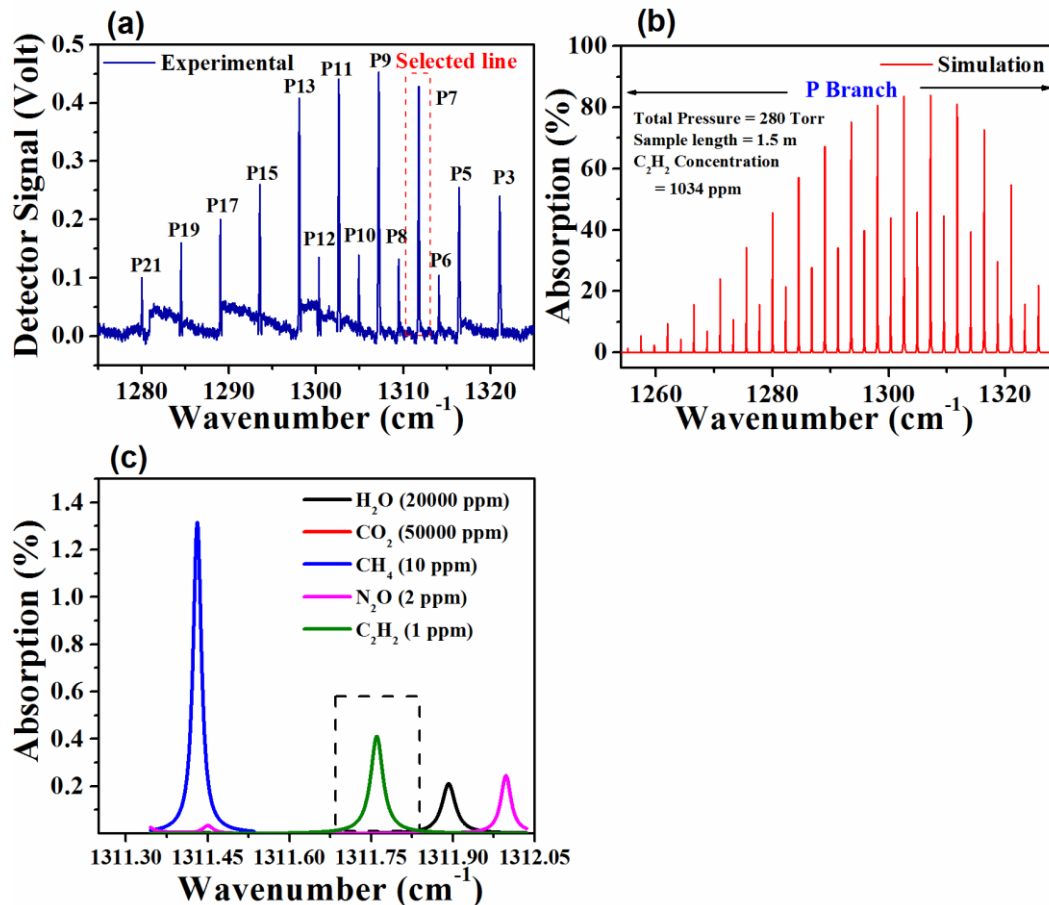


Figure 3.2(a) Experimental direct-absorption spectra of P-branch of $\nu_4 + \nu_5$ combination band of C_2H_2 within the spectral region of 1257 cm^{-1} - 1330 cm^{-1} at 1034 ppm concentration, 280 Torr pressure and sample length of 1.5 metre . **(b)** HITRAN simulation under the same experimental conditions. **(c)** HITRAN simulated spectra of different gases around P7 transition line of C_2H_2 at 1311.7600 cm^{-1} .

experimental spectrum due to poor signal-to-noise ratio at the mentioned experimental conditions. We further performed a simulation under the experimental conditions (Sample length = 1.5 m , Pressure = 150 Torr , Temperature = 296K) to select an interference-free transition line of C_2H_2 . Figure 3.2c illustrates the simulated spectra of low concentration of C_2H_2 (1 ppm) in combination with the several abundant

molecular species (such as H₂O, CO₂, CH₄, N₂O) which are present in industrial field as well as in human exhaled breath. We selected the P7 rotational line of C₂H₂ centred at 1131.7600 cm⁻¹, one of the strongest absorption lines of the P-branch with the linestrength of 1.179 × 10⁻¹⁹cm⁻¹molecule⁻¹cm², for the present study.

3.4.2 Laser Characterization

We next performed the characterization of the laser parameters (ΔI_1 , ΔI_2 , ψ_1 , ψ_2) for the WMS-2f/1f detection method by modulating (30 kHz) sinusoidally the injection-current of the EC-QCL operating at 1311.7600 cm⁻¹. We determined the laser parameters as a function of modulation depth ($\Delta\nu$) which is the half of peak-to-peak of FM. A home-made etalon with free spectral range (FSR) of 0.01 cm⁻¹ was utilized to track the FM,

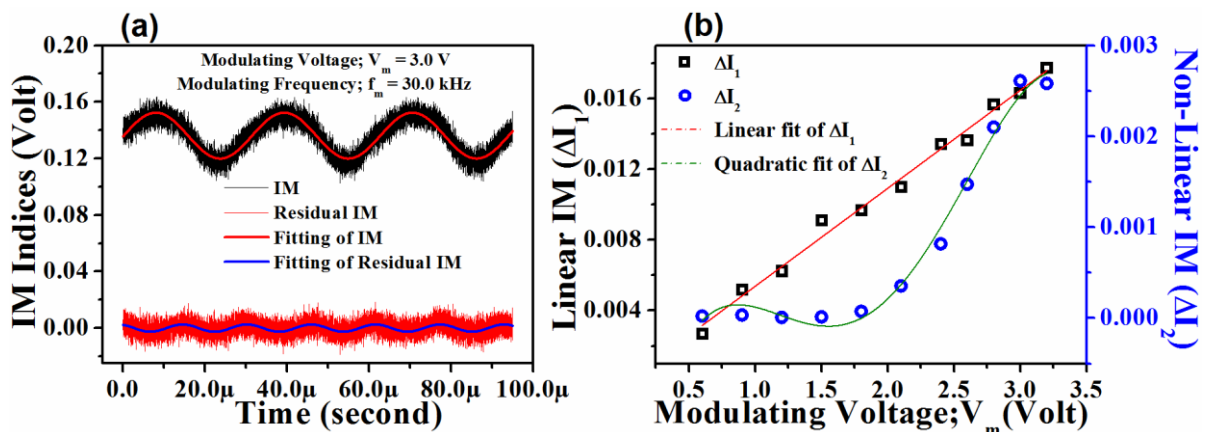


Figure 3.3(a) Intensity curve and residual for modulating voltage (V_m) of 3.0 volt and modulating frequency (f_m) of 30 kHz with best $1f_m$ and $2f_m$ fits, respectively. **(b)** Measured linear and non-linear components of IM at different modulating voltages with best linear and quadratic fits, respectively.

whereas linear and non-linear IM were measured in absence of the sample. We calculated the modulation depth ($\Delta\nu$) by sinusoidally fitting the fringe centre in the interference pattern of FM. The linear IM (ΔI_1) was determined by fitting the laser intensity with a sinusoidal function (Figure 3.3a). Thereafter, the linear FM/IM phase shift (ψ_1) was found to be 1.21π from the modulation of intensity and frequency. The fitting residual of linear IM (ΔI_1) was further fitted by a sinusoidal function

twice the modulation frequency to acquire the non-linear IM (ΔI_2). The non-linear IM (ΔI_2) is commonly known as residual amplitude modulation (RAM) which is the background of the $2f$ signal. Now, the phase shift of the non-linear IM (ψ_2) was determined from the fitting of the laser intensity and prior-knowledge of ψ_1 . We also found a linear and quadratic dependence, as shown in Figure 3.3b, for ΔI_1 and ΔI_2 , respectively as a function of modulation voltage (V_m). The *cw* EC-QCL employed in the present study thus can be characterized by modulating voltage (V_m) of 3.0 volt and modulating frequency (f_m) of 30 kHz as

$$I(t) = I_{ave}(\nu)[1 + 0.0163 * \text{Cos}(2\pi f_m t + 1.21\pi) + 0.0026 * \text{Cos}(4\pi f_m t + 1.29\pi)] \quad (3.10)$$

3.4.3 Optimization of Modulation depth

The maximum WMS- $2f$ signal can be achieved at the optimum modulation index m , which is defined as

$$m = \Delta\nu / (\gamma / 2) \quad (3.11)$$

where $\Delta\nu$ is the modulation depth and γ is the full-width at half maximum (FWHM) of the absorption line shape at the atmospheric pressure. It is well documented that the maximized WMS- $2f$ signal is obtained at $m = 2.2$. The pressure broadening coefficient of the selected P7 transition line of C_2H_2 at $1311.7600 \text{ cm}^{-1}$ is $0.0852 \text{ cm}^{-1}\text{atm}^{-1}$ which requires an optimum value of $\Delta\nu$ around 0.187 cm^{-1} (5.6 GHz) for the maximum WMS- $2f$ signal. However, due to the limitations on the current modulation, a maximum modulation depth of 2.5 GHz (0.0833 cm^{-1}) can be achieved for the current *cw* EC-QCL. Therefore, experimental parameters are required to be optimized to maximize the WMS- $2f$ signal for the present study. We first measured the amplitude of WMS- $2f$ signal as a function of the modulating amplitude (V_m) and found that the signal-to-noise ratio initially increases with the increase of the modulating amplitude and then followed by an increase in the line-width which eventually leads to a decrease in signal (Figure 3.4a). The amplitude of WMS- $2f$ signal was then plotted as a function of

modulating amplitude (V_m) in Figure 3.4b and a maximum WMS-2f signal was achieved at modulation amplitude of 2.5 Volt.

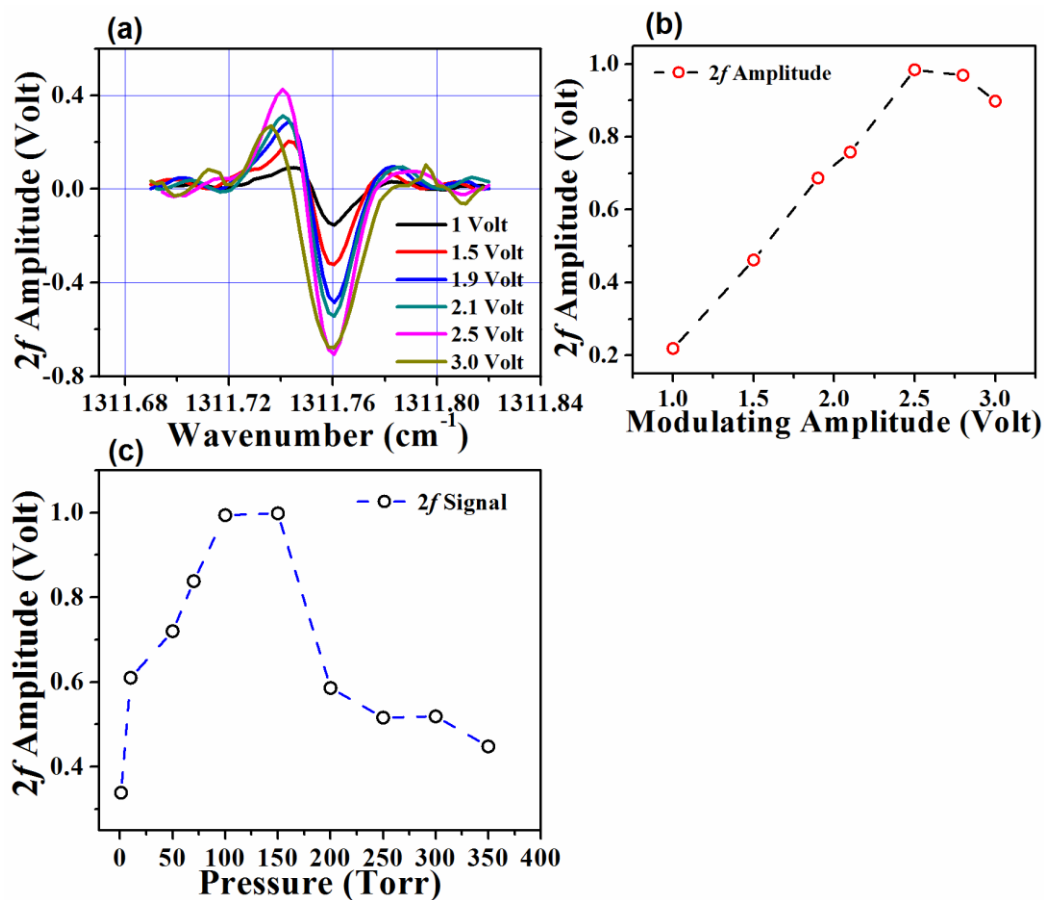


Figure 3.4(a) 2f WMS spectra of C₂H₂ for P7 rotational line of (ν₄+ν₅) combination band at 1311.7600 cm⁻¹ and 150 Torr pressure as a function of modulating voltage. **(b)** The amplitude of 2f WMS signal as a function of modulating voltages. **(c)** Amplitude variation of 2f WMS signal for different sample pressures at modulating voltage of 2.5 volt and sample concentration of 1034 ppm.

We next performed a series of experiments with a constant sample concentration at the optimum modulation amplitude (V_m) of 2.5 Volt with the aim to achieve an optimum value of sample pressure (Figure 3.4c). We found that the amplitude of WMS-2f signal was maximum at the pressure of 150 Torr for the optimum modulating voltage (V_m) of 2.5 Volt. The modulation depth ($\Delta\nu$) was found to be 0.037 cm⁻¹ at 2.5 Volt of the modulation amplitude (V_m) and frequency of 30 kHz. Therefore, the modulation index (m) for the experimentally achieved optimum

modulation depth (0.037 cm^{-1}) and pressure (150 Torr) was determined to be ~ 2.2 ($0.037 \text{ cm}^{-1} / 0.0168 \text{ cm}^{-1}$), which confirmed the theoretical prediction of the m index. The experimental WMS- $1f$ and $2f$ signals of the P7 transition line of C_2H_2 at $1311.7600 \text{ cm}^{-1}$ are depicted in Figure 3.5 for the optimum pressure and modulation depth. The WMS- $2f$ signal was found to be asymmetric and this asymmetry arises from the linear IM component. In contrast, the non-linear IM component contributes to the WMS- $2f$ residual amplitude modulation ($2f$ -RAM) which is responsible for the non-zero DC-offset of the WMS- $2f$ signal.

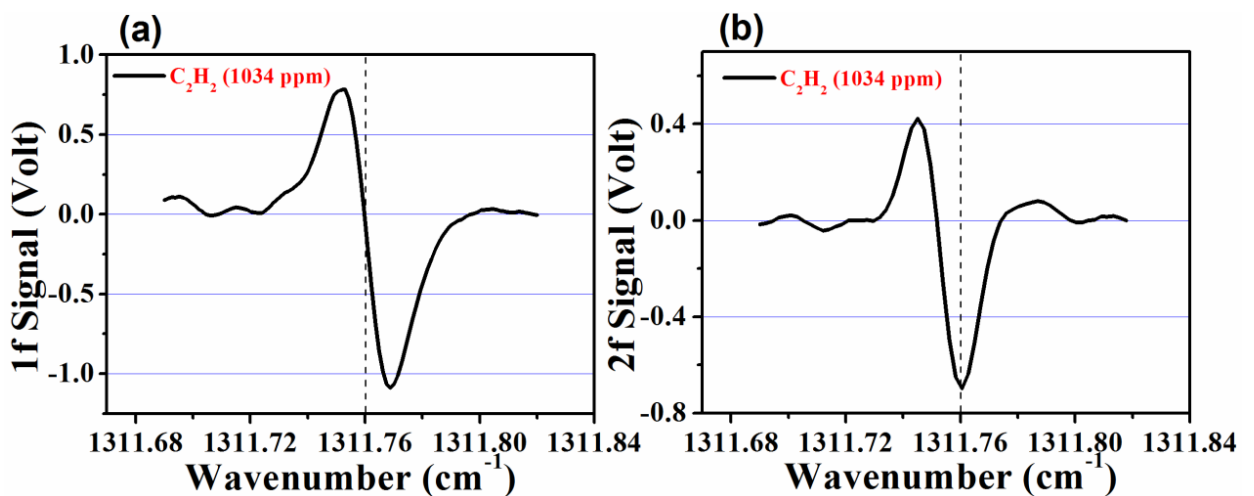


Figure 3.5(a) 1f and (b) 2f WMS spectra of selected C_2H_2 absorption line at $1311.7600 \text{ cm}^{-1}$ for optimum modulating voltage and pressure of 2.5 volt and 150 Torr, respectively.

3.4.4 Calibration-free normalized WMS- $2f/1f$ signal

The WMS- $2f/1f$ line shape, for the P7 transition line of C_2H_2 centred at $1311.7600 \text{ cm}^{-1}$, in a single laser scan at different sample concentrations and pressure of 150 Torr is shown in Figure 3.6. The measurements were performed with the modulation parameters of $V_{\text{scan}} = 25 \text{ V}$, $f_{\text{scan}} = 2.5 \text{ Hz}$, $V_m = 2.5 \text{ V}$ and $f_m = 30 \text{ kHz}$ and compared with the simulated results. The simulation result fits well with the centre peak of WMS- $2f/1f$ at the transition centre of $1311.7600 \text{ cm}^{-1}$. However, it was found that the fittings of the side peaks of WMS- $2f/1f$ with the simulated result were more susceptible than the centre peak due to the uncertainties in the IM

phase shifts, arising from the fact that the odd harmonics of the isolated transition are only zero at line-centre position. The centre-peak value of WMS- $2f/1f$ was utilized to infer the gas concentration.

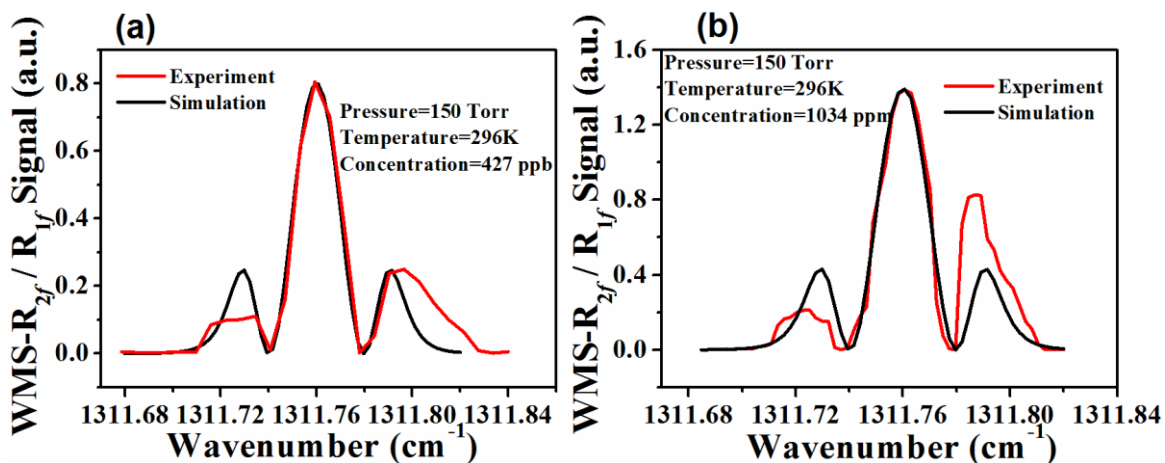


Figure 3.6(a) and (b) $1f$ normalized $2f$ WMS (WMS- $2f/1f$) spectra fitted with simulated result for the selected C_2H_2 absorption line at $1311.7600 \text{ cm}^{-1}$ for different sample concentrations under the optimum experimental conditions.

3.4.5 Measurement Linearity and System Stability

We next tested the linearity of the WMS- $2f/1f$ detection system for the measurement of C_2H_2 concentration ranging from 0.4 ppm to 1000 ppm (Figure 3.7a). A linear regression demonstrated a good linear correlation ($R^2 = 0.9983$) between WMS- $2f/1f$ signal amplitude and the concentration of C_2H_2 .

Finally, we performed Allan variance test to evaluate the long-term stability of the present detection system (Figure 3.7b) [23]. A standard C_2H_2 concentration of 0.4 ppm was measured up to 30 minutes. We achieved the minimum detection limit of 43 ppb with an averaging time of 1 second. However, an optimum averaging time for the system was found to be 110 seconds which corresponds to the minimum detection limit of 3 ppb . This suggests the potential of $1f$ normalized WMS- $2f$ strategy using an EC-QCL for ultra-sensitive detection of C_2H_2 in real-life practical applications.

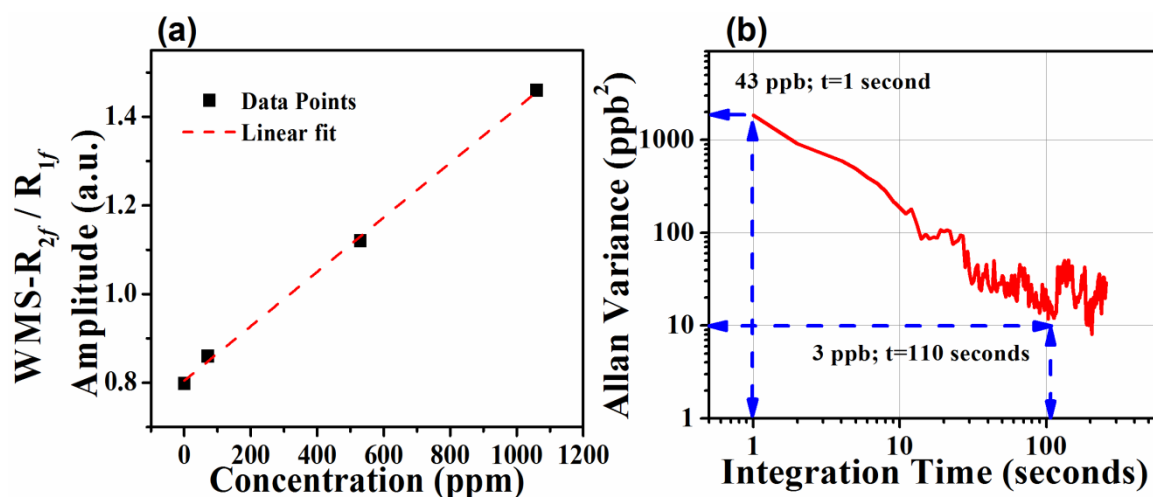


Figure 3.7(a) A linear regression plot between WMS-2f/1f amplitude and standard C₂H₂ concentrations. (b) The Allan Variance plot for the system stability.

3.5 Conclusions

We developed, implemented and also tested a calibration-free WMS-2f/1f detection method using the *cw* EC-QCL in the mid-IR spectral region covering 7.5-8 μm . The validity of the system was demonstrated by ultra-sensitive detection of C₂H₂ in the levels of ppb via a rotationally resolved P7 line in the ($\nu_4+\nu_5$) combination band of C₂H₂ at 1311.7600 cm^{-1} . The performance of the system was evaluated by characterizing the different laser parameters associated with the current-modulation and subsequently the stability was verified by the Allan-variance analysis. A noise-limited detection limit of 3 ppb for C₂H₂ detection was achieved over the 1.5 m optical pathlength for 110 seconds averaging, but this could further be improved by coupling the WMS-2f/1f technique to a multi-pass cell, such as Herriot cell or White cell, and a detection limit in the order of ppt (10^{-12}) can easily be achieved. Moreover, the advantages of wide tunability and high-resolution of EC-QCL system coupled with the present calibration-free WMS-2f/1f strategy could further be extended to study other molecular species within the tuning range of the laser.

3.6 References

- [1] Hinkley E D and Kelley P L 1971 Detection of Air Pollutants with Tunable Diode Lasers *Science* **19**, 635-9.
- [2] Martin P A 2002 Near-infrared diode laser spectroscopy in chemical process and environmental air monitoring *Chem. Soc. Rev.* **31**, 201-10.
- [3] Werle P 1998 A review of recent advances in semiconductor laser based gas monitors *Spectrochim. Acta Part A* **54**, 197-236.
- [4] Lackner M 2007 Tunable diode laser spectroscopy (TDLAS) in the process industries - a review *Rev. Chem. Eng.* **23**, 65.
- [5] Allen M G 1998 Diode laser absorption sensors for gas-dynamic and combustion flows *Meas. Sci. Technol.* **9**, 545-62.
- [6] Song K and Jung E C 2003 Recent Developments in Modulation Spectroscopy for Trace Gas Detection Using Tunable Diode Lasers. *Applied Spectroscopy Reviews* **38(4)**, 395-432.
- [7] Hancock G, van Helden J H, Peverall R, Ritchie G A D and Walker R J 2009 Direct and wavelength modulation spectroscopy using a cw external cavity quantum cascade laser. *Appl. Phys. Lett.* **94**, 201110.
- [8] Liu J T C, Jeffries J B and Hanson R K 2004 Large-modulation-depth $2f$ spectroscopy with diode lasers for rapid temperature and species measurements in gases with blended and broadened spectra *Appl. Opt.* **43**, 6500-9.
- [9] Dharamsi A N and Bullock A M 1996 Applications of wavelength-modulation spectroscopy in resolution of pressure and modulation broadened spectra *Appl. Phys. B* **63**, 283-92.
- [10] Cassidy D T and Reid J 1982 Atmospheric pressure monitoring of trace gases using tunable diode lasers *Appl. Opt.* **21**, 1185-90.
- [11] Uehara K and Tai H 1992 Remote detection of methane with a 1.66- μ m diode laser *Appl. Opt.* **31**, 809-14.

- [12] Iseki T, Tai H and Kimura K 2000 A portable remote methane sensor using a tunable diode laser *Meas. Sci. Technol.* **11**, 594-602.
- [13] Henningsen J and Simonsen H 2000 Quantitative wavelength-modulation without certified gas mixtures *Appl. Phys. B* **70**, 627-33.
- [14] Duffin k, McGettrick A J, Johnstone W, Stewart G and Moodie D G 2007 Tunable diode laser spectroscopy with wavelength modulation: A calibration free approach to the recovery of absolute gas absorption line-shapes *J. Lightw. Technol.* **25**, 3114-25.
- [15] McGettrick A J, Duffin K, Johnstone W, Stewart G and Moodie D G 2008 Tunable diode laser spectroscopy with wavelength modulation: A phasor decomposition method for calibration-free measurements of gas concentration and pressure *J. Lightw. Technol.* **26**, 432-40.
- [16] Chen J, Hangauer A, Strzoda R and Amann M C 2011 VCSEL-based calibration-free carbon monoxide sensor at 2.3 μm with in-line reference cell *Appl. Phys. B* **102**(2), 381-9.
- [17] Bain J R P, Johnstone W, Ruxton K, Stewart G, Lengden M and Duffin K 2011 Recovery of absolute gas absorption line shapes using tunable diode laser spectroscopy with wavelength modulation-Part 2: experimental investigation *J. Lightwave Technol.* **29**(7), 987-96.
- [18] Li H, Rieker G B, Liu X, Jeffries J B and Hanson R K 2006 Extension of wavelength modulation spectroscopy to large modulation depth for diode laser absorption measurements in high-pressure gases *Applied Optics* **45**(5), 1052-61.
- [19] Chao X, Jeffries J B and Hanson R K 2009 Absorption sensor for CO in combustion gases using 2.3 μm tunable diode lasers *Meas. Sci. Technol.* **20**, 115201.
- [20] Chao X, Jeffries J B and Hanson R K 2012 Wavelength-modulation-spectroscopy for real-time, in situ NO detection in combustion gases with a 5.2 μm quantum-cascade laser *Appl Phys B* **106**, 987-97.

- [21] Zhao G, Tan W, Hou J, Qiu X, Ma W, Li Z, Dong L, Zhang L, Yin W, Xiao L, Axner O and Jia S 2016 Calibration-free wavelength-modulation spectroscopy based on a swiftly determined wavelength-modulation frequency response function of a DFB laser *Optics Express* **24(2)**, 1733.
- [22] Rothman L, Gordon I, Babikov Y, Barbe A, Chris Benner D, Bernath P, Birk M, Bizzocchi L, Boudon V, Brown L R, Campargue A, Chance K, Cohen E A, Coudert L H, Devi V M, Drouin B J, Fayt A, Flaud J M, Gamachem R R, Harrison J J, Hartmann J M, Hill C, Hodges J T, Jacquemart D, Jolly A, Lamouroux J, LeRoy R J, Li G, Long D A, Lyulin O M, Mackie C J, Massie S T, Mikhailenko S, Müller H S P, Naumenko O V, Nikitin A V, Orphal J, Perevalov V, Perrin A, Polovtseva E R, Richard C, Smith M A H, Starikova E, Sung K, Tashkun S, Tennyson J, Toon G C, Tyuterev V I G and Wagner G 2013 The HITRAN 2012 molecular spectroscopic database *J Quant Spectrosc Radiat Transf* **130**, 4–50.
- [23] Werle P, Mucke R and Slemr F 1993 The limits of signal averaging in atmospheric trace-gas monitoring by tunable diode-laser absorption spectroscopy (TDLAS) *Appl. Phys. B* **57**, 131-9.

Chapter 4

Design of Residual Gas Analyzer based Mass-Spectrometry for the Measurements of $^{13}\text{CO}_2/^{12}\text{CO}_2$ Isotope ratios in Human Exhaled Breath

4.1 Introduction

A typical concentration level of CO_2 in the Earth's atmosphere is around 0.04%, whereas it varies between 4%-5% in human exhaled breath. Therefore, a human exhales two orders of magnitude higher CO_2 concentration than the inhaled CO_2 concentration and hence exhaled CO_2 carries the unique signature of different physiological processes inside the human body. The three most abundant stable isotopes of CO_2 are $^{12}\text{CO}_2$, $^{13}\text{CO}_2$ and $^{12}\text{C}^{18}\text{O}^{16}\text{O}$ with natural isotopic abundances of 98.42%, 1.10% and 0.39%, respectively. Carbon isotopic analysis, particularly $^{13}\text{CO}_2/^{12}\text{CO}_2$ ratio, is an important tool in geology [1], environmental science [2], biology [3], and medical sciences [4]. In medical sciences, measurement of $^{13}\text{CO}_2/^{12}\text{CO}_2$ isotope ratios in exhaled human breath has opened up a new horizon to the non-invasive diagnosis of human diseases by means of exhaled breath analysis. The

most established and FDA approved breath test is ^{13}C -urea breath test (^{13}C -UBT) for the non-invasive diagnosis of *Helicobacter pylori* (*H. pylori*) infection measuring $^{13}\text{CO}_2/^{12}\text{CO}_2$ isotopic ratio in exhaled human breath [5], which is discussed in the following section.

However, the most critical part of the isotopic analysis is the instrumentation. At present, the most frequently used instruments for the measurement of $^{13}\text{CO}_2/^{12}\text{CO}_2$ isotope ratios in expired breath samples are high-precision gas-chromatography (GC) coupled with isotope ratio mass spectrometers (IRMS). The major disadvantages of the GC-IRMS instrumentations are the extremely high cost, prolonged analysis time, non-portability, hardware complexity and the need for dedicated personnel to maintain and operate the mass spectrometers. The high capital equipment along with hardware intricacy of the GC-IRMS systems have therefore, limited significantly the widespread applicability of the ^{13}C -UBT for non-invasive diagnosis of *H. pylori* infection in both research and routine clinical practices for point-of-care (POC) facilities such as hospitals and doctors' clinics. Recently, numerous cheaper and simpler analytical methods compared to GC-IRMS such as non-dispersive infrared spectrometer and laser assisted ratio analyzer have been developed for ^{13}C -UBT [6] with equivalent sensitivity and specificity. However, these analytical methods have various pros and cons as well as practical limitations for ^{13}C -UBT as described in various literatures [7].

More recently, high-finesse optical cavity-based laser absorption techniques such as cavity ring-down spectroscopy (CRDS) [8,9] and its variant such as off-axis integrated cavity output spectroscopy (OA-ICOS) [10] have been described in the literatures to be a viable tool for measuring high-precision $^{13}\text{C}/^{12}\text{C}$ isotope ratios in CO_2 samples for *H. pylori* detection [11,12]. However, their rapid exploitation for ^{13}C -UBT in routine clinical practices will entirely depend on the portability and affordability of these optical spectrometers regardless of their technological advances for real-time high-precision isotope ratio measurements. Therefore, there is a pressing need for the evaluation of a

simple, robust, cost-effective, and POC system that will be well-suited for breath tests in widespread biomedical applications.

In this chapter, we evaluate the use of a simple and bench-top mass spectrometer called residual gas analyzer (RGA), which is designed to measure the masses of $^{13}\text{C}^{16}\text{O}^{16}\text{O}$ (45 atomic mass unit; amu) and $^{12}\text{C}^{16}\text{O}^{16}\text{O}$ (44 atomic mass unit; amu) isotopes in exhaled breath samples from patients. The RGA-MS is an analytical technique widely used for analyzing the residual gases present in high vacuum (HV) environments ($< 10^{-5}$ Torr). Briefly, in a RGA-MS system, the ions from gas molecules are produced through electron impact ionization when gas molecules collide with thermo electrons discharged from a heated filament and the resulting ions are then separated and detected based on their mass-to-charge ratio (m/z) by utilizing a conventional RF (radio frequency) quadrupole mass filter technology with Faraday Cup detector. The instrumentation that is requisite for this RGA-MS is less expensive, more compact, easy-to-run and more portable than that for conventional GC-IRMS.

In this chapter, the RGA-MS analytical method is standardized and validated by comparison with a diode laser based cavity-enhanced absorption spectroscopic technique called OA-ICOS (described in Section 4.6) for the measurement of $^{13}\text{CO}_2/^{12}\text{CO}_2$ isotopic ratio in human exhaled breath. The clinical efficacy of the RGA-MS method for non-invasive detection of *H. pylori* infection is further confirmed in comparison with an invasive gold-standard method, namely endoscopic biopsy test.

4.2 Overview of *H. pylori* infection and ^{13}C -UBT

H. pylori is one of the most frequent bacterial infectious diseases in human beings worldwide and is now recognized as the key risk factors for chronic gastritis, peptic ulcer, stomach cancer and lymphoma [13,14]. The ^{13}C -urea breath test (^{13}C -UBT) is considered, at present, as the most reliable non-invasive method in the diagnosis of *H. pylori* infection by

contrast with the direct invasive tests such as endoscopy and biopsy-based tests including bacterial culture and rapid urease test (RUT) [15,16]. The ^{13}C -UBT is the preferred non-invasive method for all ages including children, pregnant women and elders because it is safe, simple and quick diagnostic test that can be performed repeatedly without any risk of cross infection. It can also be used for follow-up of *H. pylori* eradication after treatment and for epidemiological studies [7,17].

The underlying principle of ^{13}C -UBT is the high endogenous urease activity of the *H. pylori* microorganism in the human gastrointestinal tract, which cleaves the ^{13}C -enriched urea ($^{13}\text{CO}(\text{NH}_2)_2$) into NH_4^+ and ^{13}C -labelled HCO_3^- , which is then exhaled as $^{13}\text{CO}_2$. Therefore, individuals harbouring *H. pylori* will exhibit an enrichment of $^{13}\text{CO}_2$ in their breath samples following ingestion of ^{13}C -enriched substrate. The $^{13}\text{CO}_2$ enrichment in breath samples is usually reported as the delta-over baseline (DOB) values relative to the international standard Vienna Pee Dee Belemnite value (PDB=0.0112372) in per mil (‰), i.e. $\delta_{\text{DOB}}^{13}\text{C}\text{‰}$ and consequently a $\delta_{\text{DOB}}^{13}\text{C} \geq 2\text{‰}$ is strongly associated with the presence of *H. pylori* infection as reported previously [7,18].

4.3 Notation and Measurement Unit of Isotopic Analysis

The isotopic ratios of $^{13}\text{C}/^{12}\text{C}$ and $^{18}\text{O}/^{16}\text{O}$ of CO_2 are expressed in the typical $\delta^{13}\text{C}\text{‰}$ and $\delta^{18}\text{O}\text{‰}$ notations relative to the standard Vienna Pee Dee Belemnite (PDB) values of $(^{13}\text{C}/^{12}\text{C})_{\text{Standard}} = 0.0112372$ and $(^{18}\text{O}/^{16}\text{O})_{\text{Standard}} = 0.0020672$ as described by Equations 4.1 and 4.2, respectively. The isotopic measurements are typically represented in per mil (‰) unit.

$$\delta^{13}\text{C}\text{‰} = \left(\frac{(^{13}\text{C}/^{12}\text{C})_{\text{sample}}}{(^{13}\text{C}/^{12}\text{C})_{\text{standard}}} - 1 \right) \times 1000 \quad (4.1)$$

$$\delta^{18}\text{O}\text{‰} = \left(\frac{(^{18}\text{O}/^{16}\text{O})_{\text{sample}}}{(^{18}\text{O}/^{16}\text{O})_{\text{standard}}} - 1 \right) \times 1000 \quad (4.2)$$

4.4 Materials and Methods

4.4.1 Subjects

Thirty five subjects (31 male, 4 female, age: 21-72 years) with various gastrointestinal disorders were included in the present study and considered for the ^{13}C -UBT. Depending on the presence or absence of *H. pylori* infection as indicated by the gold standard results of endoscopic biopsy specimens including the urease test, the subjects were classified into two groups: *H. pylori* positive patients (n = 20) and *H. pylori* negative or control patients (n = 15). However, subjects were excluded from the present study if they had been taking antibiotics, proton pump inhibitors or bismuth containing compound in the four weeks preceding the study or if they had recent gastric surgery. All subjects gave written consent to participate in the study. The study was approved by the Ethics Committee Review Board of AMRI Hospital, Salt Lake, India (Study No: AMRI/ETHICS/2013/1).

4.4.2 Breath sample collection

At first, a baseline breath sample was collected in a 750 ml breath collection bag (QT00892, QuinTron Instrument Co. USA) after an overnight fast. Then a drink containing 75 mg ^{13}C -labelled Urea (CLM-311-GMP, Cambridge Isotope Laboratories, Inc. USA) with 4.0 gm citric acid (to slow down gastric emptying) dissolved in 200 ml of water was given to subjects in accordance with the standard procedure as previously described in several reports [15,16,19]. A further breath sample was collected subsequently at 30 minutes (min). All breath samples were repeated and analyzed by the RGA-MS system. The same breath samples were then analyzed by the OA-ICOS system for further validation and comparison of the results obtained from the RGA-MS. All experimental results were expressed in $\delta_{\text{DOB}}^{13}\text{C}\%$ values which refer to the post-baseline and baseline relation of $^{13}\text{CO}_2/^{12}\text{CO}_2$ isotope ratios in exhaled breath samples.

4.4.3 Statistical Analysis

One way analysis of variance (ANOVA) test for parametric variables and Mann-Whitney test for non-parametric variables were used to assess the breath test results. Box and whiskers plots were used to demonstrate the statistical distribution of $\delta_{\text{DOB}}^{13}\text{C}\%$ values in breath samples. A linear regression analysis was carried out to compare the results obtained by both RGA-MS and OA-ICOS methods. A receiver operating characteristic curve (ROC) [20] was also drawn by plotting the true positive rate against false positive rate to find out an optimal diagnostic cut-off value that exhibited the best sensitivity and specificity. All statistical analysis and calculations were performed using Analyse-it Method Evaluation software (Analyse-it Software Ltd. UK, version 2.30) and Origin Pro 8.0. A two-sided p value < 0.05 was considered to indicate statistical significance.

4.5 Design and Function of Residual Gas Analyzer-Mass Spectrometry (RGA-MS)

A schematic diagram of the residual gas analyzer (Prisma Plus, PT-M05-212-111, Pfeiffer vacuum, 1-200 amu) coupled with a customized high vacuum (HV) cylindrical chamber for measuring exhaled breath samples is depicted in Figure 4.1. The typical baseline vacuum level in the HV chamber was $\sim 9.5 \times 10^{-8}$ Torr (1 Torr=1.33 mbar). This was achieved by a turbo molecular pump (PM-153-915-T, $S_p=260$ L/s, Pfeiffer) backed up with a turbo-drag-pump (PM-P03-963A, $S_p=10$ L/s, Pfeiffer) and a diaphragm pump (PK-T01-210, $S_p=40$ L/s, Pfeiffer). The HV chamber is

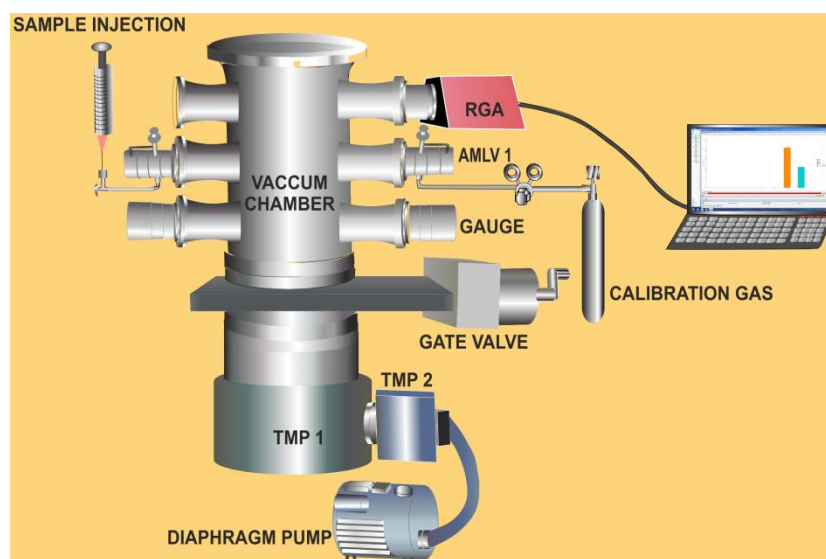


Figure 4.1 Schematic diagram of the residual gas analyzer-mass spectrometry (RGA-MS) system. TMP: Turbo molecular pump, AMLV: all metal leak valve.

also equipped with a manually actuated gate valve (PF-F71-031, Pfeiffer) to establish proper experimental conditions for breath analysis. The pressure inside the HV chamber was monitored by two Pirani gauges (PT-R26-002, Pfeiffer). The typical experimental conditions for analysing the samples were as follows: baseline pressure $1.2\text{-}1.5 \times 10^{-7}$ Torr, working pressure $3.0\text{-}3.5 \times 10^{-5}$ Torr and amount of breath samples or standard calibrate gases injected: ~ 4 mL. A gas tight syringe/stopcock (QuinTron) was used to inject the samples directly into the HV chamber through an all metal leak valve (AMLV) (PFI52031, Pfeiffer) attached with the chamber. The AMLV also facilitated to regulate the flow of samples into the chamber and to maintain the working pressure for the measurements. The ion currents for the masses 44 amu ($^{12}\text{C}^{16}\text{O}^{16}\text{O}$) and 45 amu ($^{13}\text{C}^{16}\text{O}^{16}\text{O}$) were measured with Quadera software (Prisma Plus, version 4.50) compatible with the RGA-MS system by selecting either scan bar-graph mode or multiple ion current detection (MID) mode.

Figure 4.2 depicts a typical RGA mass spectra (subtracted from the baseline) in the scan bar-graph mode showing both $^{12}\text{CO}_2$ ($m/z=44$) and $^{13}\text{CO}_2$ ($m/z=45$) ions when a ~ 4 mL breath sample of a *H. pylori* patient was injected into the HV chamber. The masses were scanned at a scanning rate of 0.2 s/amu (dwell time). The inset shows the change of ion currents with time in the MID mode for the masses 44 and 45 amu. A

total number of 20-25 data points were recorded for each mass at a scanning rate of 0.5s/amu. The data acquisition rate for each of the two

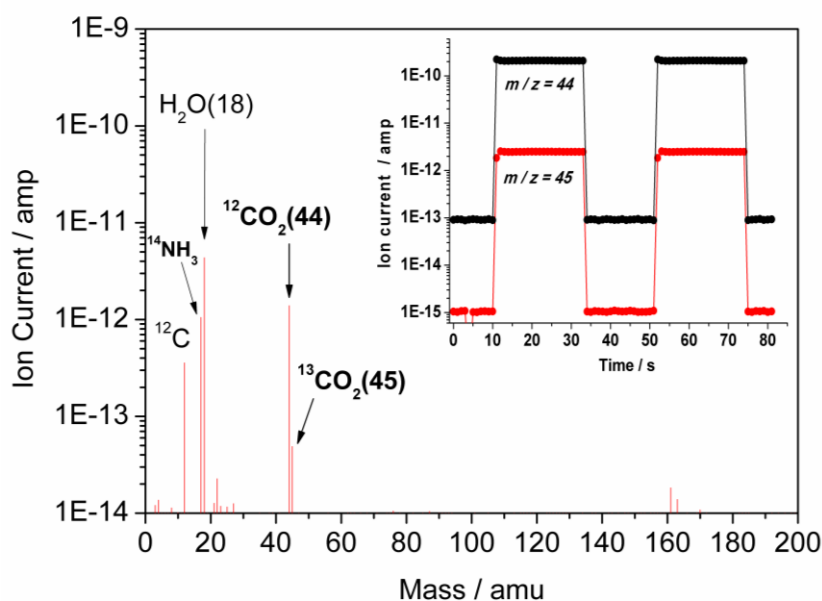


Figure 4.2 A typical RGA mass spectra depicting base-line subtracted ion currents for both $^{12}\text{CO}_2$ (44) and $^{13}\text{CO}_2$ (45) masses of a *H. pylori* patient. The inset displays the change of ion currents with time in seconds (sec) for the masses 44 and 45 amu.

masses was therefore, 1 Hz. The average ion current data of both masses were employed to calculate the $\delta^{13}\text{C}$ values using $\delta^{13}\text{C} = (\text{R}_{\text{sample}} / \text{R}_{\text{standard}} - 1) \times 1000 \text{ ‰}$, where R_{sample} is the average ion current ratio of the sample and $\text{R}_{\text{standard}}$ is 0.0112372. Results were then reported as the delta-over-baseline ($\delta_{\text{DOB}}^{13}\text{C} \text{ ‰}$) value i.e. the difference in the $\delta^{13}\text{C} \text{ ‰}$ values between the baseline and 30 minute breath sample. The typical ion current levels in breath samples for the masses of 44 and 45 amu were in the order of 10^{-10} ampere (amp) and 10^{-12} ampere (amp), respectively, as shown in Figure 4.2.

However, it should also be mentioned here that isotopic species that have identical m/z values for example, $^{13}\text{C}^{16}\text{O}^{16}\text{O}$ (45 amu) and $^{12}\text{C}^{16}\text{O}^{17}\text{O}$ (45 amu), are very difficult to distinguish using the present RGA-MS technique and even with the conventional high-precision GC-IRMS technique. In the present study, the contribution of $^{12}\text{C}^{16}\text{O}^{17}\text{O}$ (45 amu) to the $^{13}\text{C}^{16}\text{O}^{16}\text{O}$ (45 amu) was considered negligible because of its

very low natural abundance (0.037%). In addition, there are several other similar isotopic species present in exhaled breath samples such as $^{14}\text{N}^{14}\text{N}^{16}\text{O}$ (44 amu) and $^{14}\text{N}^{15}\text{N}^{16}\text{O}$ (45 amu) which could contribute to the masses of $^{12}\text{C}^{16}\text{O}^{16}\text{O}$ (44 amu) and $^{13}\text{C}^{16}\text{O}^{16}\text{O}$ (45 amu), respectively. Nevertheless, Kondo *et al.* [21] have previously demonstrated that the N_2O in exhaled breath samples did not significantly change between individuals with *H. pylori* positive and negative. Therefore, it suggests that no correction is important for the contribution of the isotopes of N_2O to the 44 amu and 45 amu peaks measured by the RGA-MS technique. We should also point out that in this study as we ultimately measured the DOB values in exhaled breath samples, any probable errors that might arise from the overlapping masses, were simply eliminated in the $\delta_{\text{DOB}}^{13}\text{C}\%$ measurements.

4.6 Diode Laser based Cavity Enhanced Absorption Technique

In this thesis, we have employed a high-precision carbon dioxide isotope analyzer (CCIA 36- EP, LGR, USA) that exploits a high-finesse optical cavity enhanced absorption technique known as off-axis integrated cavity output spectroscopy (OA-ICOS) to measure simultaneously the absorption features of $^{12}\text{C}^{16}\text{O}^{16}\text{O}$, $^{13}\text{C}^{16}\text{O}^{16}\text{O}$ and $^{12}\text{C}^{18}\text{O}^{16}\text{O}$ isotopes of CO_2 . The ICOS system and its capability to measure high-precision isotope ratios of $^{13}\text{C}/^{12}\text{C}$ and $^{18}\text{O}/^{16}\text{O}$ of CO_2 in exhaled human breath have already been described in depth elsewhere [22-24]. We therefore highlighted here the main features of this ICOS spectrometer. The ICOS system is coupled with a temperature controlled near infrared *cw* DFB laser, operating at $\sim 2.05 \mu\text{m}$. The absorption cell ($\sim 59 \text{ cm}$ long) consists of two high reflectivity cavity mirrors ($R \sim 99.98\%$) and provides an effective optical path length of 3 km. The absorption spectra of $^{12}\text{C}^{18}\text{O}^{16}\text{O}$, $^{12}\text{C}^{16}\text{O}^{16}\text{O}$ and $^{13}\text{C}^{16}\text{O}^{16}\text{O}$ at the wave numbers of 4874.178 cm^{-1} , 4874.448 cm^{-1} and 4874.086 cm^{-1} respectively, were recorded simultaneously by scanning the laser frequency over 20 GHz across the P(36), R(28) and P(16) ro-vibrational lines in the $(2,0^0,1) \leftarrow (0,0^0,0)$

vibrational combination band of the CO₂ molecule. Diaphragm pump and solenoid valves are used to maintain the cavity pressure (~30Torr) and analyze the breath samples. Typically a 25 mL amount of breath sample was injected into the cavity cell by a syringe/stopcock for the measurements. We used high-purity dry N₂ (> 99.99%) as the carrier gas for purging the optical cavity as well as to dilute the breath samples. The real-time absorption spectra were fitted with Voigt profile line shapes and consequently the absolute concentrations of ¹²CO₂, ¹³CO₂ and ¹²C¹⁸O¹⁶O in breath samples were determined by Beer's Law. Furthermore, to check the accuracy and precision of the measurements for δ_{DOB}¹³C‰ and δ_{DOB}¹⁸O‰ values in exhaled breath samples by the ICOS system, we utilized four certified standards containing CO₂ in air with known δ¹³C (Cambridge Isotope Laboratory, CIL, USA, δ¹³C= -22.8‰, -13.22‰ & -7.3‰) and δ¹⁸O (Standard NOAA air tank, Serial No.CB10073, δ¹⁸O= -1.0‰) values. The validation procedures for the measurements of high-precision isotope ratios of ¹³C/¹²C and ¹⁸O/¹⁶O by the ICOS system have been described in the Table 4.1 & Table 4.2. We measured the δ_{DOB}¹³C‰ and δ_{DOB}¹⁸O‰ values in exhaled breath samples with a typical precision of ±0.15‰ and ±0.20‰, respectively.

Table 4.1 Comparison of the δ¹³C‰ values measured by ICOS with that of certified calibration standards. SD corresponds to the 1 standard deviation of three successive measurements.

δ ¹³ C ‰ of certified calibration standards analyzed by IRMS	δ ¹³ C ‰ ± SD measured by ICOS
-22.8	-22.7 ± 0.15
-13.22	-13.34 ± 0.15
-7.3	-7.33 ± 0.15

Table 4.2 Measurements of the $\delta^{18}\text{O}\text{‰}$ values by ICOS of five flasks filled from a certified standard NOAA air tank (Serial No.CB10073).

Flask	$\delta^{18}\text{O}$ (‰) measured by ICOS method
Flask-1	-0.93
Flask-2	-1.28
Flask-3	-0.88
Flask-4	-1.18
Flask-5	-0.82
Avg.	-1.02
Standard Deviation	± 0.20
NOAA	-1.00
Difference	0.02 ± 0.20

In this chapter, we utilized the ICOS system to validate the RGA-MS system for the measurements of $\delta_{\text{DOB}}^{13}\text{C}\text{‰}$ values in the exhaled breath samples.

4.7 Calibration and Validation of the RGA-MS system

We utilized the previously mentioned same three calibration standards containing 5% CO_2 in air with known $\delta^{13}\text{C}$ values (Cambridge Isotope Laboratory, CIL, USA) ranging from baseline-level (-22.8‰) to high-level (-7.3‰) including the mid-level (-13.22‰) to calibrate the RGA-MS system and hence to ensure the accuracy and precision of the measurements for $\delta_{\text{DOB}}^{13}\text{C}\text{‰}$ values in exhaled breath samples. The precision of the RGA-MS was 0.25‰ in the $\delta^{13}\text{C}$ measurements of

calibration standards with accuracy in the range of 97-99%. It should be mentioned here that CIL has developed these three certified calibration standards (Product codes: CLM-3781/3782/3783) analyzed by IRMS technique with a precision of 0.2‰ that mimic the $^{13}\text{CO}_2$ content in normal (baseline), borderline and infected breath samples explicitly for ^{13}C -UBT. The detailed results of the calibration procedure are described in the Table 4.3. Table 4.4 shows comparisons of the $\delta_{\text{DOB}}^{13}\text{C}\text{‰}$ measurements in breath samples from five positive and five negative *H. pylori* patients as an illustration obtained by analysis with both RGA-MS and OA-ICOS methods. The measured $\delta_{\text{DOB}}^{13}\text{C}\text{‰}$ values using the RGA-MS method were in excellent quantitative agreement with the values determined by OA-ICOS method with an average DOB shift of 1.2‰.

Table 4.3 Three standard calibration gases with different $\delta^{13}\text{C}$ values -22.8‰, -13.22‰, and -7.3‰ by OA-ICOS and RGA-MS. The uncertainties on the difference of $\delta^{13}\text{C}$ values measured by the RGA and ICOS spectrometers are the standard deviations of three consecutive measurements.

Difference (‰) of $\delta^{13}\text{C}$ values	Difference (‰) measured by OA-ICOS method ($\pm 0.15\text{‰}$)	Difference (‰) measured by RGA-MS (\pm 0.25‰)
$\delta_1^{13}\text{C}$ (22.8-7.3)‰ = 15.5‰	15.52 ‰	15.68
$\delta_2^{13}\text{C}$ (22.8-13.22) = 9.58‰	9.58 ‰	9.50
$\delta_3^{13}\text{C}$ (13.22-7.3)‰ = 5.92‰	5.93 ‰	6.09

Table 4.4 Comparison of the $\delta_{\text{DOB}}^{13}\text{C}\text{‰}$ values in exhaled breath samples from five positive (P1-P5) and five negative (N1-N5) *H. pylori* patients measured individually by RGA-MS and OA-ICOS methods. The uncertainties on the $\delta_{\text{DOB}}^{13}\text{C}$ values measured by the RGA and ICOS spectrometers are the standard deviations of three consecutive measurements.

Human Subjects	Age (yrs)	Sex	Endoscopy and Biopsy Tests	$\delta_{\text{DOB}}^{13}\text{C}$ (‰) values [$\delta^{13}\text{C}$ (30 min)- $\delta^{13}\text{C}$ (0 min)] ‰	
				OA-ICOS ($\pm 0.15\text{‰}$)	RGA-MS ($\pm 0.25\text{‰}$)
P1	42	M	Positive	12.64	12.11
P2	46	M	Positive	58.35	56.50
P3	36	M	Positive	5.00	3.50
P4	25	M	Positive	18.41	16.99
P5	66	M	Positive	4.75	3.83
N1	29	M	Negative	1.44	0.67
N2	24	M	Negative	0.51	0.12
N3	42	M	Negative	1.82	1.25
N4	47	M	Negative	1.95	1.79
N5	23	M	Negative	0.85	1.45

4.8 Results and Discussions

Figure 4.3 depicts Box and Whisker plots of $\delta_{\text{DOB}}^{13}\text{C}\text{‰}$ values obtained by both RGA-MS and OA-ICOS methods to illustrate the statistical distribution of $^{13}\text{CO}_2$ enrichment in *H. pylori* positive and negative patients. We observed that the mean (29.7‰ vs 1.3‰), median (19.1‰ vs 1.3‰) and inter-quartile ranges (41.3‰ vs 1.2‰) of $\delta_{\text{DOB}}^{13}\text{C}\text{‰}$ values determined by the present RGA-MS technique increased significantly ($p < 0.001$) for the group with *H. pylori* positive patients compared to the

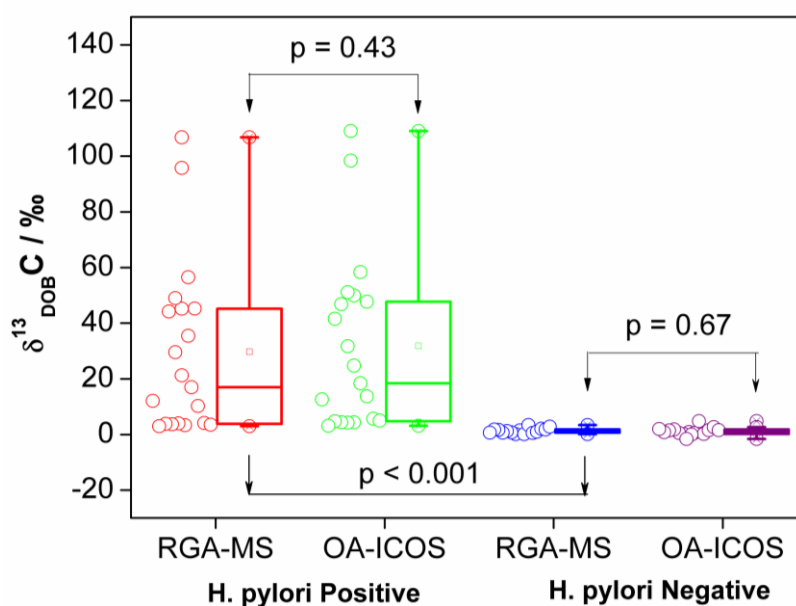


Figure 4.3 Box and Whiskers plots of $\delta_{\text{DOB}}^{13}\text{C}\text{‰}$ values determined by both RGA-MS and OA-ICOS methods illustrating the statistical distribution of $^{13}\text{CO}_2$ enrichment at 30 min in *H. pylori* positive and negative individuals. The scattered points correspond to actual experimental data points.

group with *H. pylori* negative patients. We also found that there were no statistically significant differences between the $\delta_{\text{DOB}}^{13}\text{C}\text{‰}$ values analyzed individually by the spectroscopic (OA-ICOS) and non-spectroscopic (RGA-MS) methods ($p = 0.43$ and 0.67 for positive and negative patients, respectively), indicating the potential of the RGA-MS technique as an alternative analytical tool for exhaled breath analysis to accurately diagnose the *H. pylori* infection.

We also performed the regression statistics to compare the results obtained by RGA-MS to those obtained by OA-ICOS. Figure 4.4 depicts the least square regression plot of $\delta_{\text{DOB}}^{13}\text{C}\%$ values between breath samples analyzed by RGA-MS and those analyzed by OA-ICOS for *H. pylori* positive and *H. pylori* negative individuals. The linear regression analysis of $\delta_{\text{DOB}}^{13}\text{C}\%$ (RGA-MS) versus $\delta_{\text{DOB}}^{13}\text{C}\%$ (OA-ICOS) data provides a slope of 1.0365 and a y-intercept of 0.48‰. The $\delta_{\text{DOB}}^{13}\text{C}\%$ values of both methods demonstrated close correlation as indicated by the squared correlation coefficient of $R^2= 0.9973$.

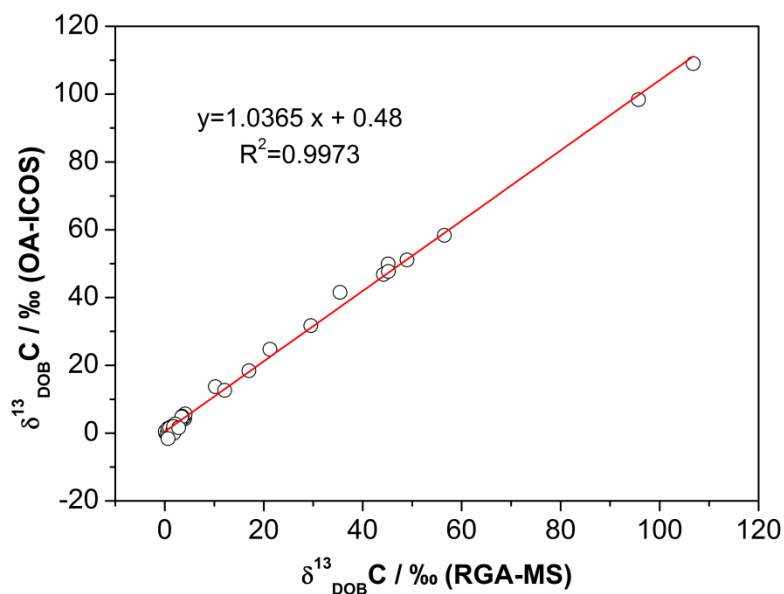


Figure 4.4 Regression plot of the correlation for $\delta_{\text{DOB}}^{13}\text{C}\%$ values between samples analyzed RGA-MS (x-axis) and those analyzed by OA-ICOS (y-axis).

However, to assess the diagnostic accuracy of the RGA-MS methodology to precisely distinguish positive and negative results, a receiver operating characteristic curve (ROC) was constructed by plotting the true positive rate (sensitivity) against false positive rate i.e. (1-specificity) by comparison with the gold standard diagnostic technique. A statistically optimal cut-off point for the present ^{13}C -UBT using the RGA-MS method was defined as the point with the highest sensitivity, specificity and diagnostic accuracy to correctly distinguish individuals with and without *H. pylori* infection.

Figure 4.5 shows a ROC plot for the ^{13}C -UBT using the RGA-MS technique. The optimal diagnostic cut-off value was determined to be $\delta_{\text{DOB}}^{13}\text{C}\text{‰}$ (cut-off) = 3.0‰. Consequently, the RGA-MS system exhibited a sensitivity of 100% (95% confidence interval (CI) 83.2-100) and a specificity of 93% (95% CI 68.1-99.8) with an accuracy of 97%. The area under the ROC curve was also determined to be 0.99 (95% CI 98.0-100), where the statistical significance level of p value was <0.0001 . Using this cut-off value of 3.0‰, the present RGA-MS method precisely diagnosed 20 of 20 patients as positive and 14 of 15 patients as negative (i.e. 1 false positive patient), ensuring the clinical feasibility of the RGA-MS detection method for the diagnosis of *H. pylori* infection without the need for aching endoscopic biopsy test. The present RGA-MS technique exhibited a false positive result (where $\delta_{\text{DOB}}^{13}\text{C}\text{‰} = 3.4\text{‰} > \delta_{\text{DOB}}^{13}\text{C}\text{‰}$ (cut-off) = 3.0‰), whereas the gold standard biopsy test was negative.

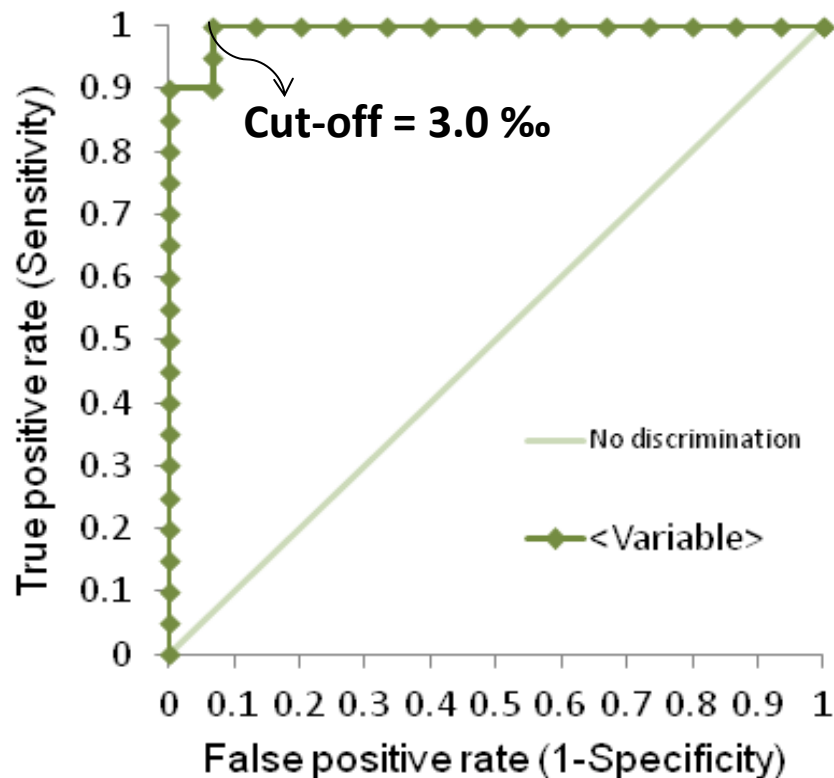


Figure 4.5 Receiver operating characteristic curve (ROC) analysis of the RGA-MS technique exhibiting the optimal diagnostic cut-off value of $\text{DOB}=3.0\text{‰}$.

Interestingly, the OA-ICOS measurement also demonstrated a significant higher value of $\delta_{\text{DOB}}^{13\text{C}}\text{‰} = 4.8\text{‰}$ of that individual compared to the cut-off value of 3.0‰ . The reason of producing false positive results in endoscopy based biopsy test is yet the subject of controversy and subsequently several possible causes have been reported [16,25]. It is known that *H. pylori* has a very patchy distribution throughout the stomach. As a result, the biopsy specimens collected during the endoscopic procedure sometimes can fail to spot the actual site of infection and thus produce false negative results. We speculate that the one false positive result obtained by both analytical methods may actually have been the true positive. Therefore, the RGA-MS approach seems to have the potential to perfectly identify subjects harboring *H. pylori* infection in contrast to gastric biopsy specimens. It also suggests that the endoscopic biopsy tests are only validated for local measurements in some specific sites of the infection, whereas our breath analysis method using the RGA-MS technique is supported for global measurements of the infection throughout the stomach.

However, the effect of endogenous CO_2 production related to the basal metabolic rates (BMR) in individuals may have an influence on the diagnostic accuracy of the present breath analysis by means of RGA-based MS technique. It is expected that if the endogenous CO_2 production varies according to age, weight, height and sex, then the $\delta_{\text{DOB}}^{13\text{C}}\text{‰}$ values are also expected to vary accordingly. To investigate this, we estimated the endogenous CO_2 production of each subject using the Schofield and Mifflin-St Joer Equations [26,27].

Figure 4.6b shows a Box and Whiskers plot of endogenous CO_2 production rate in mmol/min. It is apparent that there was no statistically significant difference ($p=0.82$) between the endogenous CO_2 production rates obtained for *H. pylori* positive and those obtained for *H. pylori* negative individuals. In addition, we determined the cumulative percentage dose of ^{13}C recovered (cPDR %) in breath samples which accounts for the total amount of ^{13}C -urea metabolised at 30 min for both

positive and negative *H. pylori* patients. We applied the following Equation according to Klein *et al.* [28] to calculate the cPDR %:

$$cPDR(\%) = \frac{\delta^{13}_{DOB}C \times R_{PDB} \times 10^{-3} \times V_{CO_2}}{\left(\frac{D}{M_t}\right) \times \left(\frac{30 \text{ min} - 0 \text{ min}}{2}\right)} \quad (4.3)$$

where $\delta_{DOB}^{13}C$ is the DOB values obtained from the RGA-MS measurements, $R_{PDB} = 0.0112372$, D is the dose of substrate administered, M_t = molecular weight of the substrate, and V_{CO_2} is the CO_2 production rate per hour. The results are illustrated by a Box and Whiskers plot and are shown in Figure 4.6a. A marked difference of cPDR (%) values (where significance level of statistical analysis is $p < 0.001$) between two types of subjects demonstrated a sensitive marker of *H. pylori* infection and thus confirmed the feasibility of the RGA-MS technique in the diagnosis of the bacteria.

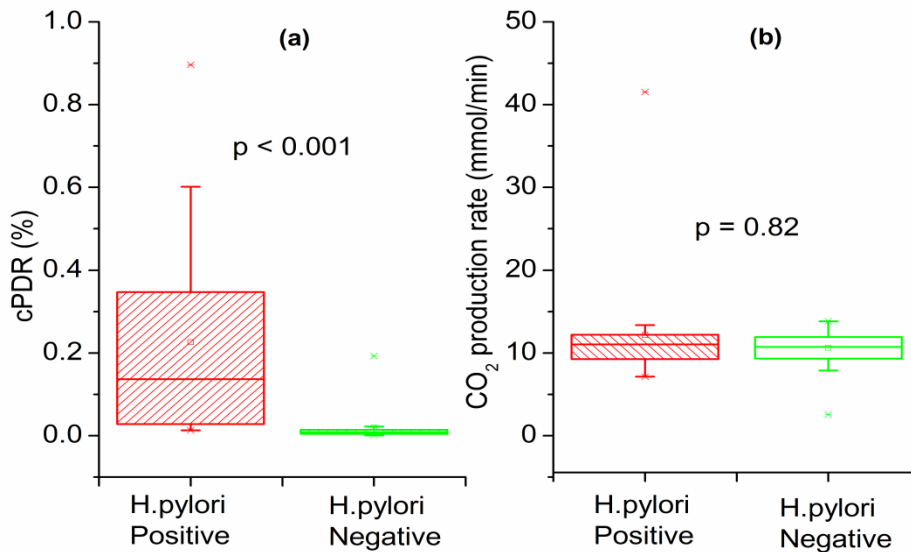


Figure 4.6 Box and Whisker plots of (a) cumulative percentage dose of ^{13}C recovered at 30 min, cPDR (%) and (b) endogenous CO_2 production rates between the two groups of *H. pylori* positive and negative patients.

We finally explored the positive and negative predictive values (PPV and NPV) of the current RGA-MS methodology for diagnostic assessment of the infection. The PPV and NPV express the patients'

probability of getting disease once the actual test results are known [29]. The present RGA-MS technique demonstrated a diagnostic PPV and NPV of 95% and 100%, respectively, indicating an excellent diagnostic accuracy for the identification of *H. pylori* infection. We also applied our results to assess the prevalence of *H. pylori* infection in the Indian population as an illustration.

Figure 4.7 depicts a plot of the prevalence of *H. pylori* infection (%) against the predictive values (%) for the present ^{13}C -UBT. Considering a *H. pylori* prevalence of 70%-80% in the Indian population [30,31], the RGA-MS technique manifested the PPV (%) between 97% to 98% and NPV=100%, making the ability of the present breath analysis technique for screening purposes in community population. However, it is important to note that predictive data may be used to estimate probability of disease but both the parameters vary in accordance with disease prevalence of the infection in the community [29].

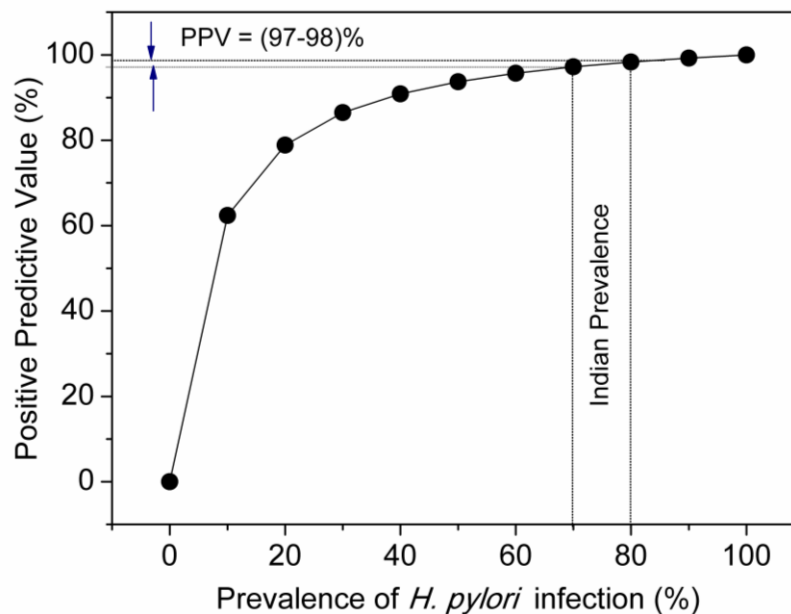


Figure 4.7 Plot of positive predictive values, PPV (%) against prevalence of *H. pylori* infection (%) in the Indian population. The PPV at 30 min past baseline would be between 97% to 98%.

4.9 Conclusions

We have extensively demonstrated the use of a residual gas analyzer (RGA) exploiting the conventional mass spectrometry technique capable of measuring high-precision $^{13}\text{CO}_2/^{12}\text{CO}_2$ isotope ratios in terms of $\delta_{\text{DOB}}^{13}\text{C}\text{‰}$ values in exhaled breath samples from individuals harboring *H. pylori* infection. The RGA-MS system also demonstrated a diagnostic sensitivity of 100% and a specificity of 93%. Accordingly, our study confirms that the present RGA-MS system for breath tests has an enormous potential for accurate determination of *H. pylori* infection without the need for invasive endoscopic tests. The current RGA-MS instrument for the ^{13}C -UBT is compact, more portable, easy-to-run and less expensive compared to the currently available all other optical spectroscopy and mass-spectrometry based detection methods. Therefore, it suggests that the present RGA-based technique could routinely be used as a powerful non-invasive POC medical tool in clinical settings or laboratories for diagnostic evaluation of *H. pylori* infection in real-time. We also conclude that the RGA-MS method presented here is a general approach for the determination of $\delta_{\text{DOB}}^{13}\text{C}\text{‰}$ values in exhaled breath samples from any other diseases or metabolic disorders. Consequently, the RGA-MS technique should have broad applicability for ^{13}C -breath tests in a wide range of biomedical and breath analysis research.

4.10 References

- [1] Quade J and Cerling T E 1990 Stable Isotopic Evidence for a Pedogenic Origin of Carbonates on Trench 14 near Yucca Mountain, Nevada *Science* **250**, 1549.
- [2] Quay P D, Tilbrook B and Wong C S 1992 Oceanic Uptake of Fossil Fuel CO (2): Carbon-13 Evidence *Science* **256**, 74.
- [3] Chapman T E, Berger R, Reijngoud D J and Okken A Eds., *Stable Isotopes in Paediatric Nutritional and Metabolic Research* (Intercept Ltd., Andover, United Kingdom, 1991).
- [4] Graham D Y, Evans D J, Alpert L C, Klein P D, Evans D G, Opekun A R, Boutton T W 1987 *Campylobacter pylori* detected noninvasively by the ¹³C-urea breath test *The Lancet* **329**, 1174-7.
- [5] Amann A, Miekisch W, Schubert J, Buszewski B, Ligor T, Jezierski T, Pleil J and Risby T 2014 Analysis of Exhaled Breath for Disease Detection *Annu. Rev. Anal. Chem.* **7**, 455-82.
- [6] Sararino V, Vigneri S and Celle G 1999 The ¹³C urea breath test in the diagnosis of *Helicobacter pylori* infection *Gut* **45**, I18-I22.
- [7] Koletzko S, Haisch M, Seeboth I, Braden B, Hengels K, Koletzko B and Hering P 1995 Isotope-selective non-dispersive infrared spectrometry for detection of *Helicobacter pylori* infection with ¹³C-urea breath test *Lancet* **345**, 961-2.
- [8] Wheeler M D, Newman S M, Orr-Ewing A J and Ashfold M R 1998 Cavity ring-down spectroscopy *J. Chem. Soc., Faraday Trans.* **94**, 337-51.
- [9] Mazurenka M I, Orr-Ewing A J, Peverall R and Ritchie G D 2005 Cavity ring-down and cavity enhanced spectroscopy using diode lasers *Annu. Rep. Prog. Chem., Sect.* **101**, 100-42.
- [10] O'Keefe A 1998 Integrated cavity output analysis of ultra-weak absorption *Chem. Phys. Lett.* **293**, 331-6.

- [11] Crosson E R *et al.* 2002 Stable isotope ratios using cavity-ring-down spectroscopy: determination of $^{13}\text{C}/^{12}\text{C}$ for carbon dioxide in human breath *Anal. Chem.* **74**, 2003-7.
- [12] Wahl E H *et al.* 2006 Application of cavity ring -down spectroscopy to high-precision isotope ratio measurement of $^{13}\text{C}/^{12}\text{C}$ in carbon dioxide *Isotopes Environ. Health Stud.* **42**, 21-35.
- [13] McColl K E L and El-Omar E 1996 Helicobacter pylori and disturbance of gastric function associated with duodenal ulcer disease and gastric cancer *Scand. J. Gastroenterol. Suppl.* **215**, 32-7.
- [14] Imrie C, Rowland M, Bourke B and Drumm B 2001 Is Helicobacter pylori infection in childhood a risk factor for gastric cancer? *Pediatrics* **107**, 373-80.
- [15] Goddard A F and Logan R P H 1997 Review article: urea breath tests for detecting Helicobacter pylori *Aliment. Pharmacol. Ther.* **11**, 641-9.
- [16] Gisbert J P and Pajares J M 2004 ^{13}C -urea breath test in the diagnosis of Helicobacter pylori infection-a critical review *Aliment. Pharmacol. Ther.* **20**, 1001-17.
- [17] Dzierzanowska-Fangrat K, Lehours P, Megraud F and Dzierzanowska D 2006 Diagnosis of Helicobacter pylori infection *Helicobacter* **11**, 6-13.
- [18] Campuzano-Maya G 2007 An optimized ^{13}C -urea breath test for the diagnosis of H pylori infection *World J. Gastroenterol.* **13**, 5454-64.
- [19] Dominguez-Munoz J E, Leodolter A, Sauerbruch T and Malfertheiner P 1997 A citric acid solution is an optimal test drink in the ^{13}C -urea breath test for the diagnosis of Helicobacter pylori infection *Gut* **40**, 459-62.
- [20] Grzybowski M 1997 Statistical Methodology: III. Receiver operating Characteristic (ROC) curves *Acad. Emerg. Med.* **4**, 818-26.
- [21] Kondo T, Mitsui T, Kitagawa M and Nakae Y 2000 Association of fasting breath nitrous oxide concentration with gastric juice nitrate and

nitrate concentrations and Helicobacter pylori infection *Digestive Disease and Sciences* **45**, 2054-7.

[22] McAlexander I, Rau G H, Liem J, Owano T, Fellers R, Baer D and Gupta M 2011 Deployment of a carbon isotope ratiometer for the monitoring of CO₂ sequestration leakage *Anal. Chem.* **83**, 6223-9.

[23] Baer D S, Paul J B, Gupta M and O'Keefe A 2002 Sensitive absorption measurements in the near-infrared region using off-axis integrated-cavity-output spectroscopy *Appl. Phys. B.: Laser Opt.* **75**, 261-5.

[24] Creedon C T, Verhulst P J, Choi K M, Mason J E, Linden D R, Szurszewski J H, Gibbons S J and Farrugia G 2013 Assessment of gastric emptying in non-obese diabetic mice using a [¹³C]-octanoic acid breath test *J. Vis. Exp.* **73**, e50301.

[25] Jordaan M and Laurens J B 2008 Diagnosis of Helicobacter pylori infection with the ¹³C-urea breath test by means of GC-MS analysis *J. Sep. Sci.* **31**, 329-35.

[26] Schofield W N 1985 Predicting basal metabolic rate, new standards and review of previous work *Hum. Nutr. Clin. Nutr.* **39**, S5-S41.

[27] Mifflin M D, St Jeor S T, Hill L A, Scott B J, Daugherty S A and Koh Y O 1990 A new predictive equation for resting energy expenditure in healthy individuals *Am. J. Clin. Nutr.* **51**, 241-7.

[28] Klein P D, Malaty H M, Czinn S J, Emmons S C, Martin R F and Graham D Y 1999 Normalizing Results of ¹³C-Urea Breath Testing for CO₂ Production Rates in Children *J. Pediatr. Gastroenterol. Nutr.* **29**, 297-301.

[29] Akobeng A K 2006 Understanding diagnostic tests 1: sensitivity, specificity, and predictive values *Acta. Paediatrica.* **96**, 338-41.

[30] Graham D Y, Adam E, Reddy G T, Agarwal J P, Agarwal R, Evans D J, Malaty H M and Evans D G 1991 Seroepidemiology Helicobacter pylori infection in India *Dig. Dis. Sci.* **46**, 1084-8.

[31] Katelaris P H, Tippet G H, Norbu P, Lowe D G, Brennan R and Farthing M J 1992 Dyspepsia, Helicobacter pylori, and peptic ulcer in a randomly selected population in India *Gut* **33**, 1462-6.

Chapter 5

Measurement of ^{18}O isotope of CO_2 in exhaled breath using Diode laser based Cavity Enhanced Absorption Technique for non-invasive detection of *Helicobacter Pylori* infection

5.1 Introduction

In the previous chapter, we showed that $^{13}\text{C}/^{12}\text{C}$ isotope ratio of CO_2 in exhaled human breath was significantly enhanced in response to ^{13}C -enriched urea for *H. pylori* infected individuals. However, the response of ^{18}O isotope of CO_2 , i.e. $^{12}\text{C}^{18}\text{O}^{16}\text{O}$, in exhaled breath was not investigated in the previous chapter. Several evidences [1,2] suggest that *H. pylori* encodes two different forms of the metalloenzyme carbonic anhydrase (α -CA and β -CA) which plays an important role in the interconversion of carbon dioxide and bicarbonate ($\text{CO}_2 + \text{H}_2\text{O} \leftrightarrow \text{H}^+ + \text{HCO}_3^-$) as well as for maintaining the urease activity in the human gastrointestinal tract [3-5]. Some authors [6-8] have also demonstrated that the oxygen-16 (^{16}O) isotope in $^{12}\text{C}^{16}\text{O}_2$ and the oxygen-18 (^{18}O)

isotope of body water (H_2^{18}O) are rapidly exchanged during the human respiration process, catalyzed by CA activity, suggesting the possibility of exploiting the oxygen-isotope fractionations of CO_2 in exhaled breath samples for non-invasive diagnosis of *H. pylori* infections. We therefore hypothesized that monitoring stable $^{18}\text{O}/^{16}\text{O}$ isotope ratios of CO_2 in exhaled breath, expressed as DOB relative to the Vienna Pee Dee Belemnite standard, i.e., $\delta_{\text{DOB}}^{18}\text{O}\text{‰} = [(\delta^{18}\text{O}\text{‰})_{t=t} - (\delta^{18}\text{O}\text{‰})_{t=\text{basal}}]$, may distinctly track the pathogenesis of *H. pylori* infections living in human stomach and hence may introduce a new strategy for the non-invasive diagnosis of *H. pylori* infections.

In this chapter, we demonstrate the potential links between ^{18}O -isotope of breath CO_2 and *H. pylori* infections by exploiting the time-dependent excretion kinetics of the $^{18}\text{O}/^{16}\text{O}$ isotope ratios of CO_2 in breath samples from individuals with and without *H. pylori* infections in response to unlabelled and labelled ^{13}C -enriched urea. We have utilized a laser-based high-resolution cavity enhanced absorption technique called off-axis integrated cavity output spectroscopy (OA-ICOS) to study the breath ^{18}O kinetics.

5.2 Materials and Methods

5.2.1 Human Subjects

In this study, we included 109 human subjects (65 male, 44 female and mean age: 41.10 ± 12.26 yrs) with various gastrointestinal disorders such as duodenal and gastric ulcer, chronic gastritis, and non-ulcer dyspepsia. The Ethics Committee Review Board of AMRI Hospital, Salt Lake, India (Study No: AMRI/ETHICS/2013/1) previously approved the protocol of the current study. We also received the institutional administrative approval from the S.N. Bose Centre, India to work on the human subjects pertinent to this project (Ref. No: SNB/PER-2-6001/13-14/1769). Each patient gave written consent to participate in the study. Subjects were classified into two different groups: *H. pylori* positive patients ($n = 66$) and *H. pylori* negative patients ($n = 43$) on the basis of

“gold-standard” invasive and non-invasive reports including endoscopy and biopsy-based rapid urease test (RUT), and ^{13}C -UBT. An increase of $\delta_{\text{DOB}}^{13}\text{C}\text{‰} \geq 2\text{‰}$ in the ^{13}C -UBT was considered to be indicative of *H. pylori* infection. In this study, a patient was considered to be infected with *H. pylori* only when both test results were positive and if there were any disagreements between the test results, the patient was excluded from the study. We also excluded the patients from the study if they had been taking any antibiotics and proton pump inhibitors in the 4 weeks prior to the endoscopic examination or those who had previous history of diabetes.

5.2.2 Exhaled breath sample collection

The UBT was performed after an overnight fast in all instances within 1-2 days following the endoscopic examination. On the day of breath analysis, the end-expiratory basal breath sample was initially collected from each patient in a breath collection bag (QT00892, QuinTron Instrument Co. USA, 750 ml) before ingestion of the substrate. Then the post-dose breath samples were collected at 15 min intervals upto 60 min following ingestion of a drink containing 75 mg ^{13}C -labelled Urea (CLM-311-GMP, Cambridge Isotope Laboratories, Inc. USA) with 4.0 gm citric acid dissolved in 200 ml of water. All the breath samples were subsequently analysed to determine both $^{18}\text{O}/^{16}\text{O}$ and $^{13}\text{C}/^{12}\text{C}$ isotope ratios of CO_2 in real-time by high-precision laser-based OA-ICOS system as described in the following section.

5.2.3 Off-axis integrated cavity output spectroscopy (OA-ICOS)

OA-ICOS was previously described in Chapter 4; Section 4.6.

5.2.4 Statistical Analysis

Statistical methods were discussed in Chapter 4; Section 4.4.3.

5.3 Results and Discussions

To investigate the carbon-13 and oxygen-18 isotopic enrichments of breath CO_2 , we first studied the time-dependent excretion kinetics of $\delta_{\text{DOB}}^{13}\text{C}\text{‰}$ along with $\delta_{\text{DOB}}^{18}\text{O}\text{‰}$ values in exhaled breath samples from individuals with *H. pylori* positive and negative using the ICOS system. The results of the excretion kinetics patterns of both infected and non-infected individuals following ingestion of ^{13}C -enriched urea have been illustrated in Figure 5.1. It was observed that both $\delta_{\text{DOB}}^{18}\text{O}\text{‰}$ and $\delta_{\text{DOB}}^{13}\text{C}\text{‰}$ values in breath samples follow the similar excretion kinetics. In case of positive patients, both DOB values reached a peak value at around 30 min and then slowly decreased, whereas no significant differences of DOB values in exhaled breath samples were observed for the individuals with *H. pylori*-negative.

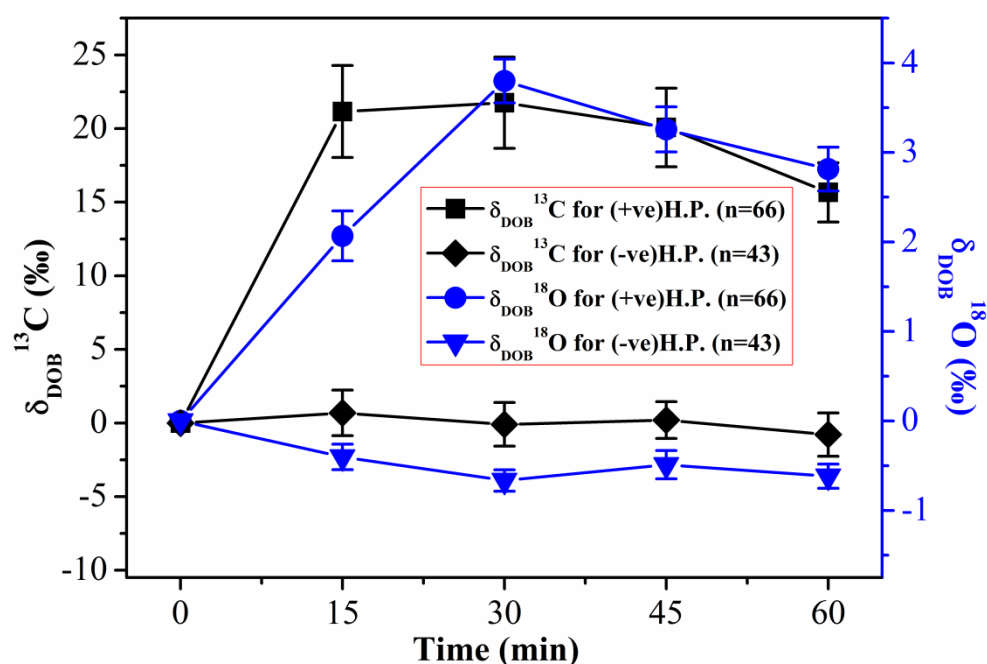


Figure 5.1 The excretion kinetic profiles of $\delta_{\text{DOB}}^{13}\text{C}\text{‰}$ and $\delta_{\text{DOB}}^{18}\text{O}\text{‰}$ values of *H. pylori* positive and *H. pylori* negative individuals for ^{13}C -Urea Breath Test. n is the number of subjects and error bars correspond to standard error of mean. (+ve) H.P. and (-ve) H.P. stand for *H. pylori* positive and *H. pylori* negative patients, respectively.

It was previously reported that the internal urease activity of *H. pylori* i.e. urease-catalyzed hydrolysis of ^{13}C -urea is strongly associated with the enrichments of $^{13}\text{CO}_2$ in breath samples [9-11]. As a result, an increase in $\delta_{\text{DOB}}^{13}\text{C}\text{‰}$ values within 30 min and subsequently the gradual decrease in $\delta_{\text{DOB}}^{13}\text{C}\text{‰}$ values in the excretion kinetics are most likely to be the results of the change in internal urease activity of the bacterial environment. Nevertheless, it was also demonstrated in some earlier reports that carbonic anhydrase (CA) enzymes are essential to maintain the urease activity of *H. pylori* infections [1,3]. The metalloenzyme CA catalyzes the interconversion of CO_2 and HCO_3^- which is important for urease-mediated acid resistance in the gastric environment [2,4]. Moreover, as the oxygen isotopes of CO_2 (^{16}O) and H_2O (^{18}O) are rapidly exchanged during this catalyzation process in response to CA activity, an increase in $\delta_{\text{DOB}}^{18}\text{O}\text{‰}$ values in exhaled breath samples for *H. pylori* positive individuals is possibly attributed to the effects of the oxygen-isotope fractionations of CO_2 in the urease-mediated bacterial environment. Therefore, the large difference in the $\delta_{\text{DOB}}^{18}\text{O}\text{‰}$ values in excretion kinetics exhibited a marked distinction between *H. pylori* positive and negative individuals. In view of this result, our findings suggest a potential link between *H. pylori* infections in stomach and the ^{18}O -isotopic exchange in exhaled breath.

We next investigated the statistical distribution of $\text{C}^{18}\text{O}^{16}\text{O}$ enrichments in breath samples at 30 min in *H. pylori* positive and negative individuals. We utilized the Box and Whisker plot of $\delta_{\text{DOB}}^{18}\text{O}\text{‰}$ values to illustrate the distribution of $\text{C}^{18}\text{O}^{16}\text{O}$ enrichments as shown in Figure 5.2. We observed that the mean, median and interquartile ranges (IQRs) indicating the mid-spread of statistical dispersion of $\delta_{\text{DOB}}^{18}\text{O}\text{‰}$ values for positive patients are 3.79‰, 3.28‰ and 2.62‰ to 3.97‰, respectively. Conversely, for the negative patients the mean, median and IQRs of $\delta_{\text{DOB}}^{18}\text{O}\text{‰}$ values were -0.66‰, -0.81‰ and -1.23‰ to 0.23‰, respectively. There was a statistically significant difference of $\delta_{\text{DOB}}^{18}\text{O}\text{‰}$ values ($p < 0.01$) between the two groups of *H. pylori* positive and negative individuals, thus suggesting that ^{18}O in breath CO_2 could be

used as a potential marker for the non-invasive detection of *H. pylori* infection.

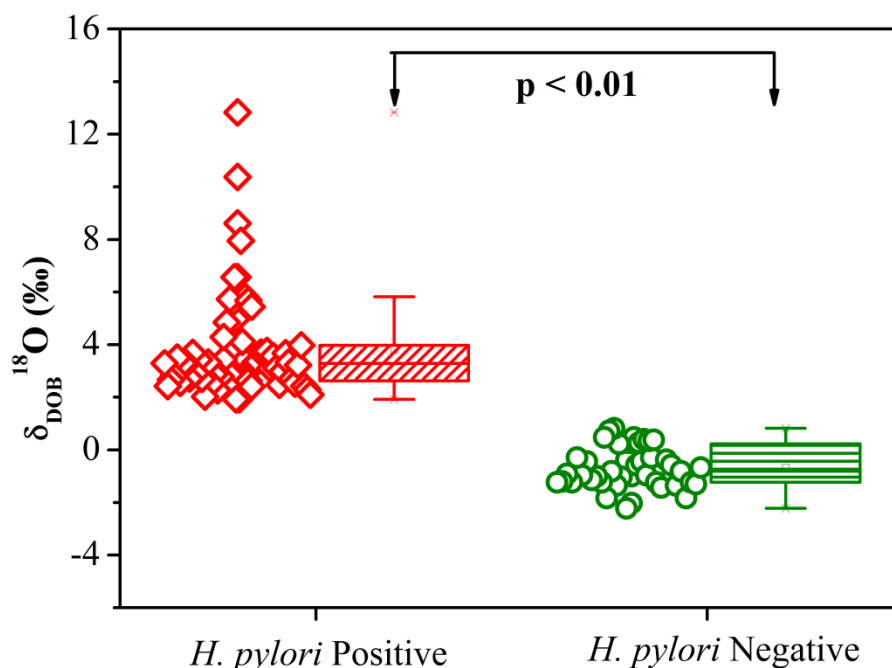


Figure 5.2 A statistical comparison of measured $\delta_{\text{DOB}}^{18}\text{O}$ ‰ values at 30 min for *H. pylori* positive and *H. pylori* negative individuals utilizing Box-whisker plot. The scattered points represented by open-diamond & open-circle symbols correspond to experimental data points measured by ICOS.

We further explored whether the unlabelled urea, $(\text{CO}(\text{NH}_2)_2)$ (i.e. with no ^{13}C -enriched substrate), has any effect in the excretion kinetics of $\delta_{\text{DOB}}^{13}\text{C}$ ‰ and $\delta_{\text{DOB}}^{18}\text{O}$ ‰ values in exhaled breath samples for the *H. pylori* infected persons. Figure 5.3a and 5.3b depict the typical excretion kinetic patterns of $\delta_{\text{DOB}}^{13}\text{C}$ ‰ and $\delta_{\text{DOB}}^{18}\text{O}$ ‰ values for 15 *H. pylori* infected individuals. We observed that when the unlabelled urea was orally administered in positive patients, the $\delta_{\text{DOB}}^{13}\text{C}$ ‰ values in breath samples did not change significantly over time, whereas the $\delta_{\text{DOB}}^{18}\text{O}$ ‰ values in breath manifested a significant change with time and followed the similar excretion kinetics with that of ^{13}C -enriched labelled urea. It is therefore noteworthy that the excretion kinetics of $\delta_{\text{DOB}}^{18}\text{O}$ ‰ followed the similar pattern regardless of the isotopic labelled substrate. This observation is possibly due to the fact that the whole mechanism i.e. urease-catalysed hydrolysis of urea to form bicarbonate and

subsequently CA-mediated inter-conversion of bicarbonate and CO₂ to finally produce ¹²C¹⁶O¹⁸O, solely depends on the substrate (urea) irrespective of its isotopic nature. In case of ¹³C-UBT, ¹³C-labelled urea is essential to observe the ¹³CO₂ isotopic enrichments in exhaled breath

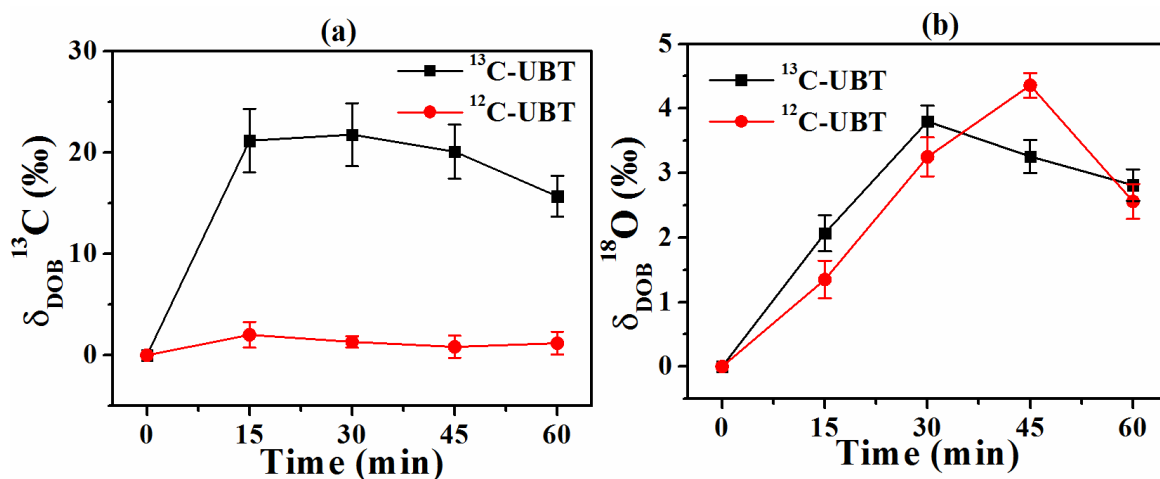


Figure 5.3 A comparison of excretion kinetic patterns of (a) $\delta_{\text{DOB}}^{13}\text{C} \text{‰}$ and (b) $\delta_{\text{DOB}}^{18}\text{O} \text{‰}$ values between ¹³C-Urea Breath Test and unlabelled-Urea Breath Test for 15 *H. pylori* positive patients.

samples for *H. pylori* infected individuals. Therefore, unlabelled urea as a substrate did not contribute to the enhancement of $\delta_{\text{DOB}}^{13}\text{C} \text{‰}$ values for *H. pylori* positive patients and hence no significant changes of $\delta_{\text{DOB}}^{13}\text{C} \text{‰}$ values in breath were observed as shown in Figure 5.3a.

Taken together, these findings indicate that ¹³C-UBT has a clinical applicability only when a patient ingests a ¹³C-enriched labelled urea and accordingly utilizes the $\delta_{\text{DOB}}^{13}\text{C} \text{‰}$ values in breath to correctly diagnose the infection, whilst measuring the $\delta_{\text{DOB}}^{18}\text{O} \text{‰}$ values in exhaled breath may provide a useful way of monitoring the status of *H. pylori* infection and ¹⁸O in breath CO₂ could be used as a potential biomarker of this infection regardless of the unlabelled urea. These data also indicate the potential of $\delta_{\text{DOB}}^{18}\text{O} \text{‰}$ values in exhaled breath as an alternative, cost-effective and robust non-invasive diagnostic approach for *H. pylori* infection and hence may open a new route to diagnose *H. pylori* infections.

We finally determined the optimal diagnostic cut-off point of $\delta_{\text{DOB}}^{18}\text{O}\text{‰}$ values in exhaled breath samples for precisely distinguishing *H. pylori* positive and negative individuals. We have utilized the receiver operating characteristics curve (ROC) analysis by plotting the false positive rate (1-specificity) vs the true positive rate (sensitivity) as shown in Figure 5.4. The statistically sound diagnostic cut-off point of $\delta_{\text{DOB}}^{18}\text{O}\text{‰}$ values was defined as the point where we obtained the highest level of diagnostic sensitivity, specificity and accuracy to correctly identify individuals harboring *H. pylori* infections. In our study, using the ROC analysis the optimal diagnostic cut-off point was determined to be $\delta_{\text{DOB}}^{18}\text{O}\text{‰} = 1.92\text{‰}$. Therefore individuals with $\delta_{\text{DOB}}^{18}\text{O}\text{‰} \geq 1.92\text{‰}$ were considered to be *H. pylori* positive, and this corresponded to the diagnostic sensitivity and specificity of 100 % (95 % CI 94.6-100) and 100 % (95 % CI 91.8-100), respectively along with a diagnostic accuracy of 100%. Furthermore, we have also determined the risk of false positive and false negative results in terms of positive and negative predictive values i.e. PPV and NPV [12] using the cut-off of $\delta_{\text{DOB}}^{18}\text{O}\text{‰} = 1.92\text{‰}$. In our study, both PPV and NPV were estimated to be 100%, demonstrating a superior diagnostic accuracy as well as ability of the present ^{18}O -isotopic methodology for large-scale screening purposes in community population. We therefore posit that monitoring of ^{18}O in breath CO_2 may distinctly track the evolution of *H. pylori* infection prior to the onset of various gastric disorders related to this infection. These findings may also have a broad clinical efficacy for accurate assessment of *H. pylori* infection by human breath analysis and therefore provide a unique approach to treat the world's most common bacterial infective disease in human stomach.

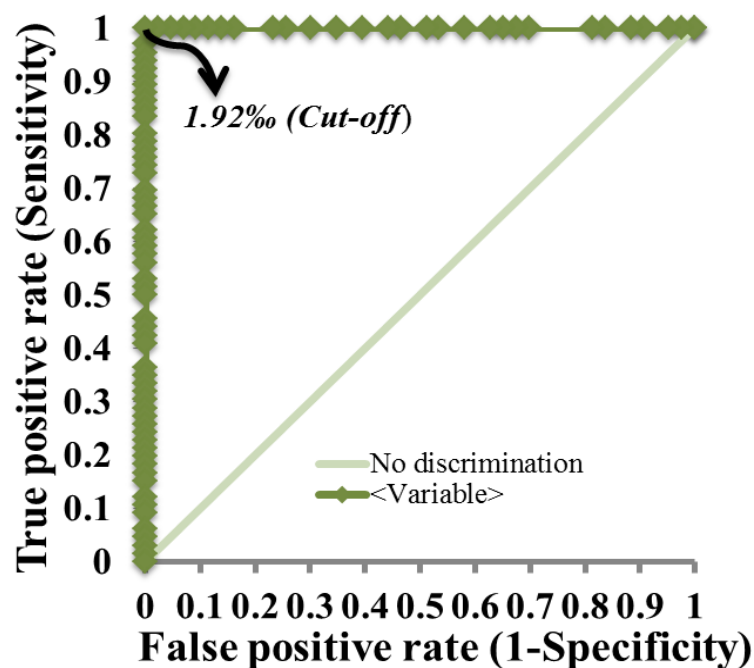


Figure 5.4 Receiver operating characteristic curve (ROC) analysis for the $\delta_{\text{DOB}}^{18}\text{O}\text{‰}$ values. The optimal diagnostic cut-off value was determined to be $\delta_{\text{DOB}}^{18}\text{O}\text{‰} = 1.92\text{‰}$ at 30 min.

5.4 Conclusions

In conclusion, we have extensively demonstrated the time-dependent excretion kinetics of high-precision $^{13}\text{C}/^{12}\text{C}$ and $^{18}\text{O}/^{16}\text{O}$ isotope ratios of CO_2 in terms of $\delta_{\text{DOB}}^{13}\text{C}\text{‰}$ and $\delta_{\text{DOB}}^{18}\text{O}\text{‰}$ values, respectively using an optical cavity enhanced spectroscopy technique in exhaled breath samples from individuals harboring *H. pylori* infection. We have also taken an important step towards the potential link between $^{18}\text{O}/^{16}\text{O}$ isotope ratios of breath CO_2 and *H. pylori* infections, thus suggesting ^{18}O in breath CO_2 could be used as a potential molecular biomarker for the identification of *H. pylori* infections in a non-invasive method. The ^{18}O in breath CO_2 methodology demonstrated a diagnostic sensitivity of 100% and a specificity of 100% along with 100% accuracy, thus making it a powerful and novel alternative diagnostic method for non-invasive assessment of *H. pylori* infection in real-time.

5.5 References

- [1] Bury-Mone S, Mendz G L, Ball G E, Thibonnier M, Stingl K, Ecobichon C, Ave P, Huerre M, Labigne A, Thiberge J M and De Reuse H 2008 Roles of α and β carbonic anhydrases of *Helicobacter pylori* in the urease-dependent response to acidity and in colonization of the Murine gastric mucosa *Infection and Immunity* **76(2)**, 497-509.
- [2] Kaunitz J D and Akiba Y 2006 Duodenal carbonic anhydrase: Mucosal protection, luminal chemosensing, and gastric acid disposal *Keio j Med* **55(3)**, 96-106.
- [3] Krulwich T A, Sachs G and Padan E 2011 Molecular aspects of bacterial pH sensing and homeostasis *Nat Rev Microbiol* **9(5)**, 330-43.
- [4] Marcus E A, Moshfegh A P, Sachs G and Scott D R 2005 The periplasmic α -carbonic anhydrase activity of *Helicobacter pylori* is essential for acid acclimation *Journal of Bacteriology*, **187(2)**, 729-38.
- [5] Marcus E A, Sachs G and Scott D R 2013 The role of ExbD in the periplasmic pH homeostasis in *Helicobacter pylori* *Helicobacter* **18**, 363-72.
- [6] Epstein S and Zeiri L 1988 Oxygen and carbon isotopic compositions of gases respired by humans *Proc. Natl. Acad. Sci. USA*. **85**, 1727-31.
- [7] Gillon J and Yakir D 2001 Influence of carbonic anhydrase activity in terrestrial vegetation on the ^{18}O content of atmospheric CO_2 *Science* **291**, 2584-7.
- [8] Sternberg L Da S L, DeNiro M J and Savidge R A 1986 Oxygen isotope exchange between metabolites and water during biochemical reactions leading to cellulose synthesis *Plant Physiol* **82**, 423-27.
- [9] Som S, Maity A, Banik G D, Ghosh C, Chaudhuri S, Daschakraborty S B, Ghosh S and Pradhan M 2014 Excretion kinetics of ^{13}C -urea breath test: influences of endogenous CO_2 production and dose recovery on the diagnostic accuracy of *Helicobacter pylori* infection *Anal Bioanal Chem* **406**, 5405-12. DOI 10.1007/s00216-014-7951-0.

[10] Rektorschek M, Weeks D, Sachs G and Melchers K 1998 Influence of pH on metabolism and urease activity of *Helicobacter pylori* *Gastroenterology* **115**, 628-41.

[11] Pantoflickova D, Scott D R, Sachs G, Dorta G and Blum A L 2003 ¹³C urea breath test (UBT) in the diagnosis of *Helicobacter pylori*; why does it work better with acid test meals? *Gut* **52**, 933-37.

[12] Akobeng A K 2006 Understanding diagnostic tests 1: sensitivity, specificity and predictive values *Acta Paediatrica* **96**, 338-41.

Chapter 6

Sensing Molecular Hydrogen in breath using a Residual Gas Analyzer for non-invasive diagnosis of Peptic Ulcer and Non-ulcerous Dyspepsia

6.1 Introduction

Peptic ulcer disease (PUD) is a chronic inflammatory condition of the stomach and proximal duodenum that is usually recognized as being caused by the *Helicobacter pylori* infection [1-4]. Although substantial progress has been made over the past decade in understanding the precise role of *H. pylori* bacteria in the pathogenesis of peptic ulcer, adequate treatment modalities along with innovative early-detection strategies of peptic ulcer remain limited [5]. Furthermore, the connection between *H. pylori* and non-ulcerous dyspepsia (NUD) also remains controversial [6-10]. Some early evidences [11-14], however, suggest that pathogenic *H. pylori* species have the ability to utilize molecular hydrogen (H_2) as a respiratory substrate during colonization in the gastric mucosa of mice. Some studies also indicate that H_2 is a by-product of colonic fermentation in the large intestine of humans and is

absorbed into the blood stream and subsequently excreted as exhaled breath [11-13, 15]. These findings suggest the possibility of exploiting H₂ human breath for non-invasive assessment of the early-stage of PUD, in contrast with the direct invasive endoscopy-based biopsy test. Although there are currently several non-invasive methods (such as ¹³C-urea breath test [UBT] and stool antigen test) for the diagnosis of the infection, the actual disease-states that increase the risk of developing ulcer or ulcer-related complications associated with *H. pylori* infection, still remain largely unknown.

Moreover, *H. pylori* contains two metalloenzymes namely, a membrane-bound H₂-uptake-type hydrogenase and urease that have previously been shown to be of particular significance for this bacterium in the gastric environment [3,16]. Several lines of evidence [1,3,17] confirm that the urease enzyme plays an important role in the acid-acclimation process of this neutrophile micro-organism for the survival in the acidic environment and subsequently high urease activity provides the potential virulence factors for causing peptic ulcer. In contrast, the respiratory enzyme hydrogenase, essential for energy production of *H. pylori* through the oxidation of molecular hydrogen ($\text{H}_2 \rightarrow 2\text{H}^+ + 2\text{e}^-$), has recently been proposed [18] to utilize the protons as well as to facilitate the acid resistance for this bacteria producing molecular hydrogen ($2\text{H}^+ + 2\text{e}^- \rightarrow \text{H}_2$). Therefore, it suggests a tantalizing hypothesis that H₂ signalling in human breath may distinctively track the pathogenesis of the preclinical phase of peptic ulcer in response to the enzymatic activity of both the hydrogenase and the urease, and hence may introduce a new strategy for treating peptic ulcer which usually encompasses both gastric and duodenal ulcers. But there is no experimental evidence so far to support such a tantalizing hypothesis. Moreover, the potential role of H₂ produced by colonic fermentations from other host-residing bacteria in the human gastrointestinal tract, predominantly in the pathogenesis of peptic ulcer associated with *H. pylori* infection, has not yet been fully elucidated. In addition, unravelling the precise molecular pathways involved in causing the changes of H₂ signalling in breath influenced by the enzymatic activity of *H. pylori* infection remains a key challenge,

whenever an individual is at high-risk of developing peptic ulcer or non-ulcerative dyspepsia.

In this chapter, we have investigated whether the H₂ signalling in breath is altered in individuals with *H. pylori*-associated peptic ulcers and non-ulcerous dyspepsia following ingestion of citric acid (in the form of lemon and orange juices) in the acid-mediated bacterial environment. As the bacterium gleans additional energy for growth by respiring H₂ through the H₂-uptake hydrogenase activity, we therefore hypothesize that real-time detection of breath H₂ from patients with ulcer complications may allow a new-generation molecular diagnostic marker for early recognition of ulcer in a non-invasive way. We further explored the potential molecular pathways underlying H₂ signalling alteration in the pathogenesis of PUD linked with *H. pylori* infection to gain a better insight into the pathophysiology of *H. pylori*-associated ulcers.

6.2 Materials and Methods

6.2.1 Subjects

One hundred and seventy two individuals (93 male, 79 female, having age 16-74 yrs.), with different gastrointestinal disorders like gastritis, non-ulcer dyspepsia, peptic ulcer, have been enrolled in this study. We divided the individuals into the three discrete categories: non-ulcer dyspepsia (*H. pylori* positive, n=72), peptic ulcer (*H. pylori* positive, n=69) and control (*H. pylori* negative, n=31) based on the reports of both “gold-standard” invasive and non-invasive tests i.e., endoscopy, biopsy-based rapid urease test (RUT) and ¹³C-urea breath test (¹³C-UBT). In ¹³C-UBT, the value of $\delta_{\text{DOB}}^{13\text{C}}$ (‰) $\geq 2\text{‰}$ at 30 minute was reflected as *H. pylori* positive [19, 20]. The *H. pylori* infection status of all the enrolled subjects has been confirmed, only when both the tests showed the same result. The patients, who are receiving antibiotics, proton pump inhibitors or H₂ receptor antagonists four weeks prior to the study, have not been included in the study. Protocol of the current study has been

approved by Ethics Committee Review Board of AMRI Hospital, Salt Lake, Kolkata, India (Study no.: AMRI/ETHICS/2013/1). The administration of S. N. Bose Centre, Kolkata, India, has also approved the protocol of the study (Ref. no.: SNB/PER-2-6001/13-14/1769). The informed written consent of each patient has been taken prior to the inclusion in the study. The detailed study protocol has been demonstrated in the Figure 6.1.

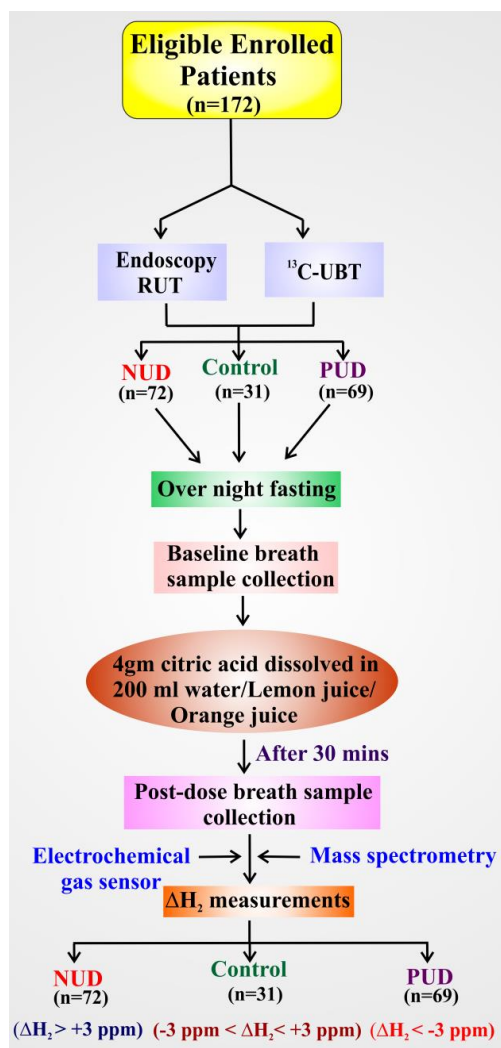


Figure 6.1. A flow diagram representing the steps and the analytical protocol followed in the study.

6.2.2 Breath sample collection

Patients underwent ^{13}C -UBT after overnight fasting within 1-2 days of the endoscopy. For ^{13}C -UBT, the basal exhaled breath sample of each

patient was initially collected in a breath bag (QUINTRON, USA, SL No.QT00892) before the ingestion of test meal. The post-dose breath samples were collected at 15 min interval up to 60 min after the consumption of 75 mg ^{13}C -labeled urea (CLM-311-GMP, Cambridge Isotopic Laboratories, Inc., USA) dissolved in 50 ml of water. Next day, H_2 concentrations (measured in ppm) of the exhaled breath samples of the same individuals were measured before and after the ingestion of only 4.0 g citric acid dissolved in 200 ml water or lemon or orange juice up to 60 min at 15 min interval. For lemon and orange juice, the solution (200 ml) pH has been maintained at 2-3. To measure H_2 concentration of exhaled breath, patients were instructed to blow directly into an electro-chemical gas sensor (Gastrolyzer) for H_2 measurement as well as in to the breath bags to be analyzed mass-spectrometrically. All the breath samples were repeated twice for each interval. The $^{13}\text{C}/^{12}\text{C}$ isotope ratio of breath CO_2 in real-time was measured by a laser-based high-precision off-axis integrated cavity output spectroscopy (ICOS) system whereas H_2 concentration was measured by an electro-chemical gas sensor (Gastro⁺ Gastrolyzer, Bedford Scientific Ltd. Model no.: CE0086) and quadrupole mass-spectrometer (QMS), as described in the following section.

6.2.3 H_2 concentration and $^{13}\text{C}/^{12}\text{C}$ isotope ratio measurements

For H_2 concentration measurement, a gastrolyzer (Gastro⁺ Gastrolyzer, Bedford Scientific Ltd. Model no.: CE0086), based on the principle of an electro-chemical sensor, has been utilized. Accuracy and precision of the instrument on the repeated measurements of a calibration standard H_2 gas (110 ppm) have been tabulated in the Table 6.1. In contrast, quadrupole mass-spectrometry, working on simple mass-spectrometry principle, utilizes a RF quadrupole mass filter technology with Faraday Cup detector to distinguish the ionized gas molecules based on their mass-to-charge ratio (m/z).

Table 6.1 Accuracy and precision of H₂ concentration (ppm) measurements. Results of H₂ concentration (ppm) measurements of five flasks filled from a single certified calibration standard H₂ gas cylinder (110 ppm).

Flask	H₂ concentration (ppm) measured by Electrochemical Sensor
Flask-1	110
Flask-2	109
Flask-3	110
Flask-4	110
Flask-5	111
Avg.	110
Calibration Standard	110
Standard Deviation	±0.7

To measure ¹³C/¹²C isotope ratio of breath CO₂ with high precision and accuracy, a CO₂ isotope analyzer (CCIA 36- EP, LGR, USA), which utilizes off-axis integrated cavity output spectroscopy (OA-ICOS) as a measurement technique, has been described in Chapter 4; Section 4.6.

6.2.4 Statistical analysis

Statistical methods were discussed in Chapter 4; Section 4.4.3.

6.3 Results

To investigate the potential role of H₂ signalling in the pathogenesis of PUD, we first investigated how the time-dependent excretion dynamics of exhaled breath H₂ alters following ingestion of an oral dose of citric acid for patients with PUD and NUD associated with *H. pylori* infection. We monitored the change in breath H₂ concentration (i.e., ΔH_2 in ppm), both mass-spectrometrically and also utilizing an electro-chemical gas sensor, in patients with *H. pylori*-positive PUD (n=48) counting both the duodenal (n=31) and gastric ulcers (n=17), *H. pylori*-positive NUD (n=53), and *H. pylori*-negative controls (n=31). In this investigation (Figure 6.2a), individuals with *H. pylori*-positive NUD exhibited considerably higher enrichments of ΔH_2 in breath samples compared with *H. pylori*-negative control patients during the 1 hour (h)-excretion breath-dynamics, whereas a marked depletion of breath ΔH_2 was manifested in individuals with *H. pylori*-positive PUD. These findings suggest a potential link between *H. pylori*-associated PUD and NUD with breath H₂ signalling and thus may open up a new avenue for the non-invasive evaluation of PUD and NUD.

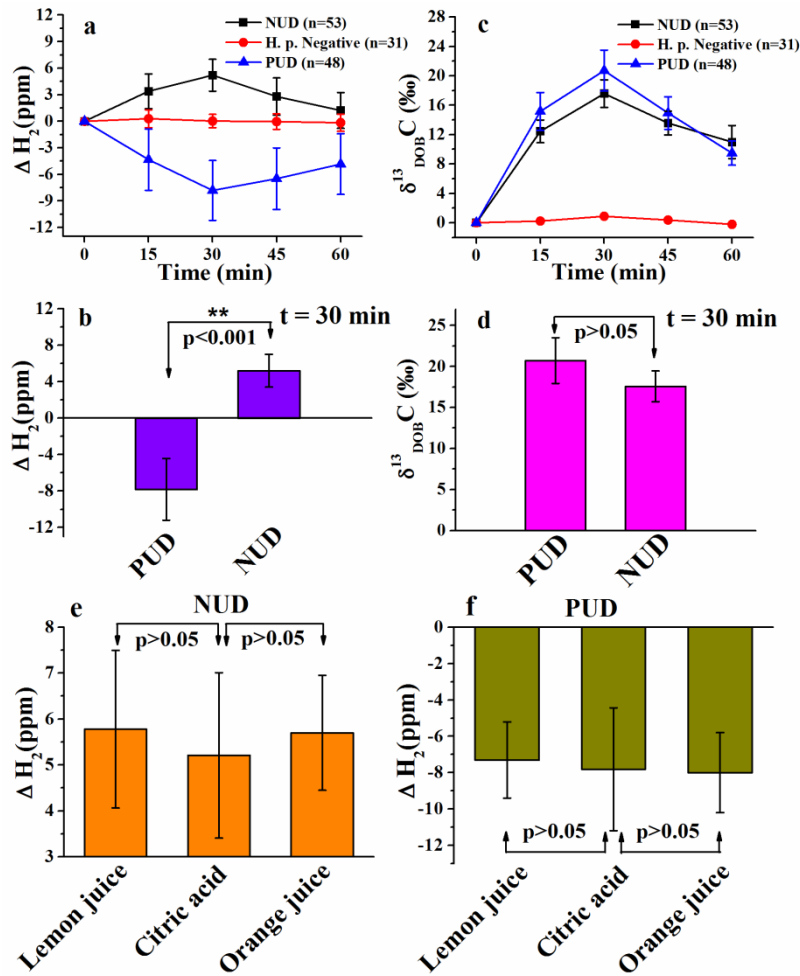


Figure 6.2 Excretion kinetics of both ΔH_2 (ppm) and $\delta_{DOB}^{13}C$ (‰) in exhaled breath H_2 and CO_2 respectively up to 60 min for NUD, PUD and *H. pylori* (*H. p.*) negative individuals along with the statistical comparisons of ΔH_2 values of PUD and NUD for three different acid test meals. **a**, The excretion kinetics of ΔH_2 demonstrated an enrichment for NUD patients and depletion for PUD patients whereas no significant change for *H. p.* Negative patients, thus revealing **(b)** a statistically significant difference ($p < .001$) of ΔH_2 value between PUD and NUD patients at 30 min. **c**, **d**, The excretion kinetics of $\delta_{DOB}^{13}C$ ‰ values illustrated the presence of *H. pylori* infection for both NUD and PUD subjects with a statistically insignificant difference ($p > 0.05$) of $\delta_{DOB}^{13}C$ ‰ values at 30 min. **e**, **f**, The similar and statistically insignificant differences ($p > 0.05$) of ΔH_2 at 30 min were observed for both NUD and PUD patients after the consumption of three different test meals i.e., lemon juice, citric acid solution and orange juice. ** corresponds to $p < 0.001$. All the ΔH_2 data are mean \pm SD whereas it is mean \pm SEM for $\delta_{DOB}^{13}C$ ‰ values.

We also explored the isotopic fractionations of the major metabolite CO₂ after administration of ¹³C-enriched urea, as the potential link between *H. pylori*-infected NUD and PUD subjects with ¹³C/¹²C-stable isotope ratios in breath CO₂, in response to urease activity, remains mostly unknown and also there is no convincing evidence so far how to identify such subjects. To investigate this, we performed the 1h-excretion dynamics of ¹³C-isotopic fractionations of breath CO₂ (Figure 6.2c), expressed as delta-over-baseline (DOB) relative to the Vienna Pee Dee Belemnite standard, i.e., $\delta_{\text{DOB}}^{13\text{C}\text{\textperthousand}} = [(\delta^{13\text{C}\text{\textperthousand}})_{t=t} - (\delta^{13\text{C}\text{\textperthousand}})_{t=\text{basal}}]$, using a laser-based integrated cavity output spectroscopy (ICOS) technique. We observed no significant difference of $\delta_{\text{DOB}}^{13\text{C}\text{\textperthousand}}$ values ($p > 0.05$) between individuals with *H. pylori*-infected NUD and PUD, suggesting that the existing ¹³C-urea breath test by ingestion of external ¹³C-labelled urea has not enough clinical efficacy to distinctively evaluate the actual disease state whether the patient has peptic ulcer or non-ulcerous dyspepsia (Figure 6.2d), whereas the monitoring of breath H₂ signalling is capable of distinguishing precisely subjects with ulcer (PUD) and non-ulcerous dyspepsia (NUD) (Figure 6.2b).

We next explored whether ingestion of an orange or lemon juice has any clinical efficacy to specifically track the progression of PUD and NUD, by tracking H₂ signalling in exhaled breath. In these investigations, there were no statistically significant differences of the ΔH_2 results in breath samples obtained from lemon juice and orange juice for a set of PUD ($n=21$) as well as NUD ($n=19$) patients as compared to the citric acid solution (Figure 6.2e and 6.2f). These results provide evidence that administration of an oral dose of natural fruit juice containing high citric acid has the enormous potential in identifying individuals with PUD and NUD by breath analysis and may also serve as a new-generation diagnostic method for routine clinical analysis as well as for large-scale screening purposes in real-time.

To specifically track the pathogenesis of PUD and NUD using breath H₂ signalling, we subsequently explored optimal diagnostic cut-off points of ΔH_2 values in exhaled breath, using receiver operating characteristics curve (ROC) analysis (Figure 6.3a and 6.3b). Individuals with $\Delta\text{H}_2 \geq 3$

ppm and $\Delta H_2 \leq -3$ ppm at 30 min were considered to be *H. pylori*-infected NUD and PUD respectively, whereas patients with $3 > \Delta H_2 > -3$ were suggested to be *H. pylori*-negative controls and all these corresponded to the typical diagnostic sensitivity and specificity of $\sim 100\%$ and $\sim 100\%$, respectively. In light of these investigations, we propose that breath H_2 signalling may offer new opportunities for treating peptic ulcer or non-ulcerous dyspepsia linked with *H. pylori* infection.

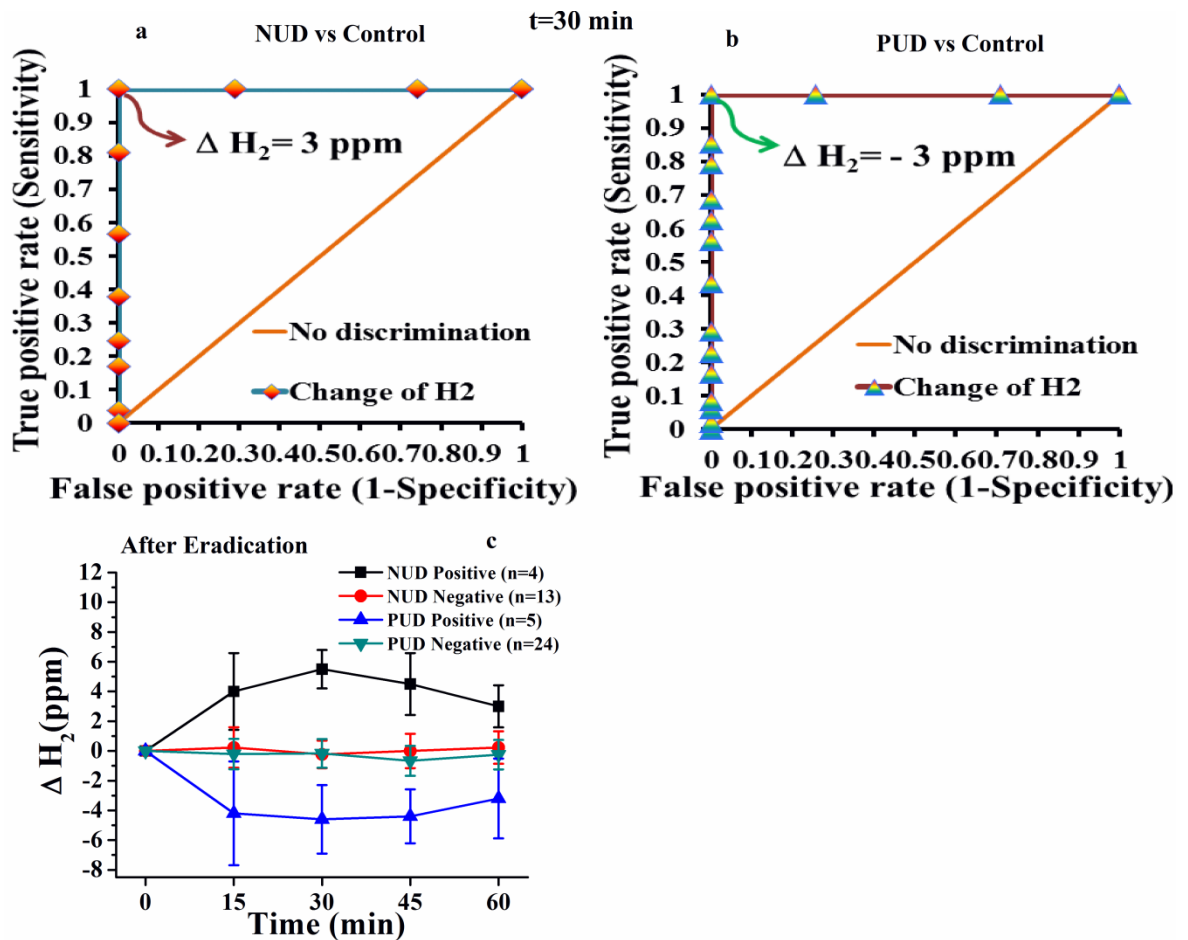


Figure 6.3 Receiver operating characteristic (ROC) curves analyses for the optimal diagnostic cut-off points of both PUD and NUD against *H. p.* negative subjects and the eradication effect on the excretion kinetics of ΔH_2 for NUD and PUD subjects. *a, b*, $\Delta H_2 \geq 3$ ppm and $\Delta H_2 \leq -3$ ppm at 30 min were considered as the indication of non-ulcer dyspepsia (NUD) and peptic ulcer disease (PUD) respectively relative to *H. p.* negative control subjects with 100% sensitivity and specificity. *c*, The successful eradication of the infection for NUD and PUD patients showed the similar excretion pattern of ΔH_2 as that of *H. p.* negative controls. All data are mean \pm SD.

Based on our findings, a major question that still remains to be answered is whether monitoring of breath molecular H₂ signalling can still act as a potential molecular biomarker for the non-invasive assessment of the PUD or NUD subsequent to the eradication of the micro-organism. To gain a better insight into the question, we further explored the validity of the H₂ signalling in response to the standard eradication therapies of the *H. pylori* infection. In this investigation, a number of individuals with *H. pylori*-infected PUD (n = 24) and NUD (n=13) followed the similar excretion profiles of breath H₂ (Figure 6.3c) with the profiles of *H. pylori*-negative controls (Figure 6.2a) and consequently exhibited a marked improvement in symptoms of ulcer and non-ulcerative dyspepsia following the eradication of the infection, suggesting the broad clinical implication of H₂ breath tests. However, contrary to the above results, a little portion of individuals with *H. pylori*-infected PUD patients (n = 5) manifested an indistinguishable change of H₂ signalling in their breath excretion dynamics before (Figure 6.2a) and after the eradication therapy (Figure 6.3c), suggesting that *H. pylori* infections were not eradicated completely and as a result there was no improvement of the symptoms related to ulcer. Our findings thus point towards a considerable clinical advancement for treating both peptic ulcer and non-ulcerous dyspepsia in a new and better way of tracking H₂ signalling in human breath. We have also established the previous hypothesis [6] that *H. pylori* infection is strongly associated with the predominant forms of PUD and the eradication of the infection might cure the ulcer and prevents relapses. In view of our results, we therefore, posit that the monitoring of H₂ signalling in exhaled breath by ingestion of an oral dose of citric acid or even a natural fruit juice (lemon or orange) indicate great promise for new-frontiers in ulcer diagnosis.

6.4 Discussion

The membrane-bound metalloenzyme hydrogenase activity of *H. pylori* has previously been proposed [15, 21] to catalyze the molecular hydrogen into protons and electrons and the reverse reaction, the

generation of molecular hydrogen: $H_2 (\rightleftharpoons H^+ + H^-) \rightleftharpoons 2H^+ + 2e^-$. In our observations, for the NUD patients, the hydrogenase may possibly utilize the reversible reaction ($2H^+ + 2e^- \rightarrow H_2$) to convert the excess H^+ ions in the cytoplasm of *H. pylori* to form H_2 by electron acceptor process under high acidic conditions to maintain the cytoplasmic pH facilitating resistance to acid for its growth [18]. On the contrary, for PUD patients, the urease enzyme released by *H. pylori* is over-expressed, producing a large amount of NH_3 in the bacterial environment [22] utilizing gastric juice urea. The hydrogenase enzyme simultaneously assists to generate additional H^+ ions from H_2 along with the requirement for driving the respiration processes and subsequently protonates the NH_3 to form NH_4^+ in the acidic medium to assist the acid-acclimation process, suggesting that the enzymatic activity of *H. pylori* may play an important role in the depletion of breath H_2 for ulcer patients in the citric acid-mediated bacterial environment and also might be a contributing factor in the pathogenesis of ulceration in the gastric milieu. Thus a statistically significant difference of breath ΔH_2 values in the excretion dynamics established a marked distinction (Figure 6.2b) between NUD and PUD patients harboring *H. pylori* infection. It is noteworthy to mention here that low and stable fasting breath H_2 levels of NUD (5.5 ± 2.01 ppm), PUD (8.68 ± 1.3 ppm) and negative control (7.1 ± 1.8 ppm) potentially eliminate any physiological effect and/or the effect of gut microbes while measuring the change of breath H_2 levels. Moreover, citric acid test meal being free from any carbohydrate avoids any effects of carbohydrate related malabsorption or intolerance in the experimental observations. Taken together, these striking findings signify that the monitoring of breath H_2 signalling may specifically track the evolution of *H. pylori*-associated peptic ulcer and non-ulcerous dyspepsia and thus might be considered as a potential molecular biomarker for the accurate evaluation of PUD and NUD in a non-invasive way.

The most striking finding of the study lies in the observation of H_2 signalling in breath when $^{13}C/^{12}C$ -isotopic fractionation (i.e. $\delta_{DOB}^{13}C\%$ values) of the major metabolite CO_2 in breath fails to track the precise evolution of ulcer. This observation is possibly attributed to the fact that

relatively higher concentration of the virulence factor, such as NH_3 , outside of the micro-organism effectively lowers the net inward proton-motive-force (pmf) [23] for PUD which in turn reduces the amount of urea entry through the UreI channel [24] in comparison to the NUD patients. However, the over-expressed urease enzymatic activity of PUD facilitates the higher utilization of urea relative to the NUD and thus compensates the $\delta_{\text{DOB}}^{13}\text{C}\%$ values for PUD (due to lower amount of urea entry). As a result, no statistically distinguishable $\delta_{\text{DOB}}^{13}\text{C}\%$ values in breath were observed between NUD and PUD patients. Taken together, our findings therefore, point to new perspectives into the accurate diagnosis of NUD and PUD using breath H_2 signalling and thus provide a unique and robust approach for treating these common diseases.

However, we finally explored the possible pathways (Figure 6.4) underlying the molecular mechanisms responsible for the alteration of H_2 signalling in exhaled breath in association with NUD and PUD in the acid mediated bacterial environment. The orally administered citric acid basically provides a higher concentration of H^+ ions outside the micro-organism which generates an inward proton-motive-force (pmf). This pmf eventually leads to the diffusion of H^+ ions into periplasmic and cytoplasmic region of the bacteria, thus lowering the pH of the periplasm and cytoplasm. To survive, *H. pylori* immediately initiates the acid-acclimation [17] process by allowing urea, present in gastric juice, through the UreI channel into the cytoplasm where it is hydrolysed in presence of urease enzyme to produce CO_2 and NH_3 . Both CO_2 and NH_3 then diffuse from cytoplasm to periplasm where α -carbonic anhydrase (α -CA) mediates the conversion of CO_2 into HCO_3^- and H^+ ions [25]. The HCO_3^- ions act as a buffer whereas H^+ ions protonate the NH_3 into weak acid NH_4^+ to regain the periplasmic pH at ~ 6.1 [17]. For NUD, along with the acid-acclimation process, the membrane bound hydrogenase enzyme also facilitates the acid resistance for *H. pylori* by utilizing a part of the diffused H^+ ions, present in both cytoplasm and periplasm, in the production of molecular H_2 ($2\text{H}^+ + 2\text{e}^- \rightarrow \text{H}_2$) [18]. Therefore, the

concentration of H_2 signalling in the exhaled breath of NUD patients enhances after the administration of citric acid.

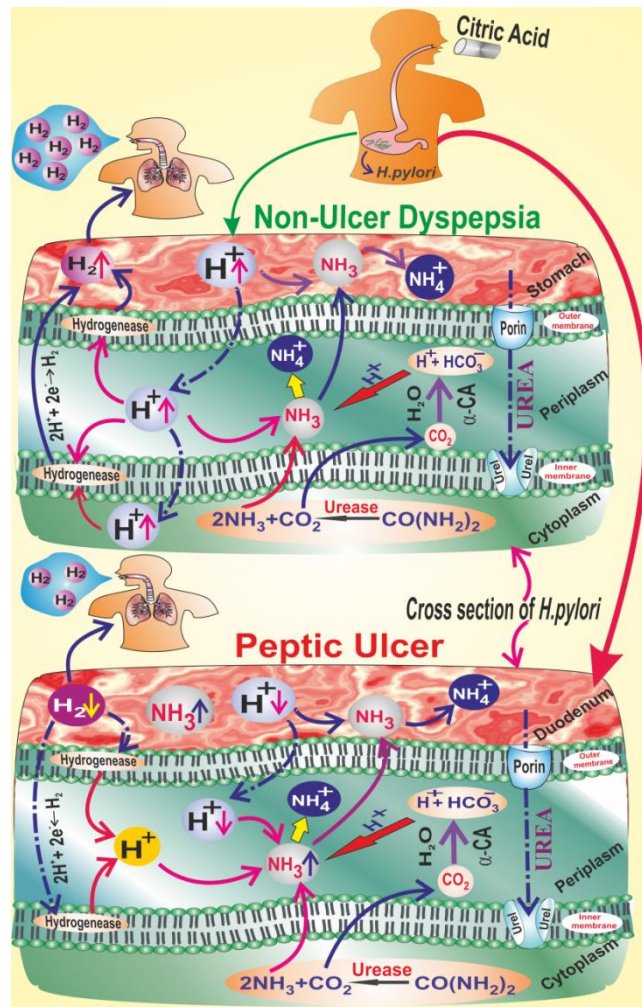


Figure 6.4 Potential pathways for the enrichment and depletion of the H_2 in exhaled breath of NUD and PUD patients respectively. For NUD, to facilitate the acid resistance for *H. pylori* in the citric acid induced environment, along with the acid-acclimation process, the membrane bound hydrogenase enzyme utilizes a part of the H^+ ions diffused in to the cytoplasm and periplasm in the production of molecular H_2 ($2H^+ + 2e^- \rightarrow H_2$). Therefore, an enrichment of molecular H_2 concentration in the exhaled breath of NUD patients is observed after the administration of citric acid. In contrast, for PUD, to protonate large amount of NH_3 , produced due to highly expressed urease enzyme in the acidic medium, the hydrogenase enzyme provides additional H^+ ions utilizing molecular H_2 ($H_2 \rightarrow 2H^+ + 2e^-$) present in the upper-gastro-intestinal tract. Therefore, molecular H_2 concentration in the exhaled breath of PUD patients is depleted after the citric acid consumption.

In contrast, for PUD, much higher concentration of NH_3 around the ulcerous cell effectively lowers the resultant potential gradient of H^+ ions in the bacterial environment in addition of citric acid in comparison to the NUD which in turn reduces the diffusion of H^+ ions in the periplasm of *H. pylori*. However, over-expressed urease activity of *H. pylori* in PUD generates substantial amount of NH_3 [22] in response to the acid-acclimation process. In absence of sufficient H^+ ions in the periplasm, hydrogenase enzyme provides additional H^+ ions to protonate excess NH_3 molecules utilizing molecular H_2 ($\text{H}_2 \rightarrow 2\text{H}^+ + 2\text{e}^-$) present in the upper-gastro-intestinal tract. Therefore, depletion of H_2 signalling in exhaled breath of PUD patients is observed.

6.5 Conclusions

In summary, our findings point to new perspectives towards our understanding the potential relationship between *H. pylori*-associated peptic ulcer or non-ulcerous dyspepsia and molecular hydrogen, produced by colonic fermentations. Consequently, we have taken a step forward in unravelling the possible molecular pathways underlying H_2 alteration in the pathogenesis of PUD and NUD, providing new insights into the pathophysiology of *H. pylori*-related ulcers. Our results also demonstrate that molecular hydrogen signalling in exhaled breath could be used as a potential biomarker for precise classification of PUD and NUD in a new-fangled and better approach in contrast with direct endoscopy-based biopsy test and even with the current ^{13}C -UBT and thus may pave the way for widespread clinical applications for early diagnosis and follow-up of patients following standard eradication-therapies.

6.6 References

- [1] Smoot D T, Mobley H L, Chippendale G R, Lewison J F and Resau J H 1990 *Helicobacter pylori* urease activity is Toxic to human gastric epithelial cells. *American Society for Microbiology* **58**, 1992-4.
- [2] Chan F K L and Leung W K 2002 Peptic-ulcer disease. *Lancet* **360**, 933-41.
- [3] Mobley H L T 1996 The role of *Helicobacter pylori* urease in the pathogenesis of gastritis and peptic ulceration. *Aliment Pharmacol Ther* **10** (Suppl. 1), 57-64.
- [4] Pietroiusti A, Forlini A, Magrini A, Galante A and Bergamaschi A 2008 Isolated *H. pylori* duodenal colonization and idiopathic duodenal ulcers. *Am J Gastroenterol* **103**, 55-61.
- [5] Kao C Y, Sheub B S and Wu J J 2016 *Helicobacter pylori* infection: An overview of bacterial virulence factors and pathogenesis. *Biomedical Journal* **39**, 14-23.
- [6] Peterson W L 1991 *Helicobacter pylori* and peptic ulcer disease. *N Engl J Med* **324**, 1043-8.
- [7] Blum A L *et al.* 1998 Lack of effect of treating *Helicobacter pylori* infection in patients with nonulcer dyspepsia. *N Engl J Med* **339**, 1875-81.
- [8] Chu Y T, Wang Y H, Wu J J and Lei H Y 2010 Invasion and Multiplication of *Helicobacter pylori* in Gastric Epithelial Cells and Implications for Antibiotic Resistance. *Infection and Immunity* **78**, 4157-65.
- [9] Talley N J and Hunt R H 1997 What role does *Helicobacter pylori* play in dyspepsia and nonulcer dyspepsia? Arguments for and against *H. pylori* being associated with dyspeptic symptoms. *Gastroenterology* **113**, 567-77.
- [10] Bernersen B, Johnsen R and Straume B 1996 Non-ulcer dyspepsia and peptic ulcer: the distribution in a population and their relation to risk factors. *Gut* **38**, 822-5.

- [11] Maier R J 2005 Use of molecular hydrogen as an energy substrate by human pathogenic bacteria. *Biochem Soc Trans* **33**, 83-5.
- [12] Maier R J 2003 Availability and use of molecular hydrogen as an energy substrate for *Helicobacter* species. *Microbes and Infection* **5**, 1159-63.
- [13] Olson J W and Maier R J 2002 Molecular hydrogen as an energy source for *Helicobacter pylori*. *Science* **298**, 1788-90.
- [14] Maier R J, Fu C, Gilbert J, Moshiri F, Olson J and Plaut A G 1996 Hydrogen uptake hydrogenase in *Helicobacter pylori*. *FEMS Microbiol Lett* **141**, 71-6.
- [15] Benoit L S and Maier R J 2008 Hydrogen and nickel metabolism in *Helicobacter* species. *Ann. N Y Acad Sci* **1125**, 242-51.
- [16] Lubitz W, Ogata H, Rüdiger O and Reijerse E 2014 Hydrogenases. *Chem Rev* **114**, 4081-148.
- [17] Sachs G, Weeks DL, Wen Y, Marcus E A, Scott D R and Melchers K 2005 Acid acclimation by *Helicobacter pylori*. *Physiology* **20**, 429-38.
- [18] Bhattacharyya S, Krishnarnurthy P, Shaker R, Staff D, Vakil N, Phadnis S H and Dunn B E 2002 *Helicobacter pylori* requires active hydrogenase enzyme to survive under acidic conditions. *Gastroenterology* **118**, A729.
- [19] Gisbert J P and Pajares J M 2004 Review article: 13C-urea breath test in the diagnosis of *Helicobacter pylori* infection-a critical review. *Aliment Pharmacol Ther* **20**, 1001-117.
- [20] Maity A, Banik G D, Ghosh C, Som S, Chaudhuri S, Daschakraborty S B, Ghosh S, Ghosh B, Raychaudhuri A K and Pradhan M 2014 Residual gas analyzer mass spectrometry for human breath analysis: a new tool for the non-invasive diagnosis of *Helicobacter pylori* infection. *J Breath Res* **8**, 016005.
- [21] Nie W, Tang H, Fang Z, Chen J, Chen H and Xiu Q 2012 Hydrogenase: the next antibiotic target? *Clin Sci* **122**, 575-80.

- [22] Kohda K, Tanaka K, Aiba Y, Yasuda M, Miwa T and Koga Y 1999 Role of apoptosis induced by *Helicobacter pylori* infection in the development of duodenal ulcer. *Gut* **44**, 456-62.
- [23] Meyer-Rosberg K, Scott DR, Rex D, Melchers K and Sachs G 1996 The effect of environmental pH on the proton motive force of *Helicobacter pylori*. *Gastroenterology* **111**, 886-900.
- [24] Weeks D L and Sachs G 2001 Sites of pH regulation of the urea channel of *Helicobacter pylori*. *Mol Microbiol* **40**(6), 1249-59.
- [25] Maity A, Som S, Ghosh C, Banik G D, Daschakraborty S B, Ghosh S, Chaudhuri S and Pradhan M 2014 Oxygen-18 stable isotope of exhaled breath CO₂ as a non-invasive marker of *Helicobacter pylori* infection. *J Anal At Spectrom* **29**, 2251-5.

Chapter 7

Measurements of natural isotopic abundances of ^{18}O and ^{13}C -urea in gastric juice using Cavity Enhanced Spectroscopy technique for non-invasive monitoring of ulcer

7.1 Introduction

Over the last few decades, the ^{13}C -urea breath test [^{13}C -UBT] based on the urease activity of the organism has widely been used as a non-invasive diagnostic method to detect exclusively the presence of *H. pylori* infection in the stomach [1,2]. But the current ^{13}C -UBT has not till date adequate efficacies to distinctively assess the actual disease-states i.e. whether the person harboring *H. pylori* infection has the peptic ulcer or non-ulcerous dyspepsia. One salient disadvantage of the ^{13}C -UBT is the influence of urease-positive *non-H. pylori* bacteria in the oral cavity on the results of ^{13}C -UBT [3-5]. Numerous false positive results are thus still observed in the present ^{13}C -UBT because of the consumption of orally administered ^{13}C -enriched urea. Moreover, there are several other drawbacks and pitfalls in the existing ^{13}C -UBT. For example, the optimal diagnostic cut-off point discriminating positive and negative ^{13}C -UBT

results is still a controversial issue [2]. The results of ^{13}C -UBT remain questionable and affect the diagnostic accuracy when the cut-off values are very close to the borderline at the onset of the infection or when the cut-off level lies in a region, so called the “grey-zone” [2]. Therefore there is a pressing need to explore a new-generation strategy which can circumvent all these issues in the existing ^{13}C -UBT and consequently make the diagnosis more sensitive, precise and disease specific.

Studies in the past decade have also demonstrated that ^{16}O in $^{12}\text{C}^{16}\text{O}_2$ and ^{18}O of H_2^{18}O are rapidly exchanged in the gastric juice catalyzed by the metalloenzyme carbonic anhydrase (CA) of *H. pylori* for maintaining the urease activity in its environment [6-8]. But the potential role of ^{18}O -isotopic fractionations in the gastric environment influenced by the enzymatic activity of *H. pylori* especially in the pathogenesis of peptic ulcer or non-ulcerous dyspepsia has not yet been fully explored.

Several lines of evidence [9,10] also suggest that gastric juice contains urea in the range of 3mM to 5mM but its potential link with the infection still remains controversial. Moreover, the natural isotopic abundances of ^{13}C -urea [$^{13}\text{C}^{16}\text{O}(\text{NH}_2)_2$] as well as ^{18}O -urea [$^{12}\text{C}^{18}\text{O}(\text{NH}_2)_2$] in the gastric juice for positive and negative *H. pylori* infected persons are also largely unknown. It therefore suggests a tantalizing hypothesis that utilization of natural isotopic urea in the gastric juice by the *H. pylori* and subsequently monitoring of ^{18}O and ^{13}C of breath CO_2 levels in response to the enzymatic activity may distinctively track the pathogenesis of peptic ulcer, non-ulcerous dyspepsia and *H. pylori* infection. Hence this may bring in a new-generation and cost-effective UBT strategy without any orally administered ^{13}C -labelled external urea for treating the risk of developing ulcer or ulcer-related complications associated with *H. pylori* infection. But until now there has been no study to support such a tantalizing hypothesis. Moreover, without oral ingestion of any ^{13}C -labelled urea, how the accurate diagnosis of *H. pylori* infection along with the actual disease state (i.e. peptic ulcer or non-ulcerous dyspepsia) is possible, that has never been explored before. The reason for the missing information is mainly due to the lack of knowledge of the actual isotopic abundances of the ^{18}O and ^{13}C -urea in human gastric juice. A

new insight into the role of natural ^{13}C and ^{18}O -isotopic urea in gastric juice is therefore essential to elucidate the pathophysiology of *H. pylori* infection and to distinctively track the pathogenesis of peptic ulcer or functional dyspepsia.

In this chapter, we investigated the natural isotopic abundances of ^{18}O and ^{13}C -urea in the gastric juice for *H. pylori* positive and negative patients together with the potential links of both ^{18}O and ^{13}C isotopes of breath CO_2 with the gastric pathogen *H. pylori*. We have subsequently assessed the clinical validity and robustness of the new UBT without ingestion of any external isotopic urea in response to the standard eradication therapies of the infection and finally also determined several novel diagnostic parameters such as diagnostic cut-off values, sensitivity, specificity of ^{18}O and ^{13}C of breath CO_2 to gain a better insight into the diagnostic efficacy for the non-invasive assessment of peptic ulcer, non-ulcerous dyspepsia and *Helicobacter pylori*.

7.2 Materials and Methods

7.2.1 Subjects

In this study, one hundred and forty five individuals (83 male, 62 female, having age 18-67 yrs.), with different gastrointestinal disorders like gastritis, non-ulcer dyspepsia, peptic ulcer, were enrolled after the initial screening. We categorized the enrolled individuals into the three distinct groups: non-ulcer dyspepsia (*H. pylori* positive, n=53), peptic ulcer (*H. pylori* positive, n=57) and *H. pylori* negative (n=35) based on the reports of both invasive and non-invasive “gold-standard” tests i.e., endoscopy, biopsy-based rapid urease test (RUT) and ^{13}C -urea breath test (^{13}C -UBT) respectively. For all the enrolled individuals, there was no contradiction between the test reports of *H. pylori* infection of both the tests. In ^{13}C -UBT, individuals with the value of $\delta_{\text{DOB}}^{13}\text{C}$ (‰) $\geq 2\text{‰}$ at 30 minute were considered to be *H. pylori* positive [1,2,11]. The patients, who were receiving antibiotics, proton pump inhibitors or H_2 receptor

antagonists four weeks prior to the study, were excluded from the study at the initial screening. Ethics Committee Review Board of AMRI Hospital, Salt Lake, Kolkata, India, approved the Protocol of the current study (Study no.: AMRI/ETHICS/2013/1). The administration of S. N. Bose Centre, Kolkata, India, also approved the current study (Ref. no.: SNB/PER-2-6001/13-14/1769). All the patients gave their written consents prior to the study.

7.2.2 Collection of gastric juice

During the endoscopic examinations, ~10 ml of gastric juice from all the enrolled subjects were aspirated through the suction channel of the endoscope and collected in a mucus extractor inserted in the suction line. The gastric juice samples were then stored under -20°C for maintaining protein stability till analysis. Before analysis, the gastric juice samples were centrifuged at 10000 rpm for 10 minutes to further remove the mucus and subsequently the filtrate parts were used for the FTIR and ICOS studies.

7.2.3 Preparations of Chemical solutions

The protein, Jack-bean urease (Sigma Aldrich; E.C. 3.5.1.5), was purchased from Sigma Aldrich with the highest available purity. The ¹³C-enriched urea was acquired from Cambridge Isotope Laboratory (CLM-311-GMP, Cambridge Isotopic Laboratories, Inc., USA) whereas all the other chemicals were procured from Sigma Aldrich. All the chemicals were used without further purification. Milli-Q water was used to prepare the salt solutions. The aqueous solution (0.01nM) of urease was prepared in citrate buffer (10 mM) at pH 7.0. The wide functionality range of citrate buffer was exploited to deal with the different pH levels (1 to 7.6) of the gastric juice samples. The standard solutions (5mM) of both ¹²C and ¹³C-enriched urea were prepared in the same citrate buffer at pH 7.0. The pH measurements of different samples were made utilizing a standard pH meter (ecphtutor-ds).

7.2.4 Fourier Transform Infrared (FTIR) Study

Fourier Transform Infrared (FTIR) spectroscopic measurements were carried out in a JASCO FTIR-6300 spectrometer using CaF₂ windows and a spacer thickness of 100 μm/200 μm in the mid-infrared region (1400–1500 cm⁻¹). For each measurement, 50 scans were acquired at 2 cm⁻¹ resolution. All the spectra were collected taking the buffer solution as a background reference.

7.2.5 Isotopic determination of gastric juice urea

A portion of the filtrate gastric juice was equally divided into two closed round-bottom flasks with an inert atmosphere (N₂). The jack-bean urease solution (0.01nM) was then added into the gastric juice of one of the flasks and other flask contained only the gastric juice sample. After 10 minutes, adequate amount of H₃PO₄ acid was injected into both the flasks for removing the dissolved CO₂ from the sample to its head-space. The head-space CO₂ was thereafter collected from the individual flask and analysed separately for the measurements of isotopic mole-fractions of CO₂ using an isotope-sensitive high-precision off-axis Integrated Cavity Output Spectroscopy (ICOS) as described in the following section. The actual isotopic mole fractions of CO₂, generated from the *in-vitro* chemical hydrolysis of gastric juice urea in response to the external Jack-bean urease, were calculated after subtracting the CO₂ mole-fractions of the other flask originated from the bi-carbonate which was initially present in the gastric juice sample. In this way eliminating the contributions from bicarbonates, the isotopic mole-fractions of CO₂ were utilized for the measurements of isotopic abundances of gastric juice urea. It is noteworthy that an adequate amount of NaOH solution was additionally mixed with the gastric juice samples of pH 1-3 for increasing the pH up to 7 before the addition of external urease and as a result the functionality of the urease remained intact in the gastric juice samples.

7.2.6 Off-axis Integrated Cavity Output Spectroscopy (OA-ICOS)

OA-ICOS was previously described in Chapter 4; Section 4.6.

7.2.7 Breath sample collection

The patients enrolled in the study underwent ^{13}C -UBT within 1-2 days of the endoscopic examination. Prior to the breath test, every patient was instructed to wash his mouth repeatedly to avoid any kind of contamination arising from the oral cavity bacteria. In ^{13}C -UBT, after an overnight fasting (10-12 hours) a baseline breath sample was collected in a breath bag (QUINTRON, USA, SL No.QT00892) after 10 minutes of administration of 4 gm citric acid dissolved in 200 mL of water. The test meal consisting of 75mg ^{13}C -labeled urea (CLM-311-GMP, Cambridge Isotopic Laboratories, Inc., USA) in 50mL of water was then administered and subsequently breath samples were taken at 15 minute intervals for a period of 1 hour. The design of the breath collection bags was such that the oral-breath was first passed through a dead space and then the end tidal breath was captured into the 750 ml reservoir bags utilizing a one-way valve. In this study, we collected an empty stomach breath sample additionally prior to the ^{13}C -UBT.

Next day, to exploit the natural isotopic urea present in the gastric juice, an empty stomach breath was taken after the overnight fasting (10-12 hours) and 4gm citric acid dissolved in 200 mL of water was then administered. Consequently, breath samples were collected at 15 minute intervals till 1 hour. The isotope ratios of $^{13}\text{C}/^{12}\text{C}$ and $^{18}\text{O}/^{16}\text{O}$ in the exhaled breath samples were analyzed using the ICOS technique as mentioned before.

7.2.8 Statistical analysis

Statistical methods were discussed in Chapter 4; Section 4.4.3.

7.3 Results and Discussions

To investigate the natural isotopic abundances of ^{12}C and ^{13}C -urea present in the human gastric juice, we first studied the *in-vitro* chemical reactions of human gastric juice in response to an external Jack-bean urease enzyme (Sigma Aldrich; E.C. 3.5.1.5) using the Fourier transform infrared (FTIR) spectroscopy. In the FTIR analyses, CN stretching vibrational frequencies at 1465 cm^{-1} and 1434 cm^{-1} [12,13] were assigned to qualitatively examine the presence of ^{12}C and ^{13}C -urea, respectively in the human gastric juice samples. The selected vibrational frequencies were also confirmed by utilizing the solutions of ^{12}C and ^{13}C -enriched pure urea substrates. In this *in-vitro* investigation (Figure 7.1a & 7.1b), we observed a significant decrease in peak intensity at different time intervals, demonstrating the possible chemical hydrolysis of urea present in gastric juice catalyzed by external Jack-bean urease and thereby confirming the existence of the different isotopes of urea in the human gastric juice in the qualitative way.

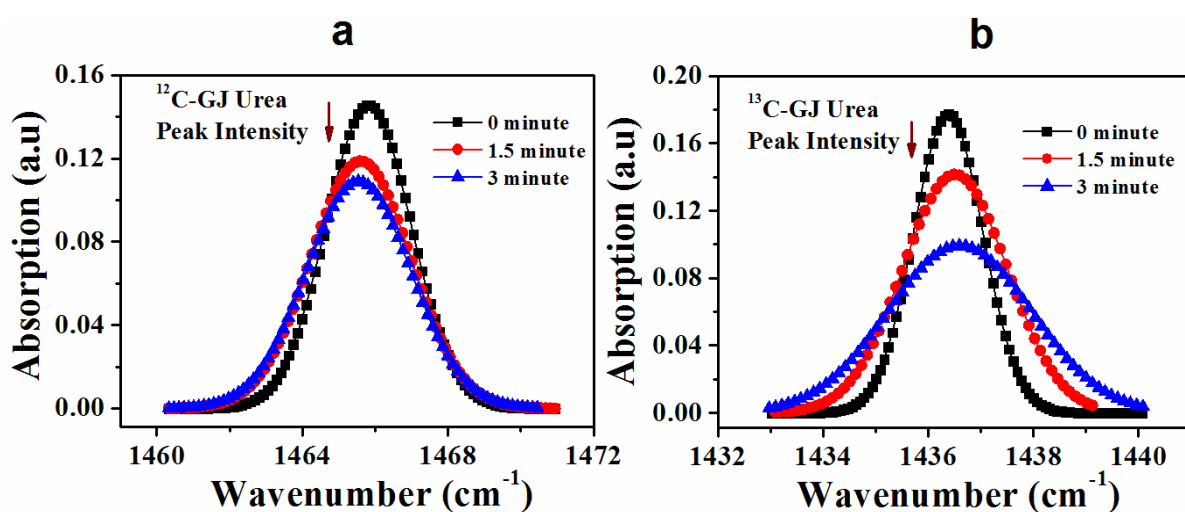


Figure 7.1 FTIR study of gastric juice urea. a) and b) show reduction in peak intensity of urea with time in response to the external Jack-bean urease enzyme for ^{12}C and ^{13}C isotopes respectively exploiting C-N stretching vibrational frequencies. The decrease in peak intensity indicates the manifestation of the possible urea hydrolysis reaction. Larger volume of gastric juice has been exploited for ^{13}C isotope to achieve the reasonable peak intensity.

To evaluate the precise abundances of individual isotopes i.e., ^{12}C , ^{13}C and ^{18}O of urea along with the total amount of urea present in the gastric juice, we analysed the gastric juice for positive and negative *H. pylori* infected individuals utilizing an isotope-selective high-resolution optical integrated cavity output spectroscopy (ICOS) technique. In this unique approach, head-space CO_2 , generated from the chemical break-down of urea present in human gastric juice in response to the external Jack-bean urease, was exploited for the isotope specific measurements of gastric juice urea. In this study (Figure 7.2a), we found statistically insignificant difference ($p > 0.05$) of total gastric juice urea between *H. pylori* positive ($1.78 \pm 0.3(\text{SE})$ mM) and negative ($2.68 \pm 0.44(\text{SE})$ mM) individuals. But, interestingly, a statistical significant difference ($p < 0.01$) of total gastric juice urea was observed between the sub-groups of *H. pylori* positive individuals i.e., between NUD ($2.17 \pm 0.37(\text{SE})$ mM) and PUD ($0.65 \pm 0.20(\text{SE})$ mM) whereas NUD was found to be statistically insignificant ($p > 0.05$) from *H. pylori* negative individuals (Figure 7.2b). This result signifies that higher urease activity of PUD individuals eventually lowered the total gastric juice urea on an average. Our study also sheds light on the contradictory results of the previous reports [9,10] where specific disease states of the *H. pylori* infection had not been studied properly. However, the isotopic analyses (Figure 7.2c & 7.2d) showed that there was statistically insignificant difference ($p > 0.05$) of isotopic abundances (%) between *H. pylori* positive and negative individuals irrespective of the isotopic nature of the gastric juice urea. Nevertheless, the main conclusive outcome of the isotopic analyses was that the abundances of the individual isotopes i.e. ^{12}C (~98.4%), ^{13}C (~1.11%) and ^{18}O (~0.45%) of gastric juice urea were found to be sufficiently high enough to be utilized for non-invasive detection of *H. pylori* infection in conjunction with its urease activity.

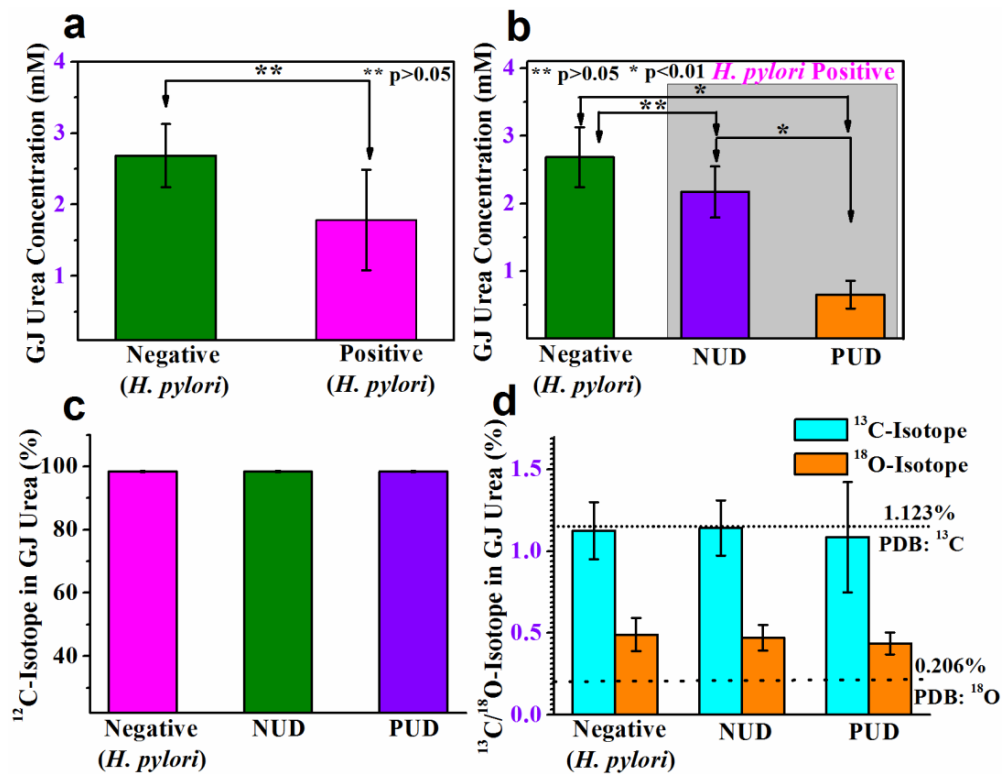


Figure 7.2 Urea concentration and isotopic fractionations in gastric juice of NUD, PUD and *H. pylori* negative patients. a) Total urea concentration in gastric juice of *H. pylori* positive and negative individuals. $p > 0.05$ indicates statistically insignificant difference between both the groups. b) Total urea concentration in gastric juice of PUD can be statistically differentiated from NUD and *H. pylori* negative patients. c) and d) show ¹²C, ¹³C and ¹⁸O isotopic fractionations (%) of total urea content in gastric juice for PUD, NUD and *H. pylori* negative individuals. The abundances of ¹³C and ¹⁸O isotopes in gastric juice show comparable existence to that of the enriched international standard Pee-Dee-Belemnite (PDB).

Now to investigate how the ¹³C and ¹⁸O-isotopic fractionations of breath CO₂ changes without ingestion of any external ¹³C-enriched urea but exploitation of natural isotopic urea present in the gastric juice by *H. pylori*, we studied the time-dependent excretion dynamics of both the isotopes in exhaled breath following ingestion of a citric acid containing test meal for *H. pylori* negative (n = 35) and positive (n=110) individuals with different gastrointestinal disorders such as peptic ulcers (n=57), and non-ulcerous dyspepsia (n=53). We monitored simultaneously ¹³C¹⁶O₂/¹²C¹⁶O₂ and ¹²C¹⁸O¹⁶O/¹²C¹⁶O¹⁶O isotope ratios in exhaled breath

samples associated with the enzymatic activities of urease in the citric acid mediated bacterial environment using a laser-based high-resolution

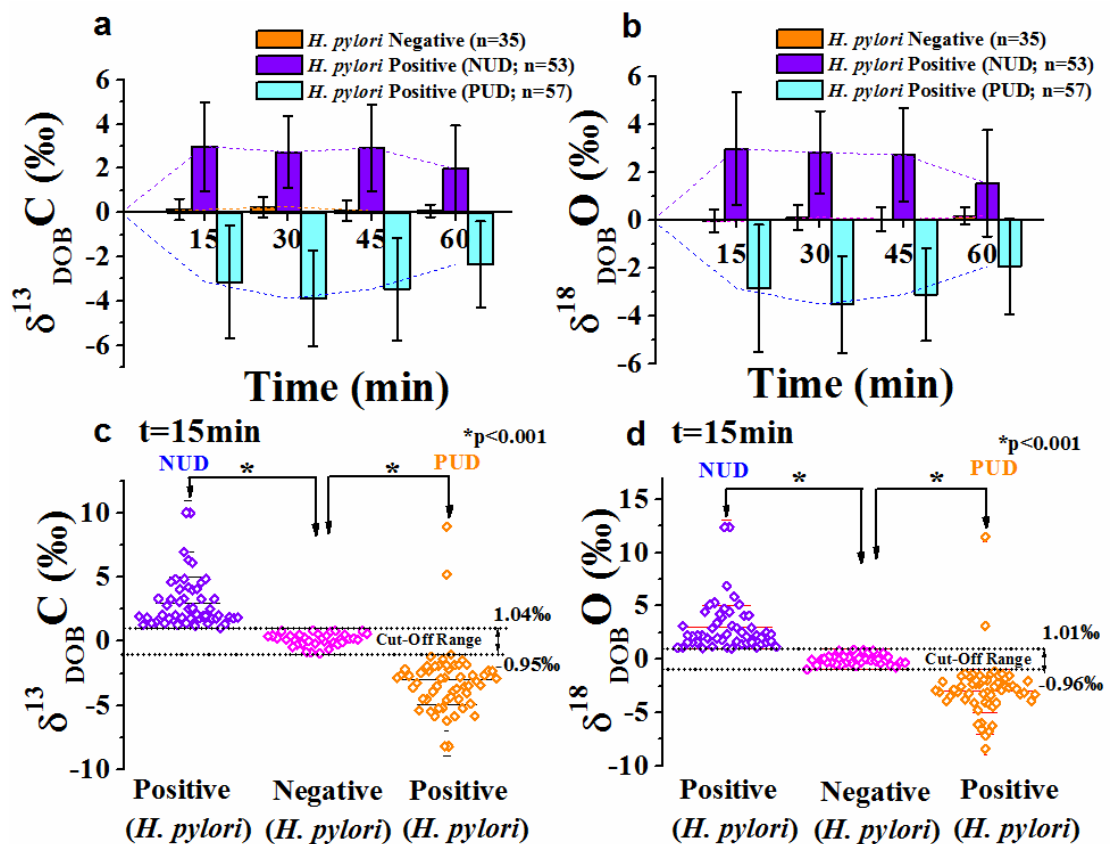


Figure 7.3 Alterations in δ_{DOB} values for ^{13}C and ^{18}O in exhaled breath due to utilization of gastric juice urea by *H. pylori* in response to citric acid. a) Change in $\delta_{DOB}^{13}C$ (‰) values in exhaled breath for NUD, PUD and *H. pylori* negative individuals. A significant enrichment and depletion is observed for NUD and PUD respectively, while no significant change is observed for *H. pylori* negative patients. b) Change in $\delta_{DOB}^{18}O$ (‰) values in exhaled breath for NUD, PUD and *H. pylori* negative individuals follows similar trend as for $\delta_{DOB}^{13}C$ (‰) values. c) and d) show the statistical comparisons of $\delta_{DOB}^{13}C$ (‰) and $\delta_{DOB}^{18}O$ (‰) values between the *H. pylori* positive and the *H. pylori* negative individuals. Cut-off ranges for the distinct diagnosis of *H. pylori* infection are demonstrated both for $\delta_{DOB}^{13}C$ (‰) and $\delta_{DOB}^{18}O$ (‰) values.

integrated cavity output spectroscopy (ICOS) technique. The isotopic fractionations in breath were expressed as usual by the delta-over-baseline (DOB) with respect to the Vienna Pee Dee Belemnite (VPDB)

standard, i.e. $\delta_{\text{DOB}}^{13}\text{C}\text{‰} = [(\delta^{13}\text{C}\text{‰})_{t=t} - (\delta^{13}\text{C}\text{‰})_{t=\text{basal}}]$ and $\delta_{\text{DOB}}^{18}\text{O}\text{‰} = [(\delta^{18}\text{O}\text{‰})_{t=t} - (\delta^{18}\text{O}\text{‰})_{t=\text{basal}}]$. In this investigation (Figure 7.3a & 7.3b), subjects with *H. pylori* positive exhibited two notably distinct excretion kinetic profiles of both ^{18}O and ^{13}C in breath CO_2 depending on the state of the infection i.e. NUD and PUD during the 1h breath excretion studies, while no significant enrichments of both the isotopic species were manifested for *H. pylori* negative individuals.

We observed statistically significant differences of $\delta_{\text{DOB}}^{18}\text{O}\text{‰}$ and $\delta_{\text{DOB}}^{13}\text{C}\text{‰}$ values ($p < 0.001$) among the two sub-groups i.e. NUD and PUD of *H. pylori* infected positive individuals (Figure 7.3c & 7.3d). In case of NUD patients, the higher amount of gastric juice urea as we experimentally observed (see Figure 7.2b) in response to the urease enzyme secreted by *H. pylori*, was possibly attributed to the isotopic enrichments of both $\delta_{\text{DOB}}^{13}\text{C}\text{‰}$ and $\delta_{\text{DOB}}^{18}\text{O}\text{‰}$ values, whereas for PUD patients much lower amount of gastric juice urea was supposed to be responsible for the depletion of $\delta_{\text{DOB}}^{13}\text{C}\text{‰}$ and $\delta_{\text{DOB}}^{18}\text{O}\text{‰}$ values. In view of these results, cut-off ranges of $-0.95\text{‰} \geq \delta_{\text{DOB}}^{13}\text{C} \geq 1.04\text{‰}$ and $-0.96\text{‰} \geq \delta_{\text{DOB}}^{18}\text{O} \geq 1.01\text{‰}$ were calculated with 100% sensitivity and specificity to diagnose the presence of *H. pylori* infection in this new UBT methodology. Taken together, these findings suggest that *H. pylori* has the ability to utilize the natural ^{13}C and ^{18}O -urea in the gastric juice and consequently the precise distinction between *H. pylori* infected and non-infected individuals is possible by monitoring ^{13}C and ^{18}O of breath CO_2 , thus unveiling a missing link between *H. pylori* infection and ^{13}C and ^{18}O -isotopic exchange in exhaled breath without oral administration of ^{13}C -labelled urea and hence may open a new UBT strategy to diagnose *H. pylori* infection. We have also established the earlier hypothesis that the urease-catalyzed hydrolysis of natural ^{13}C -urea and ^{18}O -urea in the gastric juice is strongly associated with the alteration of $^{13}\text{C}^{16}\text{O}_2$ and $\text{C}^{18}\text{O}^{16}\text{O}$ in breath samples.

We next explored, based on the previously observed (Figure 7.3a & 7.3b) two distinct excretion dynamics of both $\delta_{\text{DOB}}^{13}\text{C}\text{‰}$ and $\delta_{\text{DOB}}^{18}\text{O}\text{‰}$ in individuals with *H. pylori* infection, whether the new UBT without the utilization of any external ^{13}C -labelled urea has the sufficient efficacy to

selectively track the actual disease state i.e. where the subject has peptic ulcer (PUD) or non-ulcer dyspepsia (NUD) associated with the *H. pylori* infection. We determined the optimal diagnostic cut-off values of $\delta_{\text{DOB}}^{13}\text{C}\text{‰}$ and $\delta_{\text{DOB}}^{18}\text{O}\text{‰}$ of the new UBT to selectively track the PUD and NUD, using the receiver operating characteristics curve (ROC) analysis. In the new UBT not including any ^{13}C -labelled urea, individuals with $\delta_{\text{DOB}}^{13}\text{C}\text{‰} \geq 1.04$ and $\delta_{\text{DOB}}^{18}\text{O}\text{‰} \geq 1.01$ were considered to be NUD and these manifested the diagnostic sensitivity and specificity of 100% (Figure 7.4a & 7.4b). In contrast, $\delta_{\text{DOB}}^{13}\text{C}\text{‰} \leq -0.95$ and $\delta_{\text{DOB}}^{18}\text{O}\text{‰} \leq -0.96$ indicated PUD with ~96% sensitivity and 100% specificity and two false negative outcomes (Figure 7.4a & 7.4b). We then critically assessed the false negative results and found significant enhancements ($>1.5\text{‰}$) of both $\delta_{\text{DOB}}^{13}\text{C}\text{‰}$ and $\delta_{\text{DOB}}^{18}\text{O}\text{‰}$ values in the exhaled breath as a direct consequence of high urea concentrations in the gastric juices of these PUD individuals. Furthermore, the detailed characteristic study of the specific state of the infection revealed that these individuals were suffering from peptic ulcer bleeding. We therefore speculate that blood-urea may play a vital role for the enhancement of urea concentration in the gastric juice of these two PUD individuals. We further assessed clinical validity and widespread efficacy of new UBT for eradication purposes. Figure 7.4c & 7.4d demonstrate the clinical feasibility of the new UBT in response to the standard antibiotic therapies of the infection and thus provide a new generation methodology for the early detection and follow-up of patients after eradication of *H. pylori* infection. In view of these results, our findings point to new perspectives into the pathogenesis of the disease and the potential mechanisms linking breath ^{13}C and ^{18}O -isotopes to ulcer and non-ulcerous dyspepsia.

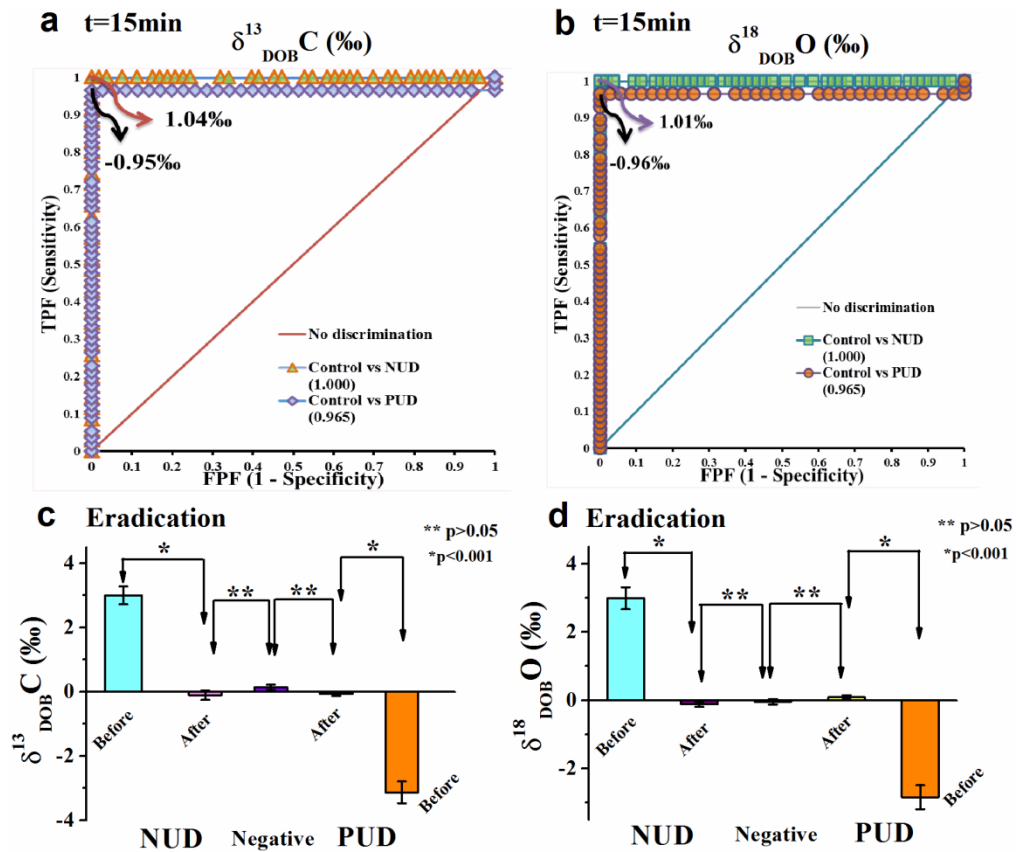


Figure 7.4 Receiver Operating Characteristics (ROC) curve for determining diagnostic cut-off values. Viability of the new UBT before and after the eradication of the disease. a) and b) depict the ROC analysis for the determination of cut-off values for the specific discrimination of PUD, NUD and *H. pylori* negative patients for $\delta_{\text{DOB}}^{13}\text{C}$ (‰) and $\delta_{\text{DOB}}^{18}\text{O}$ (‰) respectively. NUD patients could be well distinguished with 100% sensitivity and specificity while PUD showed ~96% sensitivity and 100% specificity. c) and d) Comparison in the values of $\delta_{\text{DOB}}^{13}\text{C}$ (‰) and $\delta_{\text{DOB}}^{18}\text{O}$ (‰) before and after the eradication therapy depicting the absence of the infection after the therapy with no significant difference with *H. pylori* negative group.

Finally, we addressed the missing-link of ‘grey-zone’ problem in standard ^{13}C -UBT and the efficacy of the new UBT not including any ^{13}C -labelled urea to overcome the ‘grey-zone’ problem. After incorporating the empty stomach breath sample into the standard ^{13}C -UBT protocol where ^{13}C -enriched urea was administered after 10 minutes of citric acid ingestion, we observed a significant enrichment of $\delta_{\text{DOB}}^{13}\text{C}$ ‰ value for NUD within the 10 minutes of acidification in bacterial environment through the administration of citric acid and

thereby indicating that *H. pylori* had already started to utilize the gastric juice urea to alkalize the medium. Now, administration of ^{13}C -labelled urea thereafter may eventually show less enrichment of $\delta_{\text{DOB}}^{13}\text{C}\%$ value for the on-set of the infection and thus raising the inconclusive result or

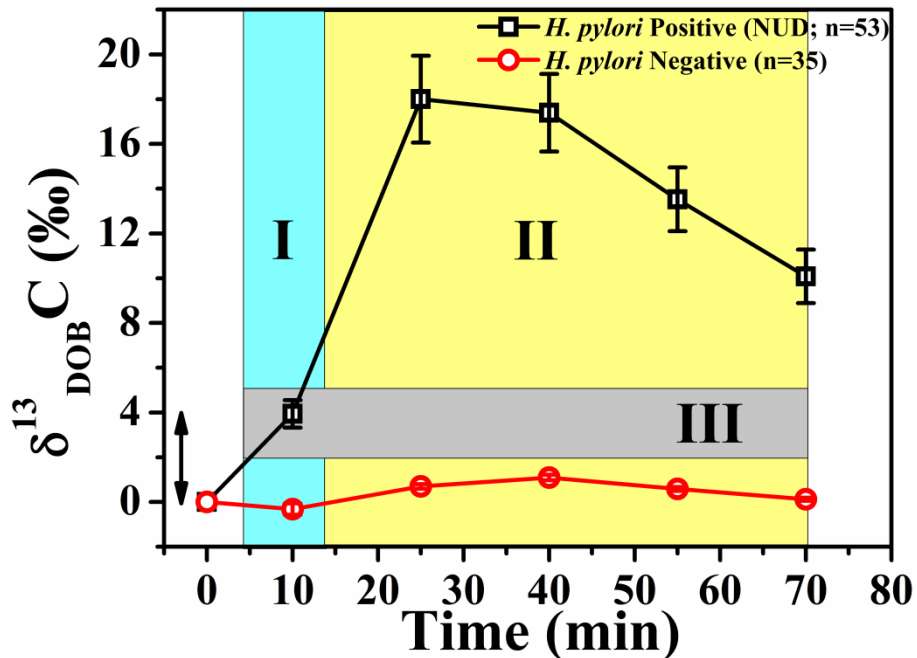


Figure 7.5 Effect of gastric juice urea in the standard ^{13}C -UBT protocol. The figure shows the increment in the $\delta_{\text{DOB}}^{13}\text{C}$ (‰) value for NUD within 10 minutes of ingestion of citric acid where the endogenous urea in gastric juice is utilized by the *H. pylori* and therefore arising ‘grey-zone’ problem for the on-set of the infection. The 0 minute denotes the empty stomach breath sample i.e., before the ingestion of citric acid. The entire excretion dynamics of ^{13}C -UBT is divided into two regions with region-I demonstrating the effect of citric acid and region-II illustrating the effect of ^{13}C -labelled urea whereas the grey region (III) indicates the ‘grey-zone’ of ^{13}C -UBT.

‘grey-zone’ problem. Therefore, the new UBT, exploiting only gastric juice urea, provides a great promise for a better, more robust and non-toxic global methodology compared with the existing ^{13}C -UBT for precise detection of the *H. pylori* infection. Moreover, several earlier evidences [3-5] demonstrated that numerous urease-containing microorganisms other than *H. pylori* are present in the human oral cavity possessing strong urease activity. Therefore the observations of the false positive results of the existing ^{13}C -UBT are likely to be the effects of the

urease activity by the urease-positive non-*H. pylori* bacteria in response to the orally administered ^{13}C -enriched external urea.

7.4 Conclusion

In conclusions, our findings suggest that devoid of any external ^{13}C -enriched urea, the new UBT strategy exploiting the natural ^{18}O and ^{13}C -urea in human gastric juice selectively reveal the specific disease state (i.e. whether it is peptic ulcer or non-ulcer) and correctly diagnose the *H. pylori* infection with unprecedented diagnostic sensitivity and specificity. Consequently, our new UBT overcomes all the existing issues, whereas the present ^{13}C -UBT often fails to do. Nonetheless, the direct exploitation of gastric juice urea in the new UBT methodology should enhance our ability to devise new and better approaches to treat the deleterious effects of all these common diseases. The new knowledge is also fostering exploration in our understanding of the relationship between peptic ulcer disease, non-ulcerous dyspepsia and *H. pylori* infection.

7.5 References

- [1] Goddard A F and Logan R P H 1997 Review article: urea breath tests for detecting *Helicobacter pylori* *Aliment Pharmacol Ther* **11**,641-9.
- [2] Gisbert J P and Pajares J M 2004 Review article: ^{13}C -urea breath test in the diagnosis of *Helicobacter pylori* infection-a critical review *Aliment Pharmacol Ther* **20**, 1001-17.
- [3] Osaki T, Mabe K, Hanawa T and Kamiya S 2008 Urease-positive bacteria in the stomach induce a false-positive reaction in a urea breath test for diagnosis of *Helicobacter pylori* infection *Journal of Medical Microbiology* **57**, 814-9.
- [4] Peng NJ, Lai KH, Liu RS, Lee SC, Tsay DG, Lo CC, *et al.* 2001 Clinical Significance of Oral Urease in Diagnosis of *Helicobacter pylori* Infection by [^{13}C]Urea Breath Test. *Digestive Diseases and Sciences* **46**, 1772-8.
- [5] Brandi G, Biavati B, Calabrese C, Granata M, Nannetti A, Mattarelli P, *et al.* 2006 Urease-Positive Bacteria Other than *Helicobacter pylori* in Human Gastric Juice and Mucosa *Am J Gastroenterol* **101**,1756-61.
- [6] Chirica L C, Petersson C, Hurtig M, Jonsson B H, Borén T and Lindskog S 2002 Expression and localization of α - and β -carbonic anhydrase in *Helicobacter pylori* *Biochim Biophys Acta*. **1601**,192-9.
- [7] Marcus E A, Moshfegh A P, Sachs G and Scott D R 2005 The periplasmic α -carbonic anhydrase activity of *Helicobacter pylori* is essential for acid acclimation *J. Bacteriol.* **187**, 729-38.
- [8] Maity A, Som S, Ghosh C, Banik GD, Daschakraborty SB, Ghosh S, *et al.* 2014 Oxygen-18 stable isotope of exhaled breath CO_2 as a non-invasive marker of *Helicobacter pylori* infection *J. Anal. At. Spectrom.* **29**, 2251-5.
- [9] Neithercut W D, Nujumi A M El and McColl K El 1993 Measurement of urea and ammonium concentrations in gastric juice *J Clin Pathol.* **46**, 462-4.

- [10] Neithercut W D, Milne A, Chittajallu R S, el Nujumi A M and McColl K El 1991 Detection of *Helicobacter pylori* infection of the gastric mucosa by measurement of gastric aspirate ammonium and urea concentrations *Gut* **32**, 973-6.
- [11] Maity A, Banik GD, Ghosh C, Som S, Chaudhuri S, Daschakraborty SB, *et al.* 2014 Residual gas analyzer mass spectrometry for human breath analysis: a new tool for the non-invasive diagnosis of *Helicobacter pylori* infection *J. Breath Res.* **8(1)**:016005. doi:10.1088/1752-7155/8/1/016005
- [12] Keuleers R, Desseyn HO, Rousseau B and Van Alsenoy C 1999 Vibrational Analysis of Urea *J. Phys. Chem. A.* **103**, 4621-30.
- [13] Grdadolnika J and Mare ´chalb Y 2002 Urea and urea-water solutions – an infrared study *Journal of Molecular Structure* **615**,177–89.

Chapter 8

Summary and Future Perspectives

8.1 Summary of the Thesis

The new-generation mid-IR EC-QCL technology in combination with ultra-sensitive spectroscopic techniques has become the core research area in recent times for field deployable sensors to monitor trace gases along with their isotopic species from different environments in real-time. In this thesis, two different spectroscopic methods i.e. (i) cavity ring-down spectroscopy (CRDS) and (ii) calibration-free wavelength modulation spectroscopy (WMS), coupled with a mid-IR EC-QCL operating between 7.5-8 μm , have been developed and standardized for precise and sensitive measurements of trace gases in ambient air. The developed CRDS technique was further demonstrated for highly sensitive measurements of methane isotopes ($^{12}\text{CH}_4$ and $^{13}\text{CH}_4$) in atmosphere and human exhaled breath with a minimum detection limit of 52 pptv and 38 pptv, respectively at atmospheric pressure. In calibration-free WMS technique, $1f$ normalized $2f$ method was utilized along with the pre-characterization of the probed QCL laser and a minimum detection limit of 3 ppbv for trace acetylene (C_2H_2) sensing was achieved with 110 seconds averaging. Furthermore, a simple, robust and cost-effective mass-spectrometric (MS) system was designed using a residual gas analyzer (RGA) and subsequently validated for the measurements of ^{12}C and ^{13}C isotopes of CO_2 in exhaled human breath.

The clinical efficacy of the system was further exploited for detecting ulcer causing *H. pylori* infection in human stomach by means of exhaled breath CO₂ isotope analysis in combination with ¹³C-UBT. Two new exhaled breath markers in forms of ¹⁸O isotope of CO₂ (¹²C¹⁸O¹⁶O) and hydrogen (H₂) were reported for non-invasive diagnosis of *H. pylori* infection. The monitoring of ¹²C¹⁸O¹⁶O isotope in exhaled breath paved a way for cost-effective breath test to detect *H. pylori* infection in human stomach eliminating any requirement of ¹³C-enriched substrate. In contrast, breath H₂ test, in response to a citric acid test meal, provided a unique advantage over the conventional non-invasive ¹³C-UBT. Breath H₂ test can distinguish two different stages of *H. pylori* infection i.e. peptic ulcer (PUD) and non-ulcerous dyspepsia (NUD) whereas the conventional non-invasive ¹³C-UBT fails to do so. Finally, we explored the applicability of a diode laser based cavity enhanced absorption technique, typically used to measure gas samples, to quantify an analyte concentration in liquid sample in combination with a chemical reaction. The technique was utilized to measure the concentration of urea and its isotopic abundances in human gastric juice and subsequently a potential link to the isotopic fractionations of exhaled breath CO₂ was established for *H. pylori* infected individuals.

8.2 Future Perspectives

This section discusses a few more likely directions that may be taken presently as well as potential improvements that can be targeted in future associated with the different techniques and protocols presented in this thesis.

8.2.1 Measurement of ¹³C/¹²C isotope ratio by the developed QCL based spectrometer

In chapter 2, the developed CRDS technique, coupled with a EC-QCL, was demonstrated for the quantitative measurements of ¹²CH₄ and ¹³CH₄ isotopes individually. However, it was pointed out in the chapter that

the precision of the measurements of $^{13}\text{CH}_4$ was not sufficient to express the measurements in $^{13}\text{C}/^{12}\text{C}$ ratio which is a better parameter in isotope analysis. Therefore, the measurement precision of the developed set up is required to be improved by reducing the relative error of ring-down time measurements and subsequently enhancing the stability of the ring-down cell.

8.2.2 Combination of WMS and ICOS

In chapter 3, it was mentioned that the minimum detection limit of WMS technique can be further enhanced by using a multi-pass cell. It was also previously described that ICOS technique utilizes the output intensity to measure sample concentrations. Therefore, ICOS will be the most suitable cavity enhanced absorption technique that can be combined with the WMS technique to achieve sub-ppt (10^{-12}) level sensitivity. Moreover, this combination will be better suited to tackle pressure-broadened and overlapping absorption lines.

8.2.3 Miniaturization of RGA-MS system

The miniaturization process of RGA-MS system is currently underway to make it more portable and convenient for clinical laboratories. The previous open ion-source is replaced by a closed ion-source to eliminate the requirement of an additional sample injection chamber. Also, new amendments have been planned to make the system suitable for on-line measurements.